Numerička simulacija strujanja u višestupanjskom aksijalnom kompresoru

Bartolec, Bruno

zir.nsk.hr

dabar
DIGITALNI AKADEMSKI ARHIVI I REPOZITORIJI

UNIVERSITY OF ZAGREB

Faculty of Mechanical Engineering and Naval Architecture

MASTER'S THESIS

Bruno Bartolec

Zagreb, 2017

UNIVERSITY OF ZAGREB

Faculty of Mechanical Engineering and Naval Architecture

NUMERICAL SIMULATION OF THE FLOW IN A MULTI-STAGE AXIAL COMPRESSOR

Supervisor: Student:

Prof. Hrvoje Jasak, PhD   Bruno Bartolec

Zagreb, 2017

I hereby declare that this thesis is entirely the result of my own work except where otherwise indicated. I have fully cited all used sources and I have only used the ones given in the list of references

<div align="right">
Thank you,
Bruno Bartolec
</div>

Sveučilište u Zagrebu	
Fakultet strojarstva i brodogradnje	
Datum	Prilog
Klasa:	
Ur.broj:	

DIPLOMSKI ZADATAK

Student: **Bruno Bartolec**   Mat. br.: 0035185172

Naslov rada na
hrvatskom jeziku: **Numerička simulacija strujanja u višestupanjskom aksijalnom kompresoru**

Naslov rada na
engleskom jeziku: **Numerical Simulation of the Flow in a Multi-Stage Axial Compressor**

Opis zadatka:

Simulation of fluid flow in multi-stage axial compressors using Computational Fluid Dynamics (CFD) is used regularly during design and optimisation of such machines. Increased compressor efficiency is critical for the overall performance of a gas turbine, but brings various challenges. The objective of this project is to evaluate the performance of OpenFOAM in practical compressor simulations for design and off-design conditions.

In this study, compressible turbulent quasi-steady flow in a 3.5-stage axial compresor studied at the Institute of Jet Propulsion and Turbomachinery at RWTH Aachen University (Hoynacki, 1999) shall be simulated using OpenFOAM and results shall be compared with available experimental data.

The candidate shall perform the following tasks within this project:

- Describe a CFD model for a 3.5-stage axial compressor, accounting for the handling of flow characteristics (gas compressibility, turbulence, transient effects), rotating components, rotor-stator interfaces and appropriate inlet/outlet boundary conditions. Select and justify a level of approximation for each of the above in the CFD model. Comment on the necessary simplifications in terms of compressor geometry and flow physics;
- Collect the available experimental and reference numerical data for the RWTH Aachen 3.5-stage compressor;
- Prepare a computational mesh for the RWTH Aachen 3.5-stage compressor geometry;
- Perform a CFD simulation of the flow in the compressor for the nominal operation point, as described in the literature. Perform further simulations at several operating points at 68% and 100% of the nominal rotational velocity and plot the results in form of pressure ratio and efficiency curves for two rotational velocities;
- Compare the detailed flow field results against available experimental data in form of pressure, temperature and Mach number fields in a given cross section and pressure distribution on the blade.

The Thesis shall list the bibliography and any assistance received during this study.

Zadatak zadan: Rok predaje rada: Predviđeni datumi obrane:

9. ožujka 2017.   11. svibnja 2017.   17., 18. i 19. svibnja 2017.

Zadatak zadao: Predsjednica Povjerenstva:

Prof. dr. sc. Hrvoje Jasak   Prof. dr. sc. Tanja Jurčević Lulić

Table of Contents

List of Figures

List of Tables

Nomenclature

Greek letters

ω	Angular velocity	s^{-1}
σ	Cauchy Stress Tensor	Pa
τ	Viscous stress tensor	Pa
γ	Diffusion coefficient	$\text{m}^2\,/\,\text{s}^2$
$\Gamma_{\omega,\text{eff}}$	Effective diffusivity of specific turbulence dissipation rate	$\text{m}^2\,/\,\text{s}$
$\Gamma_{\text{k,eff}}$	Effective diffusivity of turbulence kinetic energy	$\text{m}^2\,/\,\text{s}$
λ	Thermal conductivity	$\text{W}\,/\text{m}\cdot\text{K}$
μ	Dynamic viscosity	$\text{Pa}\cdot\text{s}$
ν	Molecular kinematic viscosity	$\text{m}^2\,/\,\text{s}$
ω	Specific dissipation rate	s^{-1}
Φ	Arbitrary turbulent quantity	-
ϕ	Transported scalar variable	-
Φ''	Fluctuating component of an arbitrary turbulent quantity	-
ψ	Compressibility	$\text{s}^2\,/\,\text{m}^2$
ρ	Fluid density	$\text{kg}\,/\,\text{m}^3$
$\widetilde{\Phi}$	Favre-Averaged arbitrary turbulent quantity	-
μ_t	Turbulent (eddy) viscosity	$\text{Pa}\cdot\text{s}$

Latin letters

D	Symmetric part of the velocity gradient	s^{-1}
g	Gravitational acceleration	$\text{m}\,/\,\text{s}^2$
I	Identity (unit) tensor	-
q	Heat flux vector	$\text{W}\,/\,\text{m}^2$
R	Reynolds Stress Tensor	Pa

u	Velocity vector	m / s
$\mathbf{u}_{\text{rel}}$	Relative velocity vector	m / s
$\widetilde{\mathbf{u}}$	Favre-Averaged velocity	m / s
e	Specific total energy	J / kg
F_1	Blending Function	-
F_2	Blending Function	-
h	Specific enthalpy	J / kg
h_0	Specific total enthalpy	J / kg
i	Rothalpy	J / kg
k	Turbulent kinetic energy	m^2 / s^2
p	Static pressure	Pa
q_v	Volumetric sources and sinks of the scalar field	-
R	Individual gas constant	J / kg $\cdot$ K
r	Radius	m
S_{H}	Source term of enthalpy	W / m^3
T	Absolute temperature	K
t	Time	s
u	Internal energy	J / kg
u_{Θ}	Tangential component of the absolute velocity vector	m / s

Abbreviations

CFD   Computational Fluid Dynamics

GGI   General Grid Interface

MRF   Multiple Reference Frame

IDAC   Inversely Designed Aachen Compressor

IGV   Inlet Guide Vane

CDA   Controlled Diffusion Aerofoils

RANS   Reynolds Averaged Navier-Stokes Equations

SST   Shear Stress Transport

FVM   Finite Volume Method

Abstract

Design and optimisation og various types of machinery has been significantly improved with the utilization of numerical simulations. Computational Fluid Dynamics (CFD) deals with numerical simulations of fluid flow in a wide variety of cases. One of the premier applications of CFD is simulating fluid flow inside turbomachines. Turbomachines play a vital role in energy conversion and as such it is important that turbomachines operate efficiently and flexibly.

A key element that needs to be addressed when doing turbomachinery CFD simulations is the so called rotor-stator interface. The fluid flow inside a turbomachine is often assumed periodic which allows for only a part of the machine to be simulated thus, lowering the required computational resources. Computational resources can also be spared with approximating transient fluid flow with a quasi-steady state solution, the so called frozen rotor approach.

In this thesis the fluid flow inside the IDAC is simulated using the open source CFD package OpenFOAM. The multi-stage axial turbo compressor was developed and extensively tested at RWTH Aachen University. In order to resolve the rotor-stator interaction two different types of interfaces are used: the mixing plane interface and the General Grid Interface (GGI). Since only a part of the compressor, a single passage is simulated a periodic boundary condition must be applied. For this purpose a variation of the GGI is employed.

Numerical simulations are performed for four different operating points, two at the nominal design speed and two at 68% of the nominal design speed. The results of numerical simulations are presented as images of the flow field for different variables but also compared to avaliable experimental results in terms of mass flow rate, total pressure ratio, and efficiency.

Keywords: *CFD*, *OpenFOAM, mixing plane*, *General Grid Interface*, *multi-stage turbomachinery*

Sažetak

Konstrukcija i optimizacija različitih vrsta strojeva je značajno poboljšanja primjenom numeričkih simulacija. Područje istraživanja koje se bavi simuliranjem strujanja fluida nayiva se računalna dinamika fluida. Jedna od najznačajnih primjena računalne mehanike fluida je numeričko modeliranje strujanja unutar turbostrojeva. Zbog važnosti uloge turbostrojeva u pretvorbi energije, njihov rad mora biti efikasan i fleksibilan.

Kod simuliranja strujanja u turbostrojevima važno je obratiti pažnju na sučelje između rotora i statora. Strujanje u turbostroju se može smatrati periodičnim što omogućava provedbu simulacije samo na dijelu turbostroja, čime se smanjuju potrebni računalni resursi. Dodatno smanjenje računalnih resursa je moguće računanjem stacionarnog stanja uunutar turbostroja umjesto tranzijentnog strujanja.

U sklopu ovog rada, *open source* računalni paket OpenFOAM upotrebljen je za simulaciju stlačivog strujanja unutar trostupanjskog kompresora konstruiranog na sveučilištu Aachen. Za sučelje između rotora i statora upotrebljene su dvije različite metode, *mixingPlane* i *overlapGGI*. Metoda *overlapGGI* je izvedenica *Generalized Grid Interface* metode spajanja nekomfornih numeričkih mreža. Pod pretpostavkom periodičkog strujanja simuliran je samo jedan međulopatični prolaz. Na granicama međulopatičnog prostora kao periodični rubni uvjet primjenjen je *cyclicGGI*, također izvedenica *Generalized Grid Interface* metode.

Numeričke simulacije provedene su za četiri radne točke, dvije za nominalnu brzine vrtnje te dvije za reduciranu brzinu vrtnje. Rezultati numeričkih simulacija prikazani su obliku polja značajnih fizikalnih veličina, ali također uspoređeni s eksperimentalnim podacima kao što su maseni tok, omjer totalnih tlakova i efikasnost.

Keywords: *Računalna mehanika fluida*, *OpenFOAM*, *višestupanjski turbokompresor*

Prošireni Sažetak

(EXTENDED ABSTRACT IN CROATIAN)

Uvod

Cilj ovog rada je provedba numeričke simulacije stlačivog strujanja u trostupanjskom kompresoru izrađenom i ispitanom na Sveučilištu Aachen te usporedba dobivenih numeričkih rezultata s dostupnim eksperimentalnim podacima u svrhu validacije numeričkog postupka. Kompresor na kojem su provedene numeričke simulacije je transonični kompresor nazvan Inversly Designed Aachen Compressor (IDAC). Simulacije su provedene u četiri različite radne točke korištenjem `foam-extend` softwarea [1].

Matematički model

Matematički model koji korišten za modeliranje stačivog strujanja unutar aksijalnog kompresora sastoji se od jednadžbe očuvanja mase, jednadžbe očuvanja količine gibanja, jednadžbe očuvanja energije te konstuntivnih jednadžbi potrebnih da bi se *zatvorio* matematički model. Jednadžba očuvanja energije nije zapisana u obliku očuvanja totalne energije ili totalne entalpije kao što je to uobičajeno već u obliku očuvanja rotalpije. Rotalpija je fizikalna veličina karakteristična za turbostrojeve, izvedena iz zakona očuvanja energije i Eulerove jednadžbe za turbostrojeve. Za rotolapiju je karakteristično to da je konzervirana unutar reda rotorkskih ili statorskih lopatica, ali nije konzervirana unutar cijelog stupnja turbostroja.

Modeliranje rotacije rotora turbo kompresora ostvareno je primjenom *Multiple Reference Frames* metod (MRF metode) [2]. Primjenom MRF metode značajno se smanjuje potrebno računalno vrijeme izrvšavanja numeričke simulacije jer numerička mreža ostaje nepomična u prostoru. Efekt rotacije je postignut dodavanjem dodatnih inercijskih članova u jednadžbe matematičkog modela. Jednadžbe očuvanja s primjenjenom MRF metodom glase:

– jednadžba očuvanja mase,

$$\frac{\partial \rho}{\partial t} + \nabla \bullet (\rho \mathbf{u}) = 0, \tag{1}$$

– jednadžba očuvanja količine gibanja,

$$\frac{\partial (\rho \mathbf{u})}{\partial t} + \nabla \bullet (\rho \mathbf{u}_{\text{rel}} \otimes \mathbf{u}) + \omega \times (\rho \mathbf{u}) = -\nabla p + \nabla \bullet \tau + \rho \mathbf{g}, \tag{2}$$

– jednadžba očuvanja rotalpije,

$$\nabla \bullet (\rho i \mathbf{u}_{\text{rel}}) = -\nabla \bullet (\rho \omega r u_{\Theta} \mathbf{u}_{\text{rel}}) - \nabla \bullet (p \mathbf{u}) + \nabla \bullet (\tau \cdot \mathbf{u}) + \nabla \bullet (\lambda \nabla T) + S_{\text{H}}. \tag{3}$$

Geometrija aksijalnog turbokompresora sastoji se od lopatica raspoređenih po obodu te u više stupnjeva. Stupanje turbostroja sastoji se od reda jednog reda rotorskih i jednog reda statorskih lopatica. Zbog geometrije turbostroja može se pretpostaviti da je strujanje u njemu aksisimetrično. Uz tu pretpostavku dovoljno je simulirati strujanje u jednom međulopatičnom kanalu, odnosno jednom prolazu, te se time značajnu smanjuju računalni resursi potrebni za provedbu numeričke simulacije. Da bi ovaj pristup bio moguć potrebno je koristiti ciklični rubni uvjet na granici mežulopatičnog prostora. U opsegu ovog rada korišten je `cyclicGGI` rubni uvjet, inačica GGI sučelja za povezivanje nekonformnih mreža [3]. Zbog geometrije samih lopatica iznimno je teško generirati jedinstvenu numeričku mrežu za cijeloviti prolaz aksijalnog turbokompresora. Uobičajeno je generirati mrežu oko jedne lopatice te koristiti sučelje kako bi se zasebne lopatične mreže povezale u cijelilnu. U sklopu ovog rada korištena su dva različita sučelja: `overlapGGI`, također inačica GGI sučelja [3] te `mixingPlane` sučelje [4].

Inversly Designed Aachen Compressor - geometrija i prostorna disretizacija

IDAC je višestupanjski askijalni turbokompresor dizajniran u svrhu ispitivanja nestacionarnih fenomena unutar turbokompresora te međusobne interakcije uzvodnih i nizvodnih stupnjeva [5]. Uz tri stupnja kompresor također ima red usmjeravajućih lopatica ispred prvog stupnja. Shema kompresora prikazana je na Slici 1
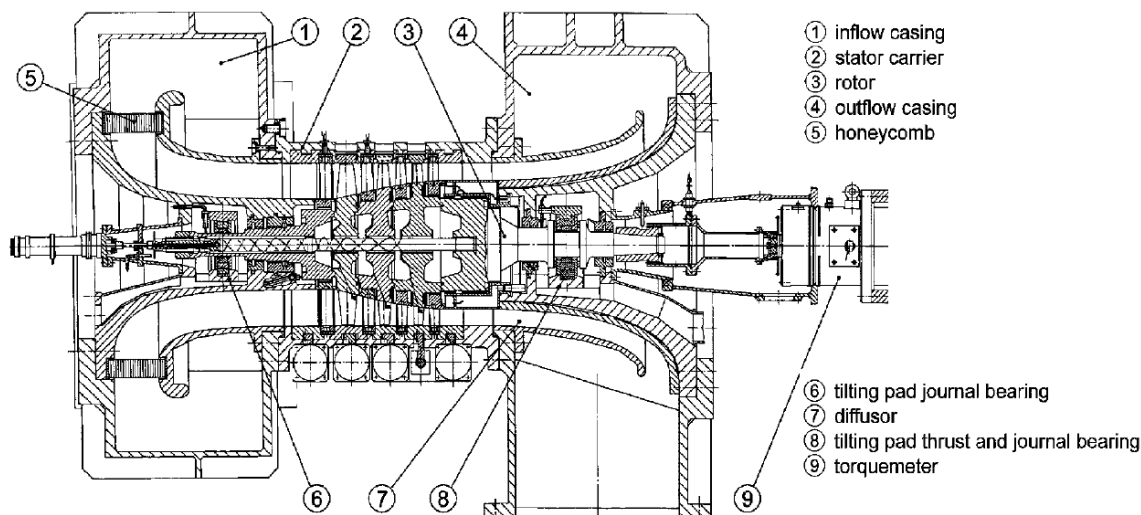
Slika 1: IDAC PRESJEK [5].

Profil lopatica je posebnog oblika koji omogućava da se kontroliranom difuzijom izbjegne pojava udarnog vala pri prelasku iz nadzvučnog u podzvučnog strujanje i razvijen je posebno za primjenu u transoničnim turbostrojevima. Pojava udarnog vala uzrokuje gubitke, a može i izazvati i odvajanje graničnog sloja koje stvara dodatne gubitke. Uobičajena metoda

sprječavanja pojave udarnog vala je tanji profil ulaznog i izlaznog brida lopatice. Kod lopatica s kontroliranom difuzijom ulazni i izlazni brid mogu biti deblji što dopušta veće opterećenje lopatica te produžuje njihov radni vijek. Karakteristike lopatica svakog pojedinog stupnja prikazane su u Tablici 1.

Table 1: KARAKTERISTIKE IDAC LOPATICA [6].

	Vodeće lopatice	Prvi stupanj		Drugi stupanj		Treći stupanj	
		Rotor	Stator	Rotor	Stator	Rotor	Stator
Broj lopatica	38	25	40	31	42	39	46
Duljina tetive [mm]	32	50	30	38	28	31	26
Visina lopatica [mm]	86.72	86	71.1	61.18	53.76	47.74	43.68

Geometrija jednog lopatičnog prolaza za koji će biti izrađena numerička mreža prikazana je na Slici 2. Za svaku od sedam lopatica napravljena je zasebna numerička mreža, koja čini takozvanu regiju cijeloukupne mreže, koja je zatim povezana `mixingPlane` sučeljem. Pošto je topologija numeričke mreže oko svih lopatica ista u nastavku će detaljno biti prikazana mreža oko prve rotorske lopatice.
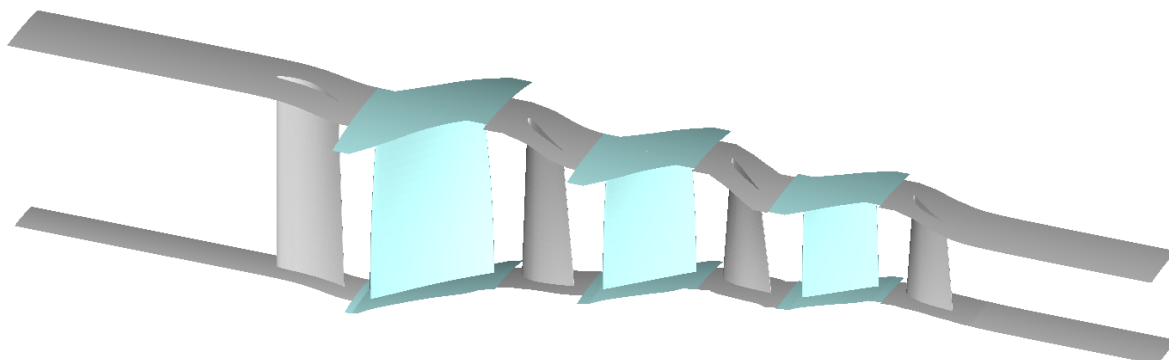
Slika 2: GEOMETRIJA ROTORSKIH (TIRKIZNO) I STATORSKIH (SIVO) LOPATICA, BUBNJA I KUĆIŠTA KOMPRESORA.
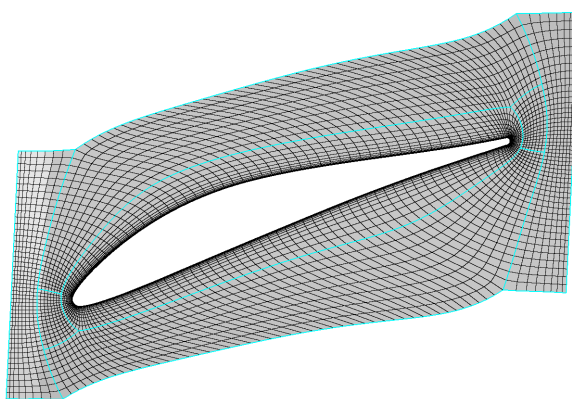
Slika 3: TOPOLOGIJA NUMERIČKE MREŽE PRVE ROTORSKE LOPATICE.

Slika 3 prikazuje *mutli-block* topologiju numeričke mreže za prvu lopaticu. Topologija mreže je takozvana O-H struktura koja omogućava izradu optimalnih numeričkih mreža međulopatičnog prostora u aksijalnim turbostrojevima. Oko lopatice se nalazi O blok napravljen normalnom ekstruzijom iz površinske mreže lopatice. H blokovi koji čine ostatak mreže nalaze se na karakterističnim dijelovima geometrije lopatice, pretlačnoj i potlačnoj strani, ulaznom i izlaznom bridu lopatice te ulazu i izlazu u međulopatični prostor.
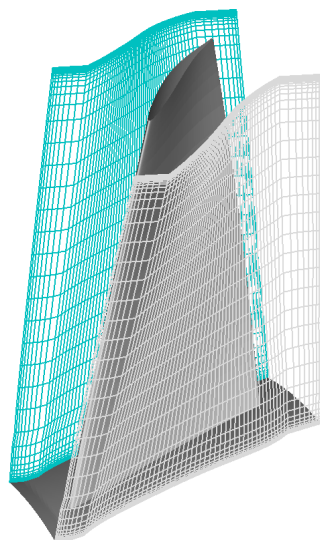
Slika 4: Periodične granice mreže prve rotorske lopatice.

Na Slici 4 prikazani su *patchevi* na kojima je primjenjen `cyclicGgi` rubni uvjet. Slika 5 pokazuje lokaciju sučelja između različitih regija mreže te je također naznačen ulaz i izlaz iz numeričke dodomene.
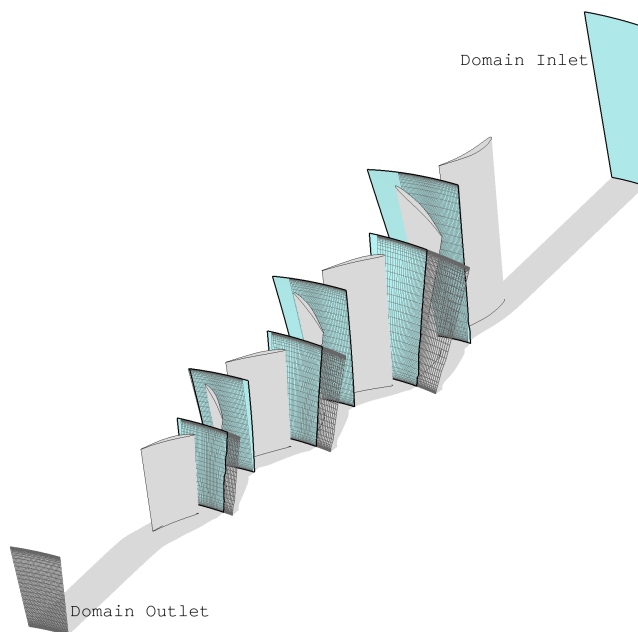
Slika 5: Ulazi (tirkizno) i izlazi (sivo) za svaku od regija numeričke mreže.

Numerička mreža jednog međulopatičnog prolaza kompresora prikazana je na Slici 6. Mreža se sastoji od ukupno 2 400 768 heaksaedarskih kontrolnih volumena. Zbog različitog broja lopatica u svakom redu kompresora relativni položaj lopatica nije periodičan po cijelom obodu turbokompresora. Zbog toga bi primjena `overlapGgi` metode na sučelju izmežu rotora i statora ne bi bila fizikalna. Kako bi `overlapGgi` metoda bila promjenjiva geometrija kompresora je izmjenjana u oblik gdje svaki stupanj ima jednak broj lopatica.
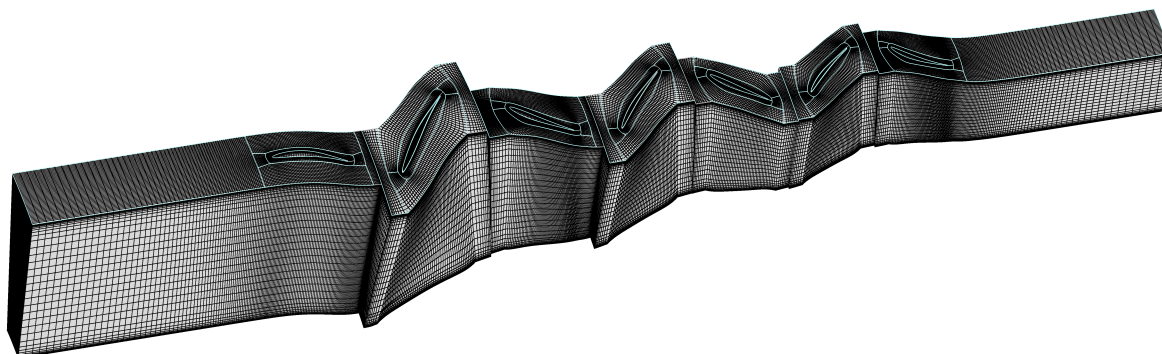
Slika 6: NUMERIČKA MREŽA KOMPRESORA.

Rezultati

U nastavku su prikazani rezultati za projektnu radnu točku dobiveni korištenjem `mixingPlane` metode. Rezultati za ostale radne točke nalaze se u radu kao i rezultat za projektnu radnu točku sa `overlapGgi` metodom.

Tablica 2 prikazuje usporedbu između eskperimentalnih mjerenja i numeričke simulacije za projektnu radnu točku. Rezultati numeričke simulacije pokazuju zadovoljavajuće poklapanje sa eksperimentalnim mjerenjima. Razlika u rezultatima je vjerojatno uzrokovana modeliranjem turbulencije, prostornom diskretizacijom i pojednostavljenima geometrije kompresora.

Table 2: USPOREDBA EKSPERIMENTALNIH I NUMERIČKIH REZULTATA ZA PROJEKTNU RADNU TOČKU

	Eksperiment	Numerička Simulacija	Relativna Greška [%]
Maseni Protok [kg/s]	13.66	13.02	-4.66
Omjer totalnih tlakova 1. stupnja	1.31	1.32	0.71
Omjer totalnih tlakova 2. stupnja	1.27	1.29	1.84
Omjer totalnih tlakova 3. stupnja	1.23	1.23	0.16
Ukupni omjer totalnih tlakova	2.06	2.09	2.71
Adijabatska Efikasnost [%]	90.4	82.1	-9.15
Snaga [kW]	996	1068	7.19
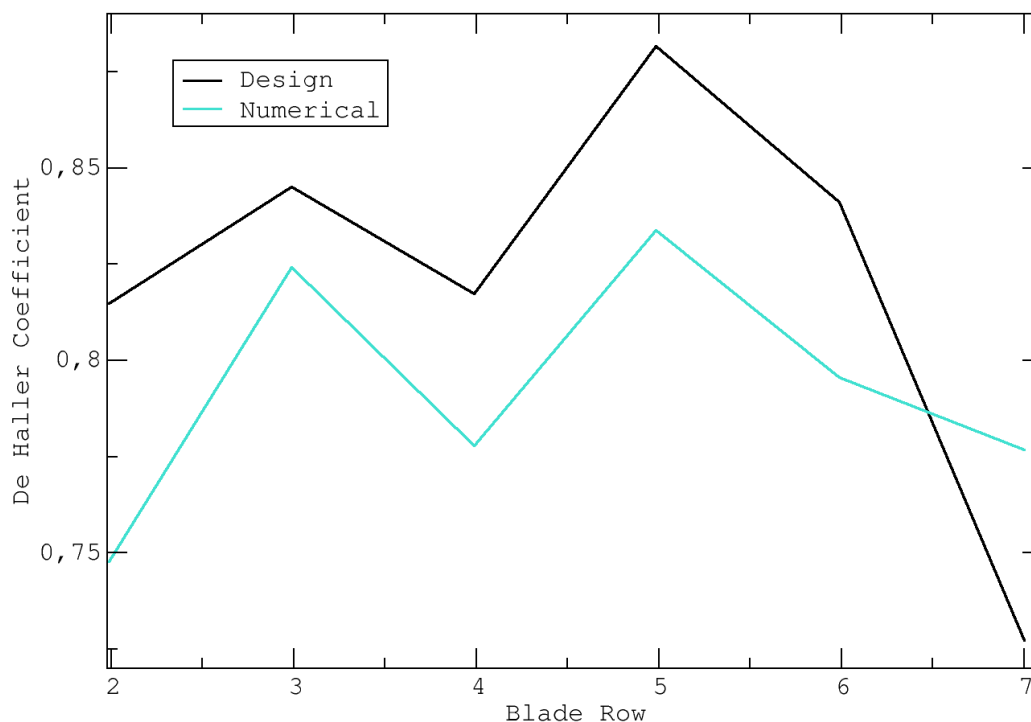
Slika 7: Usporedba de Hallerovog koeficijenta izmađu projektnih vrijednosti i rezultata numeričke simulacije.

Slika 7 prikazuje usporedbu de Hallerova koeficijent za pojedine redove lopatica. Na horizontalnoj osi prvi red rotorskih lopatica je označen dvojkom dok je zadnji red statorskih lopatica označen brojkom sedam. De Hallerov koeficijent je jednostavan pokazatelj opterećenosti lopatice [7]. Računa se prema sljedećem izrazu

$$\text{de Haller} = \frac{\mathbf{u}_{\text{outlet}}}{\mathbf{u}_{\text{inlet}}} \tag{4}$$

Pri računanju de Hallerovog koeficijenta za statorske lopatice u obzir se uzima apsolutna brzina, a za rotorske relativna. Ako je de Hallerov koeficijent manji od 0.7 na lopatici može doći do odvajanja strujanja [7]. De Hallerov koeficijent dobiven iz rezultata numeričke simulacije prati trend projektnog de Hallerovog koeficijenta iako numerički rezultati pokazuju veće opterećenje lopatica. Značajna razlika u de Hallerovom koeficijentu je na zadnjoj statorskoj lopatici. Projektne vrijednosti pokazuju puno veće opterećenje lopatice nego numerički rezultati. Ova razlika je vjerojatno uzrokovana razlikom u metodi računanja de Hallerovog koeficijenta budući da numerički rezultati pokazuju vidljivo odvajanje strujanja.

Slika 8 prikazuje usporedbu statičkog tlaka na kućištu kompresora izmjerenog eksperimentom i izračunatog numeričkom simulacijom. Vrijednosti dobivene numeričkom simulacijom poklapaju se u trendu s eksperimentalnim podacima, dok po vrijednostima postoje odstupanja.
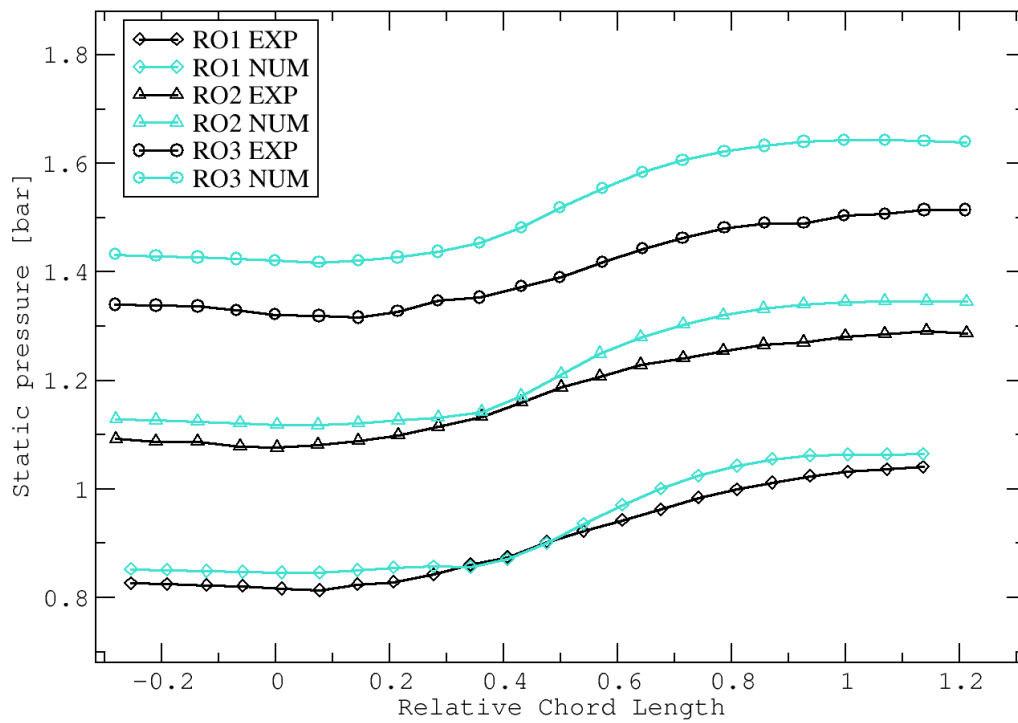
Slika 8: Usporedba raspodjele na kućištu kompresora između eksperimenta i numeričke simulacije.

Zadnja statorska lopatica je dizajnirana tako da bude značajno opterećenja. Na njoj prilikom rada u projektnoj radnoj točki dolazi do odvajanja strujanja. Odvajanje strujanja je vidljivo na polju totalnog tlaka iza statorske lopatice. Usporedba totalnog tlaka izmjerena eksperimentom i dobivena simulacijom vidljiva je Slici 9.

(a) Eksperimentom izmjereni totalni tlak [8].

(b) Numerički izračunati totalni tlak.
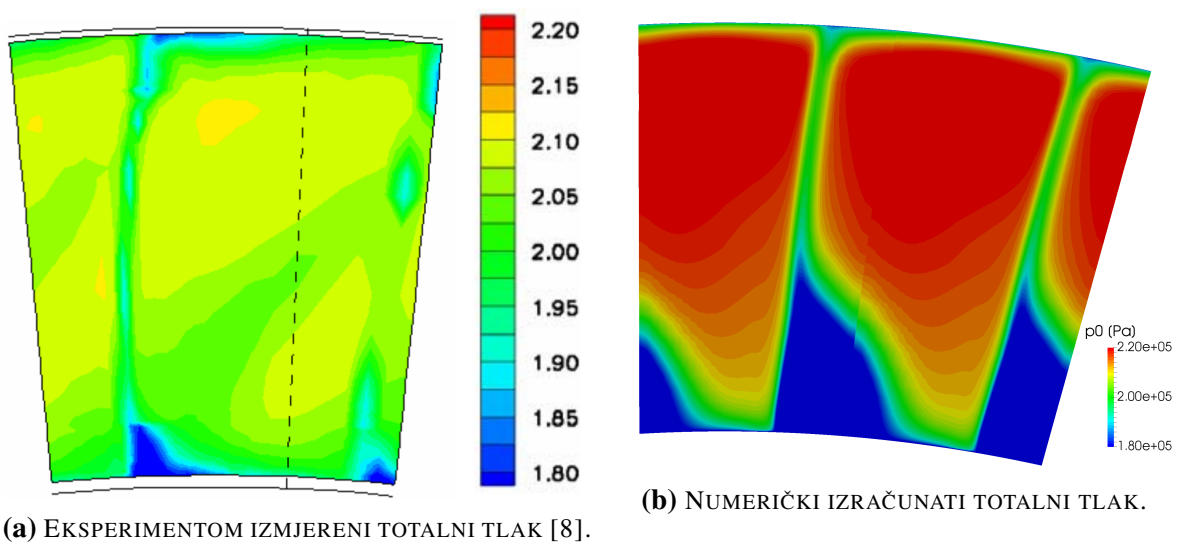
Slika 9: Usporedba polja totalnog tlaka iza zadnjeg statora između eksperimenta i numeričke simulacije.

Numerička simulacijom dobiveno je veće odvajanje strujanja nego što je izmjereno eksperimentom. Vrtlog na zadnjoj lopatici dobiven numeričkom simulacijom prikazan je strujnicama na Slici 10. Poremečaj strujanja proteže se do trećine visine lopatice.
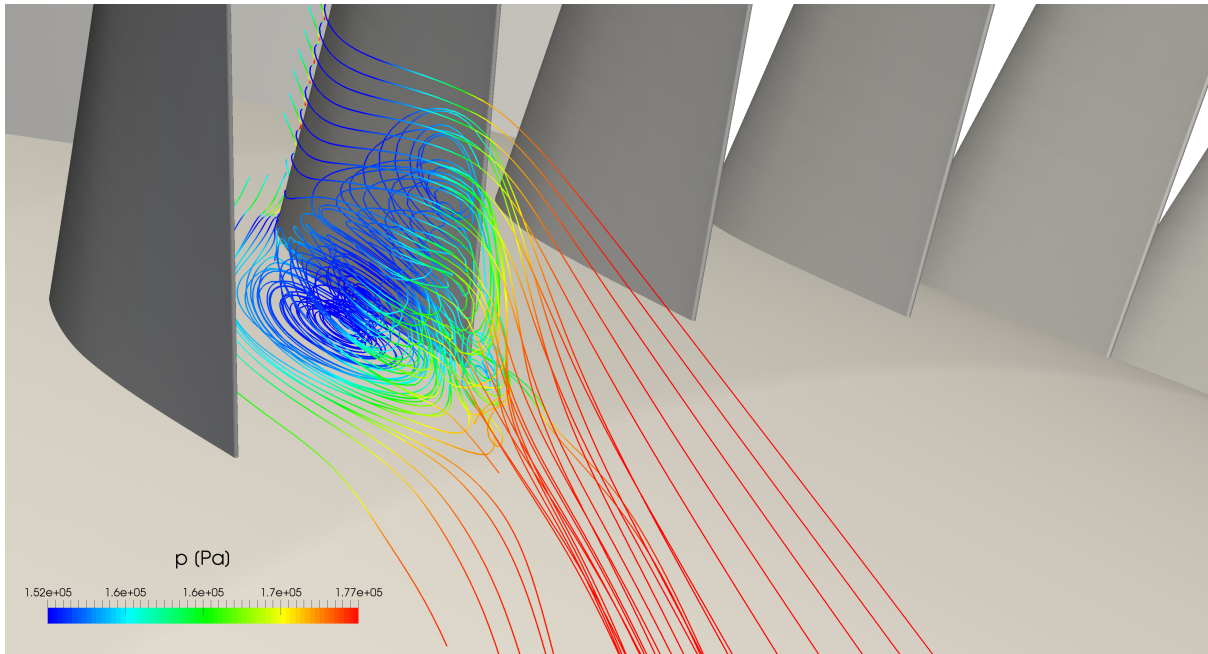
Slika 10: ODVAJANJE STRUJANJA NA ZADNJEM STATORU.

Polje tlaka na konstantnom radijusu unutar kompresora prikazano je na Slici 11. Na ulazu u kompresor dolazi do ubrzavanja strujanja te je zbog u području usmjeravajućih lopatica nizak tlak. Vidljivo je da tlak raste kroz stupnjeve kompresora.

Slika 11: POLJE TLAKA ZA PROJEKTNU RADNU TOČKU.

Slika 12 prikazuje polje statičke temperature. Vrtložni tragovi iza lopatica karakterizirani su većom temperaturom od glavnine strujanja. Uzrok povećanju temperature je disipacija kinetičke energije uzrokovana turbulencijom i mješanjem.
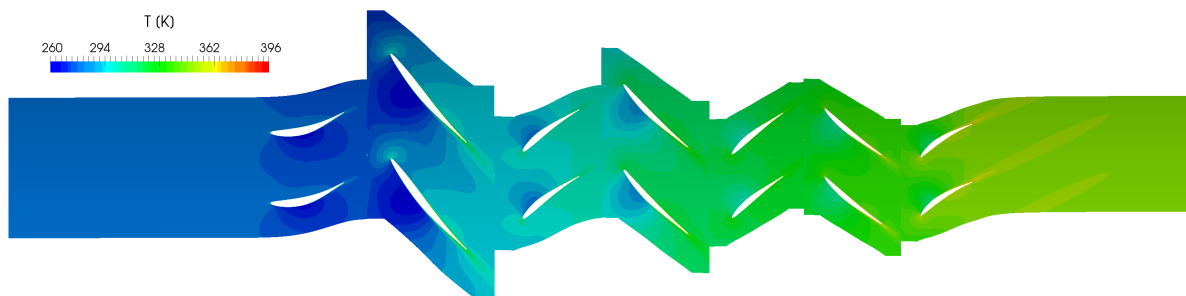
Slika 12: Polje temperature za projektnu radnu točku.

Na Sliici 13 prikazano je polje apsolutnog Machovog broja. Na statorskim lopaticama vidljivo je karakteristično ubrzanje strujanja na potlačnoj strani.
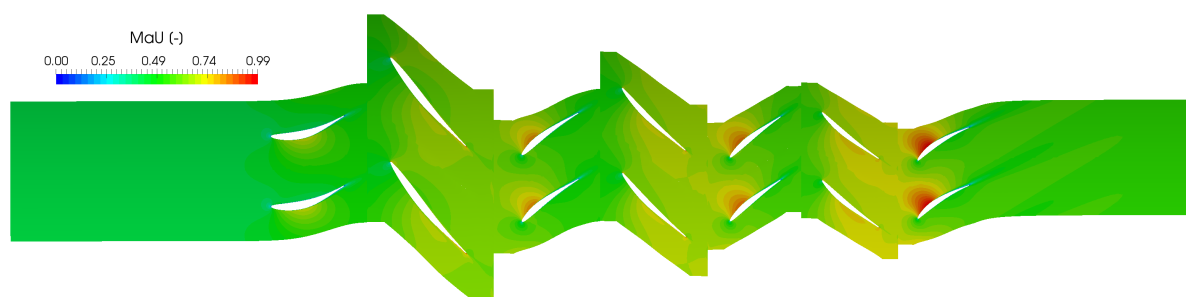
Slika 13: Polje Machovog broja za projektnu radnu točku.

Polje relativne brzine prikazano je na Slici 14. Na polju relativne brzine uz karakteristično ubrzanje na podtlačnoj strani statorskih lopatica može se vidjeti i karakteristično ubrzanje na podtlačnoj strani rotorskih lopatica.
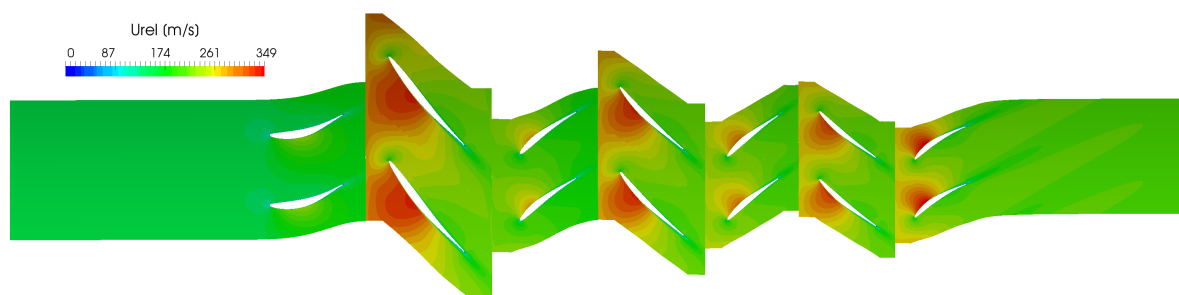
Slika 14: Polje relativne brzine za projektnu radnu točku.

Kod polja rotalpije prikazanog na Slici 15 vidljive su karakteristike the fizikalne veličine. Rotalpija je očuvana u lopatičnom redu te postoji skok između vrijednosti rotalpije u rotoru i vrijednosti rotalpije u statoru.
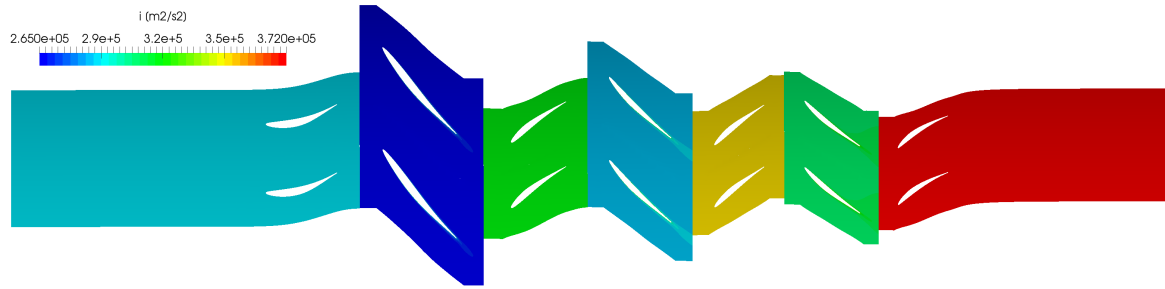
Slika 15: Polje rotalpije za projektnu radnu točku.

Zaključak

Prikazani rezultati numeričke simulacije stlačivog strujanja unutar aksijalnog turbo kompresora pokazuju zadovoljavajuću točnost u usporedbi s eksperimentalnim mjerenjima. Ne samo u globalnim vrijednostima već i u detaljima strujanja kao što je tlak na kućištu kompresora. Točnost prikazanih rezultata dokazuje valjanost primjene numeričkih simulacija u procesu konstruiranja aksijalnih turbokompresora.

1 Introduction

The focus of technological development in industry today is the increase of efficiency and flexibility. The incentive for higher efficiency is not only economical but also ecological. High flexibility means that the process is efficient throughout its operating range and not just at a single working point. This allows for the industrial process to adapt to a demand outside the optimal operating point without high decrease in efficiency. To improve upon an industrial process it is necessary to understand which parameters influence the process in what way and what happens during the process for its duration.

With the application of mathematical expressions it is possible to predict an outcome of a certain process under the influence of observed parameters. Describing any process through mathematical expressions is called mathematical modelling. Since natural phenomena is highly complex, the accompanying mathematical model will be equally if not even more complex. Therefore to be applicable, a mathematical model is derived only to capture the relevant occurrences in a process and does not get to complex for solving. For example, if one wishes to know the temperature in a room it is not necessary to track every single molecule of air inside the room but it is a must to take into account the energy coming from the Sun or a space heather inside the room.

Fluid flows are part of everyday human experience but also a crucial part of most industrial operations. Main role of fluids in industrial operations is the transport of mass and energy. The study of fluid flows trough mathematics is called fluid mechanics. In fluid mechanics the continuum hypothesis defines that a fluids density is a continuous function. Along with density other properties of the fluid are also considered continuous [9]. Within fluid mechanics there are numerous types of flows classified by their specific characteristics. Through a certain amount of simplifications and assumptions, analytically solvable mathematical models have been developed and are used in engineering practice. If one wishes to improve the efficiency of a complex flows, it is necessary to obtain the intricacies of the fluid flow. The mathematical model that is able to capture the complex spatial and temporal nature of fluid flows is available, but unsolvable through analytical procedures. In cases where an analytical solution is unattainable it is possible to obtain a numerical solution, which is an approximation of the analytical solution. Field of fluid mechanics dedicated to obtaining numerical solutions is called Computational Fluid Dynamics (CFD).

Numerical simulations are a way of solving complex mathematical models with the use of computers. Although numerical analysis was used before the invention of computers it has come to the forefront in engineering practice with the growth of computational resources. Since in numerical simulations the calculation is done on a computer, the mathematical model must only contain the mathematical operations which are feasible on a computer. Adapting certain mathematical models for numerical simulations means that the results gained with the numerical simulation will only be an approximation of the analytical result since certain

mathematical operators must be replaced with much simpler ones. Even as such, numerical simulations are extremely valuable in today's scientific research and engineering practice. With the use of numerical simulations various problems in various fields of science and engineering are solved, like for example molecular dynamics which studies the movement and interaction of molecules in biology and chemistry [10], stress analysis in mechanical and civil engineering, and of course the study of fluid flows solved within computational fluid dynamics. Since numerical simulations are only an approximation of analytical results which come from a simplified mathematical model of the real process, a cautious approach to evaluating the quality of numerical results is needed. A prior understanding of observed natural phenomena, numerical methods and experience is required for successful numerical analysis. As a means of validating numerical results a comparison with experimental results is often performed. Experiments are typically more time consuming and costly than numerical analysis but the results tend to be more reliable for certain variables. If the numerical results are in good correlation with the experimental data, the numerical procedure can be applied to other problems which can be described with the same mathematical model as the verified one, with greater confidence and certainty.

1.1 Axial Turbo Compressors

Turbomachines are all devices that transfer energy to or from a continuously flowing fluid [7]. If in a turbomachine energy is transferred from the flowing fluid to the turbomachine then this turbomachine is classified as a turbine. In the opposite case, when energy is transferred from the turbomachine to the flowing fluid, the turbomachine is classified as either a pump or a compressor. They are not only classified in terms of energy transfer but also in terms of flow direction of the fluid inside the device. If the general flow direction is parallel to the axis of the turbomachine, then that turbomachine is classified as an axial one. A turbomachine where the fluid flow direction is perpendicular to the axis is classified as radial. The flow direction can also be both parallel with the axis and perpendicular to the axis in different parts of the turbomachine. In this case, that turbomachine is classified as a mixed flow turbomachine.

Turbomachines play an important role in modern industry. Turbines have a huge role in energy production, pumps are crucial in water supply and industrial applications. Axial turbo compressors are used to deliver large quantities of gasses. They are usually paired with gas turbines, used in energy production and jet engines.

The energy transfer occurs in a part of the turbomachine called the rotor. As it name implies the rotor is a rotating component. Another component of most turbomachines is the stator. In compressors, the stator's role is to transform kinetic energy of the fluid flow into an increase of static pressure. In turbines the stator has the opposite role. Some turbomachines such as some types of pumps have a diffuser instead of a stator whereas some do not have one at all, such as wind turbines and fans. The combination of a stator and a rotor creates a stage of

a turbomachine. Both stators and rotors consist of blades. When the fluid flows around the blade of either a rotor or a stator the flow properties change. Main goal of rotor and stator blades is changing the flows direction. The profile of rotor and stator blades is referred to as aerofoil and is similar to the profile of wings, although the full shape of a rotor or stator blade is much complex than the shape of a wing. Understanding the flow around an two dimensional aerofoil is fundamental to understanding how a turbomachine works. Flow around an aerofoil is explained in detail in most books dealing with fluid mechanics, for example [9] or [11], or turbomachinery, such as [7] and [12]. Since aerofoil flow is also discussed in undergraduate fluid mechanics classes it will not be further discussed here.

In 1901. Sir Charles Parsons built the first axial turbo compressor [13]. Sir Parsons patented the idea of a *reversed reaction turbine* in 1884. [7]. Although this *reversed turbine* was not the most efficient machine it was popular in steel mills with its constant delivery of oil free air, which was an advantage over the reciprocating compressors used beforehand. Due to it's low efficiency the use of Parsons' compressors was abandoned in favour of multi-stage centrifugal compressor [7]. Surge in the development of axial turbo compressors came after World War II along with the development of jet engines, which axial turbo compressors are part of.

The goal of an axial turbo compressor is to increase the pressure of the fluid. The rotating rotor blades increase the total energy of the fluid flow. The flow then enters the stator blades. Stator blades are shaped so that the space between the blades forms a divergent channel. For a subsonic flow in a divergent channel the speed is decreased, but the pressure is increased [11]. Increasing the pressure through the compressor causes a positive pressure gradient. The positive pressure gradient can cause flow detachment from the blades. Flow detachment causes the efficiency of the compressor to drop. Severe flow detachment will cause stall which can completely break the flow inside the machine [7]. Therefore, the pressure in a single stage of an axial turbo compressor can not be increased too much. In order to achieve a desired higher pressure gain, axial turbo compressor will have multiple stages. Through the multiple stages the flow must be smoothly guided from stage to stage. The exit angle from one blade row must be so that the fluid enters the next row of blades at the inlet angle of that row. In other words, the angle between the flow and the blade at it's inlet must be zero. Often an additional row of stator will be placed before the first rotor. It is referred to as Inlet Guide Vane (IGV). The role of inlet guide vanes is to direct the fluid so it enters the first rotor at an optimal angle.

Besides flow detachment from the blades there is other phenomena which occurs inside an axial turbo compressor that causes the decrease in efficiency. This phenomena can be grouped into two categories. The first group of losses is typical for any application of aerofoils and besides flow detachment it includes boundary layer losses, loss at the trailing edge and losses due to shock waves. The second group is caused by secondary flows inside the compressor. Boundary layer losses are caused by the viscosity of the fluid. Losses at the trailing edge occur due to the fact that there is pressure and suction side of the aerofoil. These two sides

have different flow properties and when the flow exits the aerofoil the flow from the suction side mixes with the flow from the pressure side. Mixing of two flows with different properties causes an increase of entropy which lowers the efficiency. Shock waves also cause an increase of entropy and they occur when the Mach number is one. Tip leakage is the most prominent of secondary flows inside axial turbo compressors. It occurs in a gap between blade tip and endwall [14]. A gap is necessary to allow for the machine to rotate, but in order to lower the tip leakage flow the gap must be made as small as possible. Sometimes inside the tip leakage flow a tip vortex appears. There are other types of vortices that occur inside an axial turbo compressor, passage vortices, blade vortices and Coriolis vortices [15]. They are all responsible for secondary flows inside the machine.

Along with high efficiency, one demand for modern machines is high flexibility. An axial turbo compressor is usually designed to deliver a certain quantity of fluid, a certain mass flow, to a certain level of pressure. The level of pressure is designated as a ratio of the total pressure at the outlet of the compressor and the total pressure at the inlet of the compressor. Outside the operating point with the mass flow and total pressure ratio the compressor was designed for, the flow patterns inside the compressor change. The angle at which the fluid enters a blade changes and the flow is less than optimal. Any type of turbomachine can be operated with different angular velocities. For a single angular velocity changing the total pressure ratio by affecting the conditions downstream of an axial turbo compressor will change the mass flow it delivers. Along with that the efficiency of the machine will change. Also for a single angular velocity there is an operating point at which the compressor performs at peak efficiency. Connecting the operating points with peak efficiency for various angular velocities creates the operational line [7]. In order to achieve optimal performance the compressor should operate in operating points that are on this line. At a single angular velocity there are two extreme operating points which define the limits of a compressors operating range. The first is defined by the maximum mass flow rate which the compressor can deliver. In this operating point the compressor is working in choke operating conditions. The mass flow can not be further increased beyond this point due to the Mach number being one across the section with the minimum flow area [7]. The other extreme operating point is the one in which a compressor achieves its maximum total pressure ratio. At this operating point stall occurs at the blades. Stall can be either part-span stall in which only a part of the blade is stalled or a full-span stall in which the whole blade is stalled. In the stall operating point compressor blades are fully loaded and might get damaged due to additional fatigue and pressure oscillations. Combining choke and stall operating points for different angular velocities creates two lines which bound the compressor's operating range. Caution is required when operating an axial turbo compressor especially during start up in order not to damage the machine, disturb the flow inside the machine and to operate at the highest possible efficiency.

1.2 Computational Fluid Dynamics

Development of CFD started in the early 1960's [16]. First applications of CFD were in the aeronautical industry followed by the automotive industry [16]. Today CFD analysis is regularly used in many different engineering disciplines with an ever expanding range of applications.

In order to solve partial differential equations, which constitute the mathematical model describing a flowing fluid, using numerical simulations, the equations must be discretized in the spatial and temporal domain. After both operations have been performed, a set of linear algebraic equations is obtained. A set of linear algebraic equations is suitable for solving via a computer. Of numerous techniques for spatial discretization the most used in CFD is the Finite Volume Method (FVM). In the FVM the spatial domain is separated into polyhedral control volumes which are called cells. Physical properties are usually calculated for cell centres, and their distribution inside the cell is considered linear. To calculate some terms in the discretized equations, values in face centers of cells are required. To obtain those values some kind of interpolation from cell centre values is required. A various number of interpolation methods is available and they have a significant influence on the results. Spatial domain discretized with control volumes is called numerical mesh and the process of generating a numerical mesh is called meshing. A numerical mesh not only allows for partial differential equations to be discretized as algebraic equations but also contains the information about the geometry surrounding the flow.

For this thesis, the community driven fork of open source CFD software OpenFOAM called `foam-extend` is used [1]. With open source software the code is available to the user, allowing him to learn how it works and write new code for his own purposes. All this is beneficial for both individuals who are beginners in CFD and those who are experienced and trying to push the envelope.

1.3 Thesis Outline

Section 2 presents the governing equations of compressible fluid flow inside an axial compressor. Along with the main conservation laws and turbulence modelling the Multiple Reference Frame (MRF) method, boundary conditions and also methods for connecting non-conformal meshes are described. Section 3 shows the geometry of the Inversely Designed Aachen Compressor (IDAC) and describes the process of spatial discretization of the compressor's geometry. In Section 4 results of the numerical simulations for four different operating points are presented. At the end of the thesis, Section 5 gives final remarks.

2   Mathematical model

The mathematical model the simulation of a steady compressible turbulent fluid flow in an axial turbocompressor is based on the laws of conservation of physical properties significant for the given problem. Conservation laws are a staple of continuum mechanics and the backbone of engineering practice. Along with conservation laws, constitutive equations provide additional required relations so the mathematical model can be solved.

Most flows studied in CFD can be divided into two categories: incompressible and compressible flows. For incompressible flow the change of density can be neglected as it is minimal and does not significantly affect the solution of a numerical simulation. Of course there are problems where the change of density must be taken into account. The most prominent criteria in categorizing the flow as incompressible or compressible is the Mach number. A more detailed classification of fluid flows depending on the Mach number is given in Table 1. The flow inside most axial turbo compressors must be considered compressible.

Table 1: Flow classification based on Mach number [17].

Flow Type	Mach Number
Low Subsonic	0 - 0.3
High Subsonic	0.3 - 0.6
Transonic	0.6 - 1.1
Supersonic	1 - 5
Hypersonic	>5

2.1   Introduction

This section covers the necessary mathematical expressions required to describe the flow inside an axial turbo compressor. First the concept of the scalar transport equation is introduced. Then from the scalar transport equations the mass conservation law, the linear momentum conservation law and the energy conservation law are derived. The energy conservation equation is replaced by the rothalpy conservation equation. Rothalpy is a flow property characteristic to turbomachines. After explaining the phenomena of turbulence and the need for turbulence modelling, the $k - \omega$ SST turbulence model is introduced. In order to obtain a steady state solution for the flow inside a turbomachine the MRF model is used [2].

For a system of partial differential present to have an unique solution, boundary conditions are necessary. Three basic categories of numerical boundary conditions as well as two types of specific boundary conditions are explained. Finally, due to turbomachines having complex geometries, their numerical meshes are often disjointed. To connect the two disjointed regions of the numerical mesh, two different methods are used in this thesis and explained in this section, mixing plane [4] and General Grid Interface (GGI) [3].

2.2   Governing Equations of Compressible Fluid Flow

Conservation laws describe transport of a certain property. The scalar transport equation describes the transport of an arbitrary scalar variable and is usually presented as a starting point for deriving relevant conservation laws to a given problem in fluid mechanics. In its standard form, the scalar transport equation models convective transport, diffusive transport and volume source and/or sink terms which are typical for conservation laws [18]. The standard form is expressed as:

$$\frac{\partial \phi}{\partial t} + \nabla \bullet (\phi \mathbf{u}) - \nabla \bullet (\gamma \nabla \phi) = q_v, \tag{1}$$

where ϕ represents the transported arbitrary scalar variable, (u) is the convective velocity and γ is the diffusion coefficient. On the right hand side of Eq. (1) the term q_v represents either a sink or source of the transported scalar variable. A sink or a source accounts for the non-transport effects such as local volume production or destruction of the transported scalar variable.

All of the four terms in Eq. (1) represent specific physical phenomena, which is as follows:

- term $\partial \phi / \partial t$ is the temporal derivative and describes the inertia of the isolated system,

- term $\nabla \bullet (\phi \mathbf{u})$ is the convection term. It represents the transport of scalar ϕ by the convective velocity $\mathbf{u}$. The convective transport is of hyperbolic nature,

- term $\nabla \bullet (\gamma \nabla \phi)$ is the diffusion term. This term represents transport of variable ϕ due to the existence of a spatial gradient. The nature of this term is elliptic, which means that every point inside the domain is influenced by every other point inside the domain,

- term q_v represents sources and sinks which account for non-transport effects and describe the local volume production or destruction of scalar ϕ.

Relevant conservation laws, that make the governing equations of fluid flow can be derived by substituting the transported scalar property ϕ with a any transported property.

2.2.1   Conservation of Mass

Conservation of mass is one of the basic principles of continuum mechanics. The equation for mass conservation, or the continuity equation can be simply derived from Eq. (1) by substituting arbitrary scalar variable ϕ with fluid density ρ and setting the source term to zero:

$$\frac{\partial \rho}{\partial t} + \nabla \bullet (\rho \mathbf{u}) = 0. \tag{2}$$

In continuum mechanics mass is not transferred into energy. Mass also is not transported by diffusion so the diffusion term is absent in Eq. (2).

2.2.2 Conservation of Linear Momentum

In order to derive the equation for conservation of linear momentum scalar variable ϕ is replaced by the product of fluid density and velocity field $\rho\mathbf{u}$,

$$\frac{\partial(\rho\mathbf{u})}{\partial t} + \nabla \bullet (\rho\mathbf{u} \otimes \mathbf{u}) = \rho\mathbf{g} + \nabla \bullet \boldsymbol{\sigma}. \tag{3}$$

In Eq. (3) the convective term $\rho\mathbf{u} \otimes \mathbf{u}$ is non-linear since the solution depends on itself. Due to its non-linearity it is difficult to solve and it is usually the main cause of flow instabilities.

The source terms on the right hand side of Eq. (3) represent the sum of mass force ($\rho\mathbf{g}$) and body forces ($\nabla \bullet \boldsymbol{\sigma}$). The body forces are represented by the Cauchy stress tensor $\boldsymbol{\sigma}$, which is the sum of static pressure p and viscous stress tensor τ written as:

$$\boldsymbol{\sigma} = -p\mathbf{I} + \boldsymbol{\tau}, \tag{4}$$

where $\mathbf{I}$ is the identity or unit tensor.

For a Newtonian fluid the viscous stress tensor τ is expressed as:

$$\boldsymbol{\tau} = 2\mu\mathbf{D} - \frac{2}{3}\mu\left(\nabla \bullet \mathbf{u}\right)\mathbf{I}. \tag{5}$$

In Eq. (5) μ represents the dynamic viscosity and $\mathbf{D}$ is the symmetric part of the velocity gradient tensor which is formulated as following:

$$\mathbf{D} = \frac{1}{2}\left[\nabla\mathbf{u} + (\nabla\mathbf{u})^T\right]. \tag{6}$$

Substituting Eq. (4), Eq. (5) and Eq. (6) back into Eq. (3), results in:

$$\frac{\partial(\rho\mathbf{u})}{\partial t} + \nabla \bullet (\rho\mathbf{u} \otimes \mathbf{u}) = \rho\mathbf{g} - \nabla\left(p + \frac{2}{3}\mu\nabla \bullet \mathbf{u}\right) + \nabla \bullet \left[\mu\left(\nabla\mathbf{u} + (\nabla\mathbf{u})^T\right)\right]. \tag{7}$$

The momentum equation (Eq. (3), Eq. (7)) is a vector equation and as such it can be decomposed into three scalar differential equations, each for one spatial component of the velocity vector. These three scalar partial differential equations are known as the Navier-Stokes equations.

2.2.3 Conservation of Energy

The first law of thermodynamics is the conservation of energy law. The form of the total energy conservation equation is derived by substituting the scalar variable ϕ with the product of fluid

density ρ and specific total energy e:

$$\frac{\partial(\rho e)}{\partial t} + \nabla \bullet (\rho e\mathbf{u}) = \rho\mathbf{g}\cdot\mathbf{u} + \nabla \bullet (\boldsymbol{\sigma}\cdot\mathbf{u}) - \nabla \bullet \mathbf{q} + \rho Q, \tag{8}$$

where total energy e is sum of internal energy u and kinetic energy:

$$e = u + \frac{1}{2}(\mathbf{u}\cdot\mathbf{u}). \tag{9}$$

In Eq. (8) Q is a volumetric heat source and $\mathbf{q}$ is the heat flux vector. The heat flux vector $\mathbf{q}$ is formulated by the Fourier's law as following:

$$\mathbf{q} = -\lambda\nabla T, \tag{10}$$

in which λ is thermal conductivity, a property of any material dependant on its thermodynamic state. Thermal conductivity can be expressed as a function of static pressure p and absolute temperature T:

$$\lambda = \lambda(p,T). \tag{11}$$

Molecular viscosity μ can also be expressed as a function of static pressure p and absolute temperature T:

$$\mu = \mu(p,T). \tag{12}$$

In this mathematical model for compressible flow inside an axial turbo compressor, both thermal conductivity λ and molecular viscosity μ are considered constant.

The equation of total energy conservation (Eq. (8)) is weakly coupled to the rest of the mathematical model [18]. Through an equation of state any gas property can be expressed as a function of other gas properties. Fluid density ρ can be expressed as a function of static pressure p and absolute temperature T as well.

$$\rho = \rho(p,T). \tag{13}$$

The air flowing inside the compressor is considered ideal. With this assumption fluid density ρ can expressed using the equation of state for ideal gases:

$$\rho = \frac{p}{RT} = \psi p, \tag{14}$$

where R represents the individual gas constant and ψ is compressibility:

$$\psi = \frac{1}{RT} \tag{15}$$

Taking into account Fourier's law, Eq. (10) and relations for the Cauchy stress tensor, Eq. (8) is expanded as follows:

$$
\begin{aligned}
\frac{\partial(\rho e)}{\partial t} + \nabla \bullet (\rho e \mathbf{u}) =& \rho \mathbf{g} \cdot \mathbf{u} - \nabla \bullet (p \mathbf{u}) - \nabla \bullet \left(\frac{2}{3} \mu \left(\nabla \bullet \mathbf{u} \right) \mathbf{u} \right) + \\
&+ \nabla \bullet \left(\mu \left(\nabla \mathbf{u} + (\nabla \mathbf{u})^T \right) \cdot \mathbf{u} \right) + \nabla \bullet (\lambda \nabla T) + \rho Q.
\end{aligned}
\tag{16}
$$

When dealing with open thermodynamic systems and compressible flow calculations, use of enthalpy is preferred over the use of internal energy. The correlation between internal energy and enthalpy follows:

$$h = u + \frac{p}{\rho} \tag{17}$$

Specific total enthalpy, similar to total energy takes into account kinetic energy. Relationship between the specific total enthalpy and specific total energy is derived in the following way:

$$h_0 = h + \frac{1}{2} (\mathbf{u} \cdot \mathbf{u}) = u + \frac{p}{\rho} + \frac{1}{2} (\mathbf{u} \cdot \mathbf{u}) = e + \frac{p}{\rho}. \tag{18}$$

Applying the relations from Eq. (18) to Eq. (8) gives the following form of total enthalpy conservation equation:

$$\frac{\partial(\rho h_0)}{\partial t} - \frac{\partial p}{\partial t} + \nabla \bullet (\rho \mathbf{u} h_0) = \rho \mathbf{g} \cdot \mathbf{u} + \nabla \bullet (\sigma \cdot \mathbf{u}) - \nabla \bullet \mathbf{q} + \rho Q. \tag{19}$$

Even though Eq. (19) is the preferred formulation of energy conservation law for compressible flows a new variable more adequate for flows inside turbomachines will be introduced. This newly introduced variable is called rothalpy. Rothalpy is derived combining Euler turbomachinery equation and the first law of thermodynamics [12] and is defined as:

$$i = h_0 - \omega r u_\Theta, \tag{20}$$

where r is radius, ω is the angular velocity, u_Θ is the tangential component of absolute velocity and h_0 is of total enthalpy. Rothalpy, being constant over a streamline, is conserved inside a rotor or a stator of the turbomachine, but not over the stage. The exact formulation of the rothalpy conservation equation depends on the formulation of MRF method. There are two ways MRF can be formulated, utilizing either the relative velocity or the absolute velocity. If the MRF method is formulated via the absolute velocity, the rothalpy conservation equation

has the following definition [19]:

$$\nabla \bullet (\rho i\mathbf{u}_{\text{rel}}) = -\nabla \bullet (\rho \omega r u_{\Theta} \mathbf{u}_{\text{rel}}) - \nabla \bullet (p\mathbf{u}) + \nabla \bullet (\boldsymbol{\tau} \cdot \mathbf{u}) + \nabla \bullet (\lambda \nabla T) + S_{\text{H}}, \qquad (21)$$

in which $\mathbf{u}_{\text{rel}}$ is the relative velocity vector and S_{H} the source term of enthalpy. Otherwise if the formulation of MRF method utilizing the relative velocity is applied, two terms $-\nabla \bullet (\rho \omega r u_{\Theta} \mathbf{u}_{\text{rel}})$ and $-\nabla \bullet (p\mathbf{u})$, are left out and the conservation of rothalpy equation is the following:

$$\nabla \bullet (\rho i\mathbf{u}_{\text{rel}}) = \nabla \bullet (\boldsymbol{\tau} \cdot \mathbf{u}) + \nabla \bullet (\lambda \nabla T) + S_{\text{H}}. \qquad (22)$$

Angular velocity ω is equal to zero in stator, while the rotor will have an angular velocity different from zero. Looking at Eq. (20) it is obvious that there will be a difference between the rothalpy of a rotor and stator inside a single stage. This difference, usually referred as the rothalpy jump, equals:

$$\Delta i = -\omega r \mathbf{u}_{\Theta}, \qquad (23)$$

and must be accounted for by the rotor-stator interface. If the jump in rothalpy between the rotor and the stator is not respected, a continuous evaluation of enthalpy h and absolute temperature T is not possible [20].

2.3 Turbulence modelling

Turbulent fluid flow is characterized by apparently random and chaotic three-dimensional vorticity. Most real life flows are turbulent flows. The presence of turbulence increases the energy dissipation, mixing, heat transfer, and drag. An essential characteristic of turbulence is the generation of new vortices from old [21]. The vortices with the biggest diameter and most kinetic energy are usually generated by the domain shape. They brake down into smaller vortices of smaller kinetic energy. The process of vortex decomposition continues until the energy of the smallest vortices is dissipated into heat via viscous effects.

Even though chaotic and random, turbulent flow is fully described by the governing equations of fluid flow presented so far. Resolving the equations as they are now would require extremely high computational resources. To facilitate this, turbulence modelling is utilized to provide physical results within a reasonable requirement for computational resources.

The Reynolds Averaged Navier-Stokes Equations (RANS) turbulence modelling is based on averaging out the governing equations [21]. For compressible flows Favre-Averaging is used instead of Reynolds-Averaging in order to account for density fluctuations [22]. A general temporary dependant variable Φ can be decomposed into a mean and fluctuating part as follows:

$$\Phi = \widetilde{\Phi} + \Phi'', \tag{24}$$

where $\widetilde{\Phi}$ is the Favre-Averaged density-weighted variable can be expressed as:

$$\widetilde{\Phi} = \frac{\overline{\rho\Phi}}{\overline{\rho}}. \tag{25}$$

Overbars in Eq. (25) denote Reynolds-Averaging.

Applying Favre-Averaging and Reynolds-Averaging to Eq. (2) and Eq. (3) yields the following averaged out forms of the mass conservation law and linear momentum conservation law:

$$\frac{\partial \overline{\rho}}{\partial t} + \nabla \bullet (\overline{\rho}\,\widetilde{\mathbf{u}}) = 0, \tag{26}$$

$$\frac{\partial \overline{\rho}\,\widetilde{\mathbf{u}}}{\partial t} + \nabla \bullet (\overline{\rho}\,\widetilde{\mathbf{u}} \otimes \widetilde{\mathbf{u}}) = \nabla \bullet \overline{\sigma} + \overline{\rho}\mathbf{g} + \nabla \bullet \mathbf{R}. \tag{27}$$

After applying Favre-Averaging and Reynolds-Averaging a fluctuating part remains in Eq. (27). This fluctuating part is encompassed in the Reynolds stress tensor $\mathbf{R}$ which is formulated as follows:

$$\mathbf{R} = -\overline{\rho\mathbf{u}'' \otimes \mathbf{u}''}. \tag{28}$$

The Reynolds stress tensor introduces new unknown variables which in order to solve the system of equations are additionally modelled. Today there is a plethora of turbulence models for various applications. Within this thesis the $k - \omega$ SST turbulence model is used.

2.3.1 $k - \omega$ SST Turbulence model

The $k - \omega$ SST turbulence model is a two-equation turbulence model based on the Boussinesq's eddy viscosity hypothesis. The transport of turbulent kinetic energy k is defined as:

$$\frac{\partial \overline{\rho}k}{\partial t} + \nabla \bullet (\overline{\rho\widetilde{\mathbf{u}}}k) - k\nabla \bullet (\overline{\rho\widetilde{\mathbf{u}}}) = \min\left(G,\, c_1\beta^* k\omega\right) - \beta^*\rho\,\omega k, \tag{29}$$

and ω, eddy turn-over time, is defined by:

$$\frac{\partial \overline{\rho}\omega}{\partial t} + \nabla \bullet (\overline{\rho}\widetilde{\mathbf{u}}\omega) - \omega\nabla \bullet (\overline{\rho}\widetilde{\mathbf{u}}) - \nabla \bullet (\Gamma_{k,\text{eff}}\nabla\omega) =$$

$$\gamma \min\left(S_2, \frac{c_1}{a_1}\beta^*\omega \max\left(a_1\omega, \ b_1 F_{23}\sqrt{S_2}\right)\right) - \beta\overline{\rho}\omega^2 + (1-F_1)CD_{k,\omega} \quad (30)$$

Effective diffusion coefficients for both turbulent kinetic energy k and eddy turn over time ω are defined respectively:

$$\Gamma_{k,\text{eff}} = \alpha_k\mu_t + \mu, \quad (31)$$

$$\Gamma_{\omega,\text{eff}} = \alpha_\omega\mu_t + \mu, \quad (32)$$

as a function of molecular dynamic viscosity μ and eddy viscosity μ_t which is calculated as:

$$\mu_t = \frac{\overline{\rho}a_1 k}{\max\left(a_1\omega, \ b_1 F_{23}\sqrt{2}\left(\frac{1}{2}\left(\nabla\widetilde{\mathbf{u}} + (\nabla\widetilde{\mathbf{u}})^T\right)\right)\right)}. \quad (33)$$

On the right hand side of Eq. (29) the production of turbulent kinetic energy is obtained from the following equation:

$$G = 2\left(\frac{1}{2}\left(\nabla\widetilde{\mathbf{u}} + (\nabla\widetilde{\mathbf{u}})^T\right)\right)^2 \mu_t. \quad (34)$$

In Eq. (30) the term $CD_{k,\omega}$ is evaluated by:

$$CD_{k,\omega} = \max\left(2\overline{\rho}\alpha_{\omega,2}\frac{\nabla k \bullet \nabla\omega}{\omega}, 10^{-10}\right). \quad (35)$$

Since the $k-\omega$ SST combines two different turbulence models, $k-\varepsilon$ model and Wilcox's $k-\omega$ model, blending functions are required for a smooth transition between those two models. Blending functions are defined by the following equations:

$$F_1 = \tanh\left(\left(\min\left(\min\left(\max\left(\frac{\sqrt{k}}{\beta^*\omega y}, \frac{500\nu}{y^2\omega}\right), \frac{4\alpha_{\omega,2}k}{CD_{k,\omega+}y^2}\right), 10\right)\right)^4\right) \quad (36)$$

$$F_2 = \tanh\left(\left(\min\left(\max\left(\frac{2\sqrt{k}}{\beta^*\omega y}, \frac{500\nu}{y^2\omega}\right), 100\right)\right)^2\right) \quad (37)$$

In order for the blending functions to be properly defined, a number of parameters have to be defined. The following expressions are used to calculate this parameters:

$$\alpha_k = F_1 \left(\alpha_{k,1} - \alpha_{k,2} \right) + \alpha_{k,2} \tag{38}$$

$$\alpha_\omega = F_1 \left(\alpha_{\omega,1} - \alpha_{\omega,2} \right) + \alpha_{\omega,2} \tag{39}$$

$$\beta = F_1 \left(\beta_1 - \beta_2 \right) + \beta_2 \tag{40}$$

$$\gamma = F_1 \left(\gamma_1 - \gamma_2 \right) + \gamma_2 \tag{41}$$

Coefficients presented in Table (2) are fine-tuned so the model can capture the actual physical behaviour as accurate as possible.

Table 2: $k - \omega$ SST TURBULENCE MODEL COEFFICIENTS.

$\alpha_{k,1}$	$\alpha_{k,2}$	$\alpha_{\omega,1}$	$\alpha_{\omega,2}$	β_1	β_2	β^*	γ_1	γ_2	a_1	b_1	c_1
0.85	1.0	0.5	0.856	0.075	0.0828	0.09	5/9	0.44	0.31	1.0	10.0

2.4 Multiple Frames of Reference

If a part of the modelled geometry is rotating, as is the case in axial turbo compressors, Multiple Reference Frame (MRF) model is used to obtain a steady-state solution although the numerical mesh is not moving. Additional inertia terms are added to the governing equations to model the rotational movement. Because of the geometry not moving, MRF model is often referred to as the *frozen rotor approach*. Not moving the geometry significantly lowers the demand for computational resources and even though results obtained with the MRF model are only an approximation of transient flow they are, in certain cases, sufficiently accurate.

For a position vector in an inertial frame, a relationship to a vector in the moving reference frame is established in the following way:

$$\left[\frac{d\mathbf{r}}{dt} \right]_I = \left[\frac{d\mathbf{r}}{dt} \right]_R + \omega \times \mathbf{r}, \tag{42}$$

where ω is the angular velocity vector and subscripts I and R denote the inertial and rotating frame. From mechanics it is known that the differentiation of a position vector with respect to time equals velocity. Considering this fact, Eq. (42) can be written in the following form:

$$\mathbf{u} = \mathbf{u}_{rel} + \omega \times \mathbf{r}. \tag{43}$$

Eq. (43) gives the relationship between the absolute velocity in the fixed inertial frame and the relative velocity in the rotating frame of reference.

In OpenFOAM the absolute velocity formulation of MRF is used. For the compressible MRF model the conservation of mass is expressed with following equation:

$$\frac{\partial \rho}{\partial t} + \nabla \bullet (\rho \mathbf{u}) = 0. \tag{44}$$

By using the absolute velocity formulation there less source terms for inertial forces appear in momentum equation. The convective term in the linear momentum equation is calculated using the relative velocity,

$$\frac{\partial (\rho \mathbf{u})}{\partial t} + \nabla \bullet (\rho \mathbf{u}_{\text{rel}} \otimes \mathbf{u}) + \omega \times (\rho \mathbf{u}) = -\nabla p + \nabla \bullet \boldsymbol{\tau} + \rho \mathbf{g}, \tag{45}$$

but the viscous stress tensor $\boldsymbol{\tau}$ is defined same as for a stationary reference frame (given by Eq. (5)),

$$\boldsymbol{\tau} = \mu \left(\nabla \mathbf{u} + (\nabla \mathbf{u})^T \right) - \frac{2}{3} \mu \nabla \bullet (\mathbf{u}) \, \mathbf{I}. \tag{46}$$

Because the absolute velocity formulation of MRF is applied, the following rhotalpy conservation equation shall be used:

$$\nabla \bullet (\rho i \mathbf{u}_{\text{rel}}) = -\nabla \bullet (\rho \omega r u_{\Theta} \mathbf{u}_{\text{rel}}) - \nabla \bullet (p \mathbf{u}) + \nabla \bullet (\boldsymbol{\tau} \cdot \mathbf{u}) + \nabla \bullet (\lambda \nabla T) + S_{\text{H}}. \tag{47}$$

2.5 Boundary Conditions

In order for a system of partial differential equations to have a unique solution it has to have defined boundary conditions. Boundary conditions are also used to isolate the space for which the numerical simulation is performed from its surroundings [18]. They have to be prescribed for each variable on domain boundaries. Prescribing boundary conditions requires an understanding of the investigated problem.

Numerical boundary conditions are imposed at the equation level. They can be categorized as:

- Dirichlet boundary condition, which gives a fixed value for the transported scalar variable ϕ on the specified boundary

- Neumann boundary condition, which specifies the gradient of the transported scalar variable ϕ normal to the boundary. Commonly the gradient at the boundary is set to zero gradient (no flux).

– Mixed boundary condition is a boundary condition that is linear combination of the two mentioned numerical boundary conditions, Dirichlet and Neumann.

Besides numerical boundary conditions there are boundary conditions which allow a simplification and reduction of the computational domain which decreases the required computational resources. These boundary conditions are:

– Symmetry plane, which can be used when the investigated geometry is symmetrical. The flow must be steady and the expected flow pattern also must be symmetrical. If the problem satisfies all these conditions then only a part of the *original* domain can be modelled.

– Cyclic or periodic boundary conditions are used when the geometry consists of identical repeating parts, where one part can represent the whole geometry. A great example where this boundary condition is commonly applied are turbomachinery simulations. With the application of a cyclic boundary condition the flow within a single blade is modelled instead of the full annulus of a blade row.

In OpenFOAM boundary conditions are specified on objects called patches.

2.6 Rotor-Stator Interface Modelling

In general, the geometry of a turbomachine is complex. In most cases the complexity stems from the shape of blades. It is difficult to generate a numerical mesh of satisfactory quality for the entire turbomachine due to its complex geometry. Instead, the mesh is split into regions. If for example a single passage of a single stage axial turbo compressor is simulated then separate numerical meshes are created for both the rotor and the stator. The complete numerical mesh is non-conformal. Understandably, the rotor and stator meshes must be connected in some way. The interpolation between the rotor and the stator meshes can either be direct or averaged and it is handled over interface patches. Two methods of the rotor-stator interface modelling that are available in `foam-extend` are used within this thesis, the direct `overlapGgi` method and the averaged `mixingPlane`.

Both methods of rotor stator interface modelling must take into account the rothalpy jump between a rotor and a stator of a turbo compressor stage.

2.6.1 Mixing Plane

The basic assumption of the mixing plane approach is that the flow is largely mixed out in the gap between blades [23]. This assumption can be further extended that at the interface between two regions constant pitch-wise conditions can be imposed. Both these assumptions give validity to the procedure of circumferentially averaging flow field variables and then

transferring the averaged variables over the interface [24]. The averaging must at a minimum conserve the mass flow through the regions it connects [25]. Through circumferential averaging, flow variations in the circumferential direction are lost at the interface. They are however intact for the radial direction. The mixing plane interface must allow for backflow to occur [26]. Two types of averaging can be used in the mixing plane method: area averaging and weighted averaging. If both forward and backflow exist at the interface, then the weighted method is not suitable [24]. The uniform circumferential distribution of physical properties is accompanied by their reflection which is caused exactly by the assumption of circumferentially mixed out flow.

2.6.2 General Grid Interface (GGI)

The GGI is a common interface in CFD simulations of turbomachines [3]. In this thesis two derivatives of GGI are used, the `overlapGgi` is used to connect the interface between blade rows of the axial turbo compressor and `cyclicGgi` is used as a periodic boundary condition, which, under the assumption of periodic flow, allows only a single passage of the axial turbo compressor to be simulated. The GGI method of coupling two non-conformal patches is a direct method. Flow values are transferred to the patch pair without averaging of flow values. However, weighting factors must be determined to achieve a conservative discretization across the interface [3]. In essence, the weighting factors used by the GGI are percentages of surface intersection between *neighbour* faces.

    The `overlapGgi` is used in cases when the interface is not fully covered. A regular cyclic boundary condition requires for faces on both sides to match. Since `cyclicGgi` is derived from GGI the two patches can be non-conformal. This allows for a better numerical mesh to be made.

2.7 Closure

In this section the mathematical model describing compressible flow inside an axial turbocompressor was described. The model consists of main conservation laws, conservation of mass, conservation of linear momentum and conservation of energy. The conservation of energy is presented in a form with rothalpy as the transport variable. Turbulence modelling is required to solve the equations of the mathematical model within reasonable computational cost. The $k - \omega$ SST turbulence model is presented. To model the rotation of a turbomachine the MRF method is used. The basic types of boundary conditions were presented as well as methods of connecting non-conformal numerical meshes.

3   IDAC Characteristics and Spatial Domain Discretization

The introduction of numerical methods to the design process of turbomachines allowed for a much more detailed and sophisticated approach which resulted in achieving higher efficiencies and durability. In order to be able to use numerical simulations in the design process of a turbomachine the numerical procedure must be validated against experimental data gathered from an existing machine.

3.1   Introduction

The first part of this section introduces the Inversely Designed Aachen Compressor (IDAC). Even though IDAC was a research compressor, it was designed to have the characteristics of an industrial compressor. After the geometrical and performance characteristics of IDAC are introduced, the process of creating a numerical mesh for a single passage of the compressor is explained. This numerical mesh can be used with the mixing plane rotor-stator interface, but it would be unphysical to use it with the `overlapGgi` interface. For the `overlapGgi` rotor-stator interface, the existing mesh is modified and the differences between the two numerical meshes are shown.
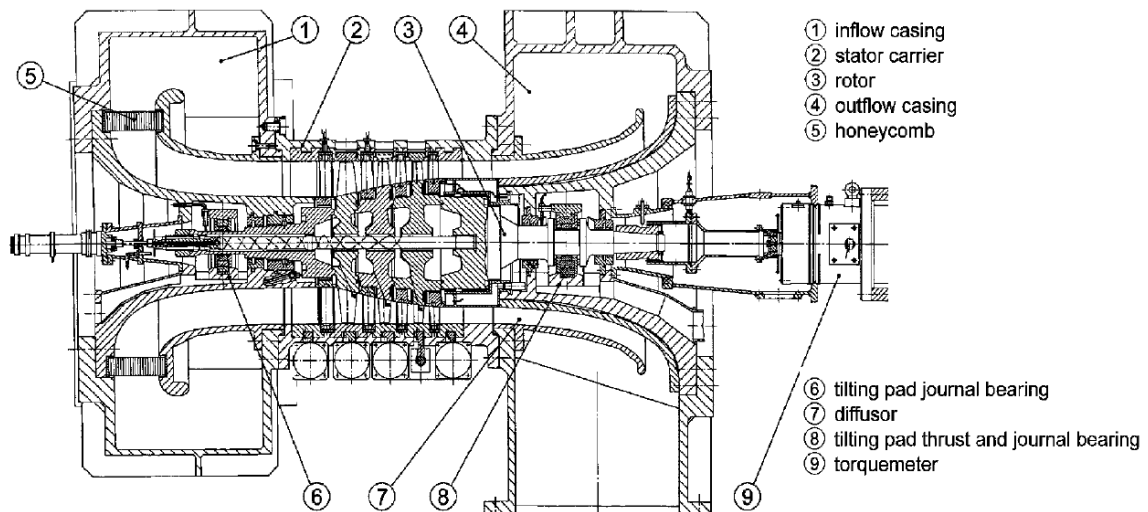
3.2   IDAC Characteristics

Figure 1: CROSS SECTION OF THE IDAC [5].

Figure 1 shows the cross section of IDAC, an axial turbo compressor built at RWTH Aachen University. IDAC is a three stage transonic axial turbo compressor with IGV. The compressor rig is based on a 1.5 stage axial turbo compressor built by Schulte (1994) [27]. The goal of

the project was to investigate unsteady phenomena as well as the upstream and downstream interactions of different stages in a multi-stage turbomachine.

Table 3: IDAC BLADE CHARACTERISTICS[6].

	Inlet Guide Vane	First Stage		Second Stage		Third Stage	
		Rotor	Stator	Rotor	Stator	Rotor	Stator
Number of Blades	38	25	40	31	42	39	46
Chord Length [mm]	32	50	30	38	28	31	26
Blade Height [mm]	86.72	86	71.1	61.18	53.76	47.74	43.68

Blade row characteristics can be found in Table (3). They were all inversely designed by a two dimensional method. The Controlled Diffusion Aerofoils (CDA) are used to shape the blades. The CDA blade shape was designed for subsonic and transonic applications. Usually on an aerofoil surface with the rise of the Mach number local patches of supersonic flow appear. The supersonic flow is then terminated by shock waves. The efficiency loss is not only caused by shock waves but also by the possible boundary layer separation due to shock waves. Through the diffusion process the transition from the supersonic to subsonic flow can be achieved without shock [28]. CDA blades can achieve higher loading due to thicker leading and trailing edge without affecting the overall performance of the compressor [29]. During operation the tip clearance is less than 0.3 millimetres resulting in a relative clearance of 0.35 percent for the blades of the first rotor, 0.49 percent for the second rotor and 0.64 percent for the third rotor [5].
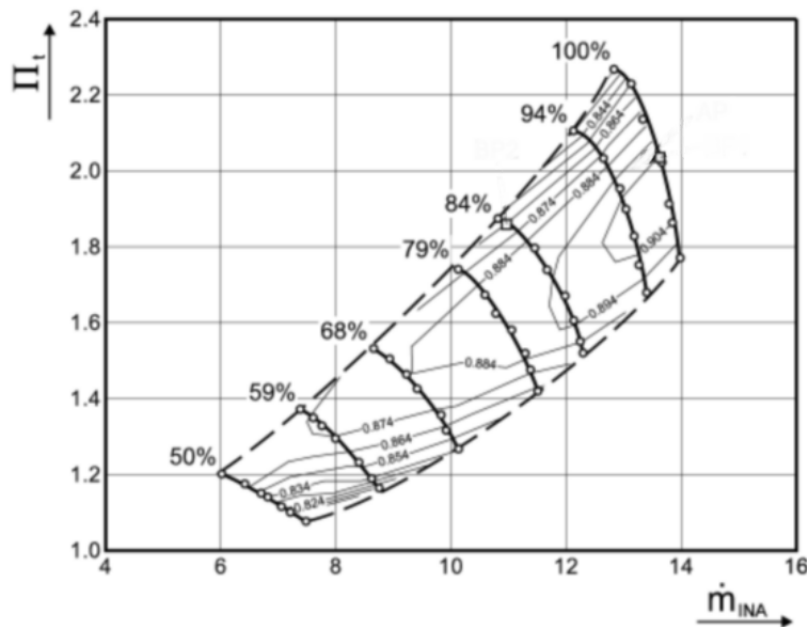

Figure 2: IDAC PERFORMANCE MAP [6].

The compressor operating range is displayed on Figure 2. Figure 2 is the compressor performance map on which values for mass flow are ploted against the total pressure ratio.

The compressor performance also contains adiabatic efficiency isolines. From the compressor map the compressor performance in each operating point can be seen.

Table 4: IDAC DESIGN PARAMETERS [27].

Rotor Speed [min^{-1}]	17000
Mass Flow [kg/s]	13.4
Power Input [kW]	920
Overall Total Pressure Ratio	2.03

Table 4 gives the data for the IDAC design operating point. The compressor is meant to spent most of its operating time in its design point and also achieve the highest efficiency.

Experimental measurements where performed for five different operating points. The first operating point is the design point. Additional measured operating points include the operating points at near-stall conditions at nominal angular velocity, 84 % and 68 % of the nominal angular velocity, as well as an operating point at near-choke conditions for 68 % of the nominal angular velocity. Measurements at these operating points include mass flow rate, total pressure ratio and adiabatic efficiency in order to compare the real compressor performance with the performance calculated during the design process. Along with overall performance of IDAC, the flow field inside the compressor was examined. Three different kinds of pneumatic probes were used to capture the pressure field inside the compressor. A semiconductor pressure transducer was used to obtain the pressure field on the casing wall above the rotor blades [5].

3.3 Numerical Domain Discretization

Spatial domain discretization has significant influence on the result of a CFD simulation. The equations of the mathematical model presented in Section 2 are dicretized in the control volumes of the numerical mesh. The spatial domain must be discretized in such way that it can capture all the relevant flow phenomena. The numerical mesh can either be structured or unstructured or a combination of the two, a so called hybrid mesh. Constructing a structured mesh is more time consuming than constructing an unstructured mesh. With a structured mesh the user has more control over the quality of the mesh. Sometimes, due to the geometry being too complex it is impossible to construct a fully structured mesh. In those cases, the parts where good mesh quality is required are discretized with a structured numerical mesh and the rest with an unstructured numerical mesh. Unstructured numerical meshes usually have more cells than structured meshes and thus higher computational demands.

In this thesis a structured mesh constructed with the Pointwise® is used. The multi-block mesh will consist solely of hexahedral control volumes.
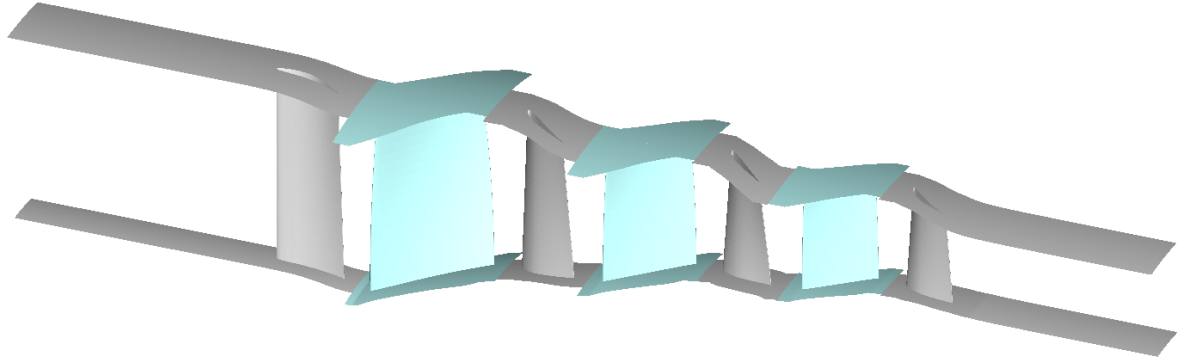
Figure 3: ROTOR (CYAN) AND STATOR (GREY) BLADES, HUB AND SHROUD.

Figure 3 displays the geometry of a single passage. The first blade from the left is the IGV which means the general fluid flow, from the perspective of Figure 3, is from left to right. The surface at the bottom of blades is called the hub, and the surface at the top is called shroud.

Each blade shown in Figure 3 defines its own numerical mesh region. The same grid topology is used for all blades and therefore only one region of the mesh will be displayed in greater detail and that is the region of the first stage rotor blade.
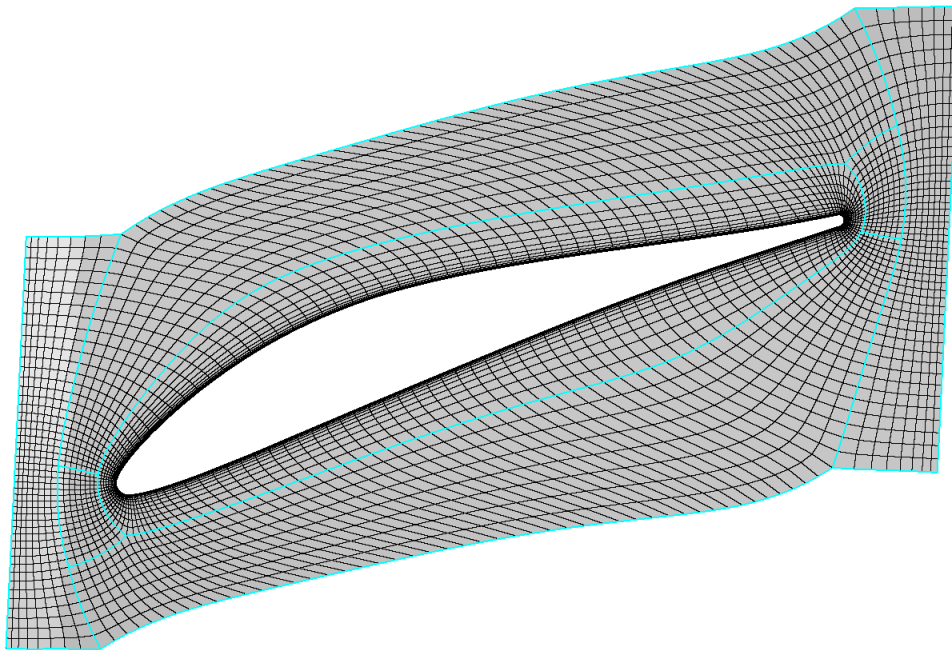

Figure 4: NUMERICAL MESH FOR THE HUB OF THE FIRST STAGE ROTOR.

The cyan lines in Figure 4 represent the border between different cell blocks of the numerical mesh for the first stage rotor hub. Each blade is meshed with the O-H topology. The combination of the O-grid around the blade and H-blocks beyond the blade is optimal for axial turbomachine blades. The separate H-blocks are for the pressure and suction side of the blade, leading and trailing edge of the blade and inlet and outlet of the numerical mesh region

for the first stage rotor. The same mesh topology is used on the shroud of the first stage rotor.
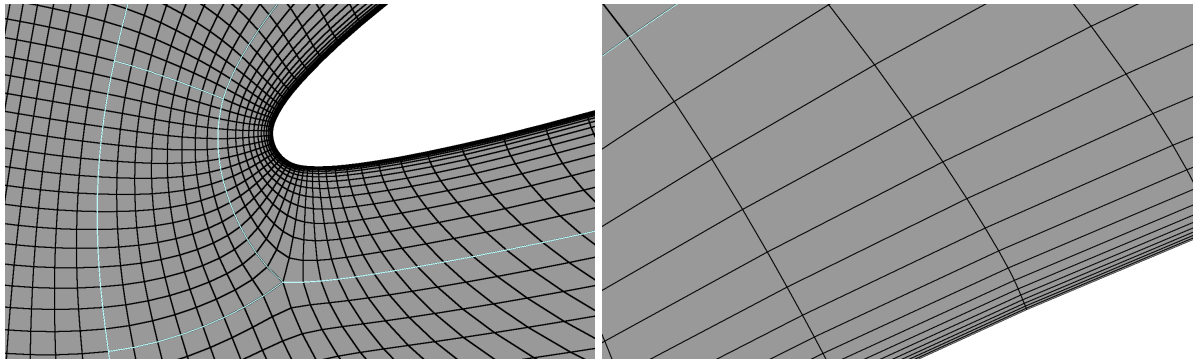
(a) FIRST STAGE ROTOR LEADING EDGE DETAIL.   **(b)** FIRST STAGE ROTOR BOUNDARY LAYER.

Figure 5: MESH DETAILS FOR THE FIRST STAGE ROTOR HUB

The H-block for the leading edge shown in Figure 5a has a higher number of nodes not only to be able to capture the flow phenomena, but also to able to describe the highly curved blade geometry. This also valid for the block at the trailing edge. The boundary layer around the blade was created using normal extrusion from the surface blade mesh. The sixteen boundary layer cells can be seen in Figure 5b.
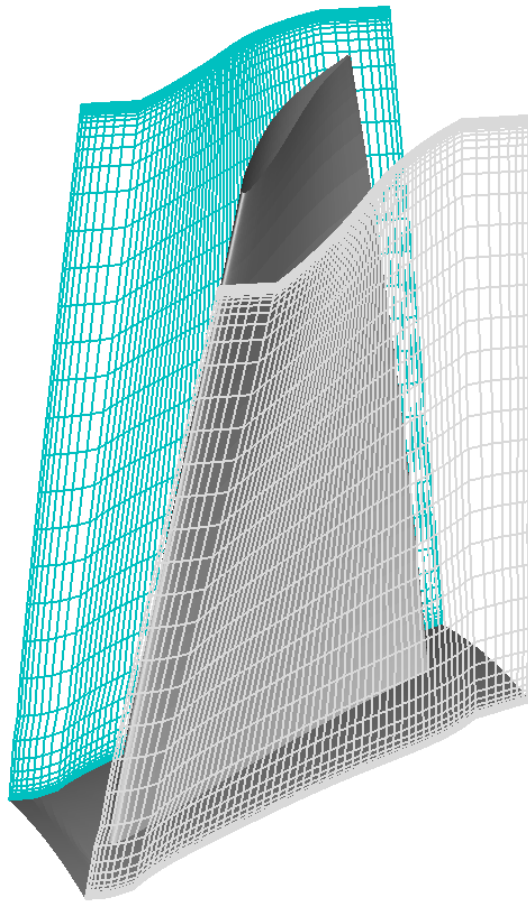

Figure 6: CYCLIC PATCHES.

A single passage means that only the flow around a single blade is computed instead of the whole blade row. This is made possible by the assumption that the flow inside an axial turbo compressor is axisymmetrical. On the sides of the numerical mesh for a single blade passage a cyclic boundary conditions must be used. Figure 6 shows the cyclic boundaries for the first stage rotor. For a cyclic boundary condition the values on the patch are used as boundary conditions for its cyclic partner. The `cyclicGgi` boundary condition allows for the nodes on cyclic patches to be non-conformal. Even if the patches are conformal the `cyclicGgi` boundary condition is more robust than the *regular* cyclic boundary condition.

The tip gap between the blade and the shroud for the first stage rotor is displayed in Figure 7. Only the tip gaps for rotor blade rows have been taken into consideration since for stator blades the difference in pressure between the suction and pressure side is significantly lower. Sometimes the tip gap flow can cause problems in obtaining a converged steady state solution, and in that case both the rotor and stator tip gaps can be neglected. In order to be able to calculate the flow in the tip gap a high number of cells is used. The cells towards the blade tip and the shroud must be equally small to capture the boundary layer phenomena.
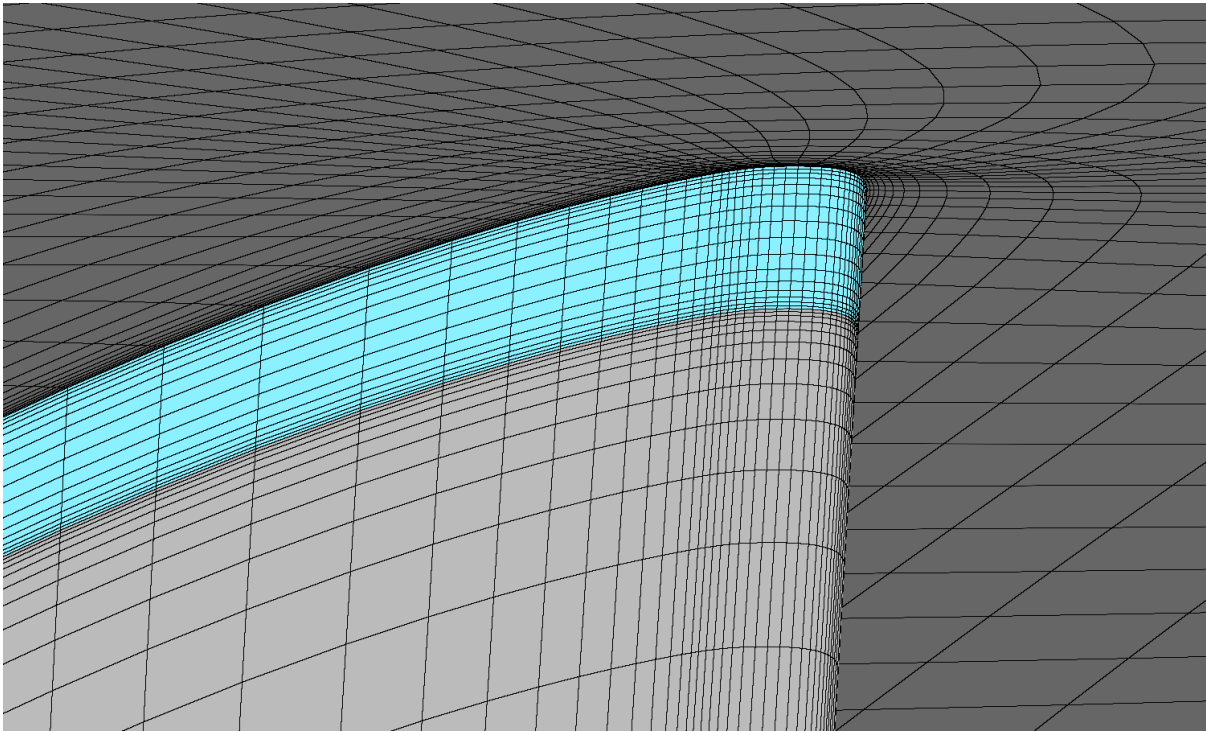

Figure 7: TIP GAP OF FIRST STAGE ROTOR.

Figure 8 shows the interface between the first stage rotor and stator. It can be seen that the mesh is non-conformal and that the patches do not fully overlap. The mixing plane rotor-stator interface is used on this interface and on the other interfaces shown in Figure 9.
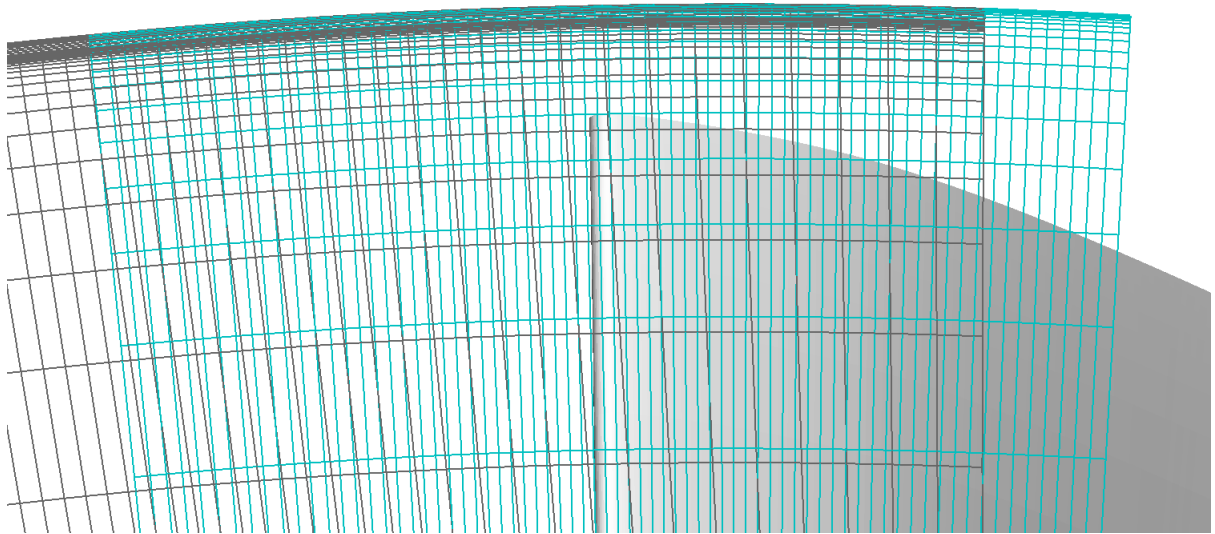
Figure 8: NUMERICAL MESH FOR THE ROTOR-STATOR INTERFACE OF THE FIRST STAGE.
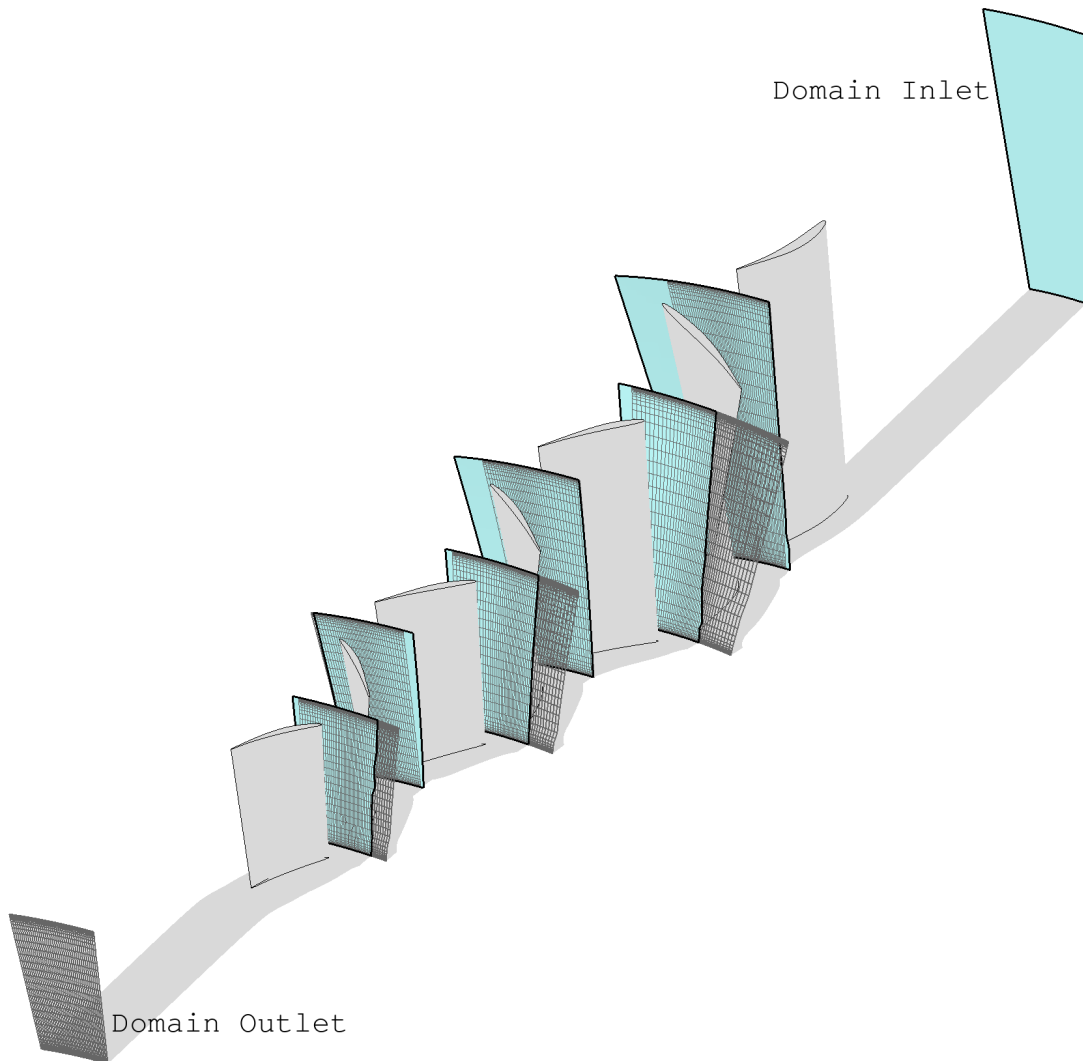

Domain Inlet

Domain Outlet

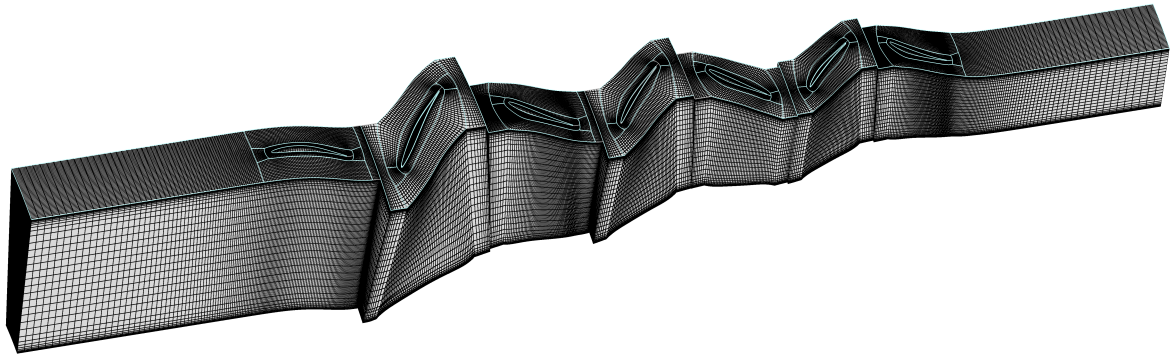**Figure 9:** INLETS (CYAN) AND OUTLETS (GREY) FOR EACH NUMERICAL MESH REGION.

Figure 10: NUMERICAL MESH FOR A SINGLE PASSAGE.

Full numerical mesh for a single passage is shown in Figure 10. The O-H mesh topology is displayed for the shroud of each blade row. The number of cells for each blade varies depending on the blade cord length and blade height. The number of cells for each region can be found in Table 5. Looking at the number cells used on a single blade of each blade row and the number of blades per blade row (Table 3) it easy to see the reduction in computational requirements with the assumption of periodic flow.

Table 5: NUMBER OF CELLS FOR NUMERICAL MESH REGIONS.

Region	Number of Cells
Inlet Guide Vanes	402432
First Stage Rotor	360448
First Stage Stator	311808
Second Stage Rotor	345088
Second Stage Stator	211968
Third Stage Rotor	345088
Third Stage Stator	423936
Overall	2400768

For the configuration shown in Figure 10, the `overlapGgi` can not be used as a rotor-stator interface. Due to different number of blades in each blade row the circumferential periodicity is not maintained. The different number of blades in each blade rows makes the relative position between blades different over the circumference of the blade row. To be able to use the `overlapGgi` at the rotor-stator interfaces the numerical mesh was modified so that the angle between the cyclic patches for each blade row was as if the blade row had 38 blades. For an axial turbo compressor with the same number of blades in each row the circumferential periodicity is maintained with a single passage. The biggest two changes in geometry occur for the third stage stator and the first stage rotor. For the IGV there is no change. The average number of blades per blade row in the IDAC is 37.29 and 37 would be a mathematically more correct choice, but with 38 blades per blade row there is less need for changing the numerical mesh. The features of Pointwise® allowed for an easy modification of the numerical mesh.

The first and second stage rotors have less than 38 blades. For these stages the cyclic patches were rotated inward towards the blade. For the rest of the blade rows rotational extrusion was used.
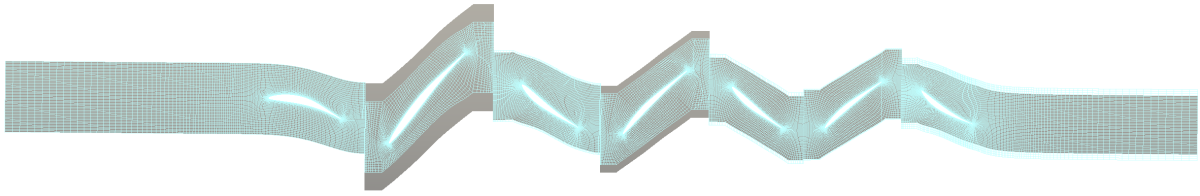

Figure 11: Difference between the original geometry (grey) and the adjusted geometry (cyan).

For the same radius, the differences between the numerical mesh with the original number of blades per blade row and the numerical mesh with 38 blades per blade row are shown in Figure 11. The blade geometry must have remained the same but the number of cells for each region has changed. The number of cells for each region in the numerical mesh modified for the `overlapGgi` rotor-stator interface is given in Table 6.

Table 6: Number of cells for numerical mesh regions.

Region	Number of Cells
Inlet Guide Vanes	402432
First Stage Rotor	328192
First Stage Stator	320640
Second Stage Rotor	340992
Second Stage Stator	217728
Third Stage Rotor	352768
Third Stage Stator	465408
Overall	2438160

3.4 Closure

This section presents the geometric characteristics of IDAC. After presenting the geometry, the method of spatial discretization of said geometry is described. The focus is put on describing the numerical mesh for a single blade since the same approach is used on all blades. After presenting a numerical mesh for a single passage of the compressor, additional numerical mesh is shown. The second mesh is for a modified compressor geometry, so a direct stator-rotor interface model can be used.

4 Results of Numerical Simulation

The mathematical model presented in Section 2 was implemented in the `steadyCompressibleMRFFoam` solver. With the `steadyCompressibleMRFFoam` solver numerical simulation were performed on two numerical meshes presented in Subsection 3.3.

4.1 Introduction

Numerical simulations where performed for the design operating point, near-stall operating points at both nominal rotor speed and 68% of the nominal rotor speed, and at near-choke operating point at 68% nominal rotor speed. Numerical results for these operating points are compared with the experimental results in terms of mass flow, total pressure ratio and adiabatic efficiency. Additional comparison is carried out with the available detailed flow data for the pressure field. Before the results are presented, boundary conditions used in the simulation are listed.

The experimental data used for the comparison with numerical results was obtained from [5], [6], [30], [8] and [27].

4.2 Boundary Conditions

The role of boundary conditions was described in Subsection 2.5. In this subsection the types of boundary conditions for each physical variable and each patch are described. The main difference in boundary conditions for different operating points is at the domain outlet (see Figure 9) for the static pressure value.

As a pressure boundary condition at the domain inlet the `isentropicTotalPressure` boundary condition was used. For the `isentropicTotalPressure` boundary condition the defined total pressure was the same for all operating points with the value of 101 325 Pa. At the domain outlet the boundary condition was set to `timeVaryingMappedFixedValue` boundary conditions. This boundary condition allows using an imposed pressure distribution at the outlet patch. The selected pressure distribution was linear with the pressure at the hub being 2% lower than the area averaged pressure at the patch and the value at the shroud being 2% higher than the area averaged pressure. For the design operating point the area averaged static pressure value is set to 178 577 Pa. This value was calculated with an iterative procedure from the available experimental data. For the near-stall point at the design rotor speed the value is set to 208 632 Pa, while for the near-stall point at 68% nominal rotor speed to 141 689 Pa. Finally, for the near-choke point at 68% nominal rotor speed the area averaged static pressure was set to 115 077 Pa. For the patches that define the compressor geometry shown in Figure 3, the `zeroGradient` boundary condition was set. The patches that define the compressor geometry are wall type boundary conditions. At the interface patches (Figure

9) the boundary condition is either `mixingPlane` or `overlapGgi`, depending on simulation type. The cyclic patches (Figure 6) are set as `cyclicGgi` for all variables, as well as `mixingPlane` and `overlapGgi` on interface patches.

For the velocity at the domain inlet, `pressureDirectedInletOutletVelocity` is set. The `pressureDirectedInletOutletVelocity` takes into account the total pressure at the inlet and calculates the velocity vector magnitude from the flux. The outlet domain boundary condition is set to `inletOutlet`. Patches depicted in Figure 3 are set to `fixedValue`.

Inlet temperature boundary condition is set to `isentropicTotalPressure`. The domain outlet and compressor geometry boundary conditions are set to `zeroGradient`.

For the turbulence properties, k and ω, respective boundary conditions are used on wall type boundaries. The domain outlet boundary condition is set to `inletOutlet`. For the turbulent kinetic energy k the inlet boundary condition is set to `turbulentIntensityKineticEnergyInlet`, while for the boundary condition on the domain inlet for the eddy turn-over time ω `turbulentMixingLengthFrequencyInlet` is applied.

Inlet domain boundary condition is set to `fixedValue` for rothalpy. The outlet domain is set `zeroGradient` as well as on the wall type boundaries. On the interface patches modified versions of `mixingPlane` and `overlapGgi` interface that account for the rothalpy jump between rotors and stators (Eq. (23)) are used.

4.3 Design Operating Point

The experimental results for the design operating point shown in Table 7 are different from the design parameters (Table 4). The difference between the design and actual mass flow rate and total pressure ratio is caused by the fact that the sidewall blockage was not considered during the two dimensional design process of the compressor [30]. The compressor was designed so that already at the design operating point a flow separation occurs at the last stage stator blade. Results presented below are obtained with the `mixingPlane` interface unless stated otherwise.

Table 7: PERFORMANCE DATA COMPARISON FOR THE DESIGN OPERATING POINT.

	Experiment	Numerical Result	Relative Error [%]
Mass Flow Rate [kg/s]	13.66	13.02	-4.66
1st Stage Total Pressure Ratio	1.31	1.32	0.71
2nd Stage Total Pressure Ratio	1.27	1.29	1.84
3rd Stage Total Pressure Ratio	1.23	1.23	0.16
Overall Total Pressure Ratio	2.06	2.09	2.71
Adiabatic Efficiency [%]	90.4	82.1	-9.15
Power [kW]	996	1068	7.19

The biggest difference between the experimental and numerical results is for the adiabatic efficiency. The difference between the total pressure ratios might indicate that the pressure

outlet boundary condition was slightly misdefined. This is probably caused by the difference in the location where the compressor experimental measurements took place and the position of the domain outlet. This causes the compressor to work in a slightly different operating condition and might explain the higher difference between the experimental and numerical results. Looking at the compressor performance map in Figure 2, lower mass flow ratio and adiabatic efficiency are consistent with a higher total pressure ratio. This would also explain why the required power input is higher in the numerical results. Of course this doesn't fully explain the difference between the two results and most of it is probably caused by the turbulence modelling and spatial domain discretization.

De Haller coefficient is a simple indicator of blade loading. It shows how much the flow is slowed down inside the blade row and is calculated by the following expression:

$$\text{de Haller} = \frac{\mathbf{u}_{\text{outlet}}}{\mathbf{u}_{\text{inlet}}} \tag{48}$$

In order to avoid flow separation de Haller coefficient should be higher than 0.7 [7]. In a stator blade row absolute velocity is used to calculate the de Haller coefficient, but for the rotor blade row relative velocity should be used. Figure 12 shows the comparison between the de Haller coefficient used during the design process and the de Haller coefficient calculated from the result of the numerical simulation.
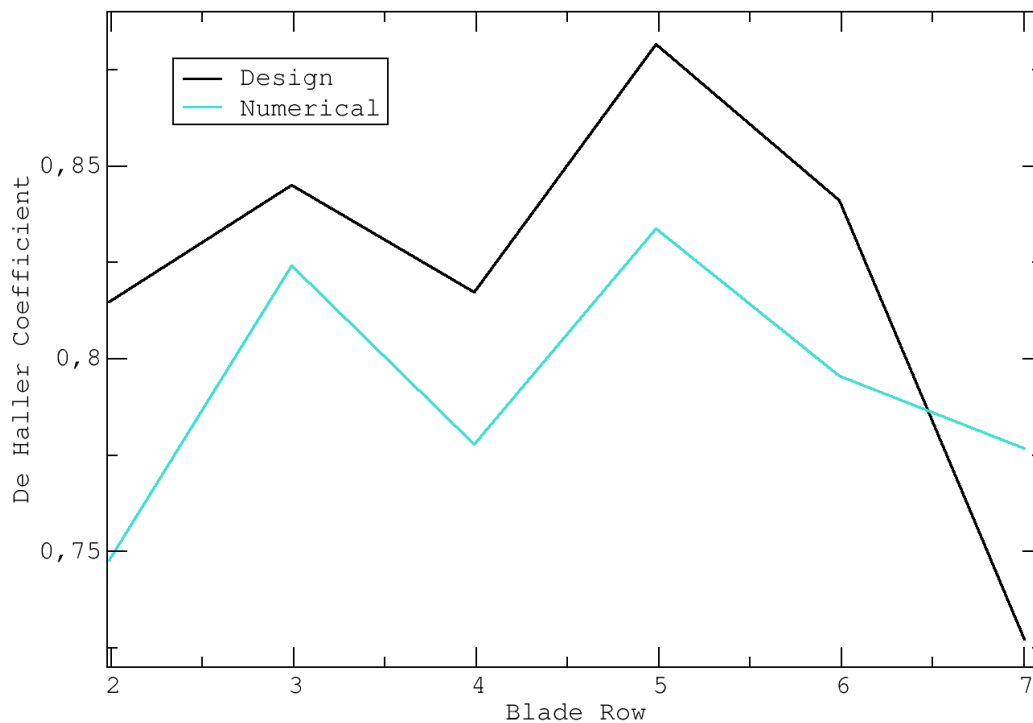

Figure 12: COMPARISON BETWEEN THE DESIGN DE HALLER COEFFICIENT AND NUMERICAL SIMULATION DE HALLER COEFFICIENT FOR THE DESIGN OPERATING POINT.

The number 2 on the horizontal axis in Figure 12 indicates the first stage rotor blade and

number 7 indicates the third stage stator blade respectively. The de Haller coefficient from the numerical results was calculated on the mid span of the blades. The numerical results follow the trend of the design curve, but indicate a higher loading than what was considered by the design process. This could have been predicted comparing the total pressure ratios for the design parameters (Table 4) and numerical results (Table 7). The main difference is on the last stage stator blade. There is no indication on which span the de Haller coefficient was taken into account during the design process. For the numerical simulation flow separation occurs below the mid span where the de Haller coefficient was calculated and that might be the cause why the de Haller coefficient is higher for the numerical result.

The pressure transducer on the compressor casing measures the pressure in multiple axial positions across the circumference above the rotor blades for each stage. The average pressure on the compressor casing was presented in [5] for all the operating points considered within this work. In order to compare numerical results to experimental on the shroud patch above a rotor blade, contours with a constant axial position were made on the same position where experimental values were measured. The values on this contours were averaged out over the circumference and presented in Figure 13. The comparison between the experimental and numerical results shows that the pressure distribution above the compressor rotor blades calculated by the numerical simulation is in good correspondence with the experimental values. The biggest difference is in the pressure distribution above the third stage rotor.
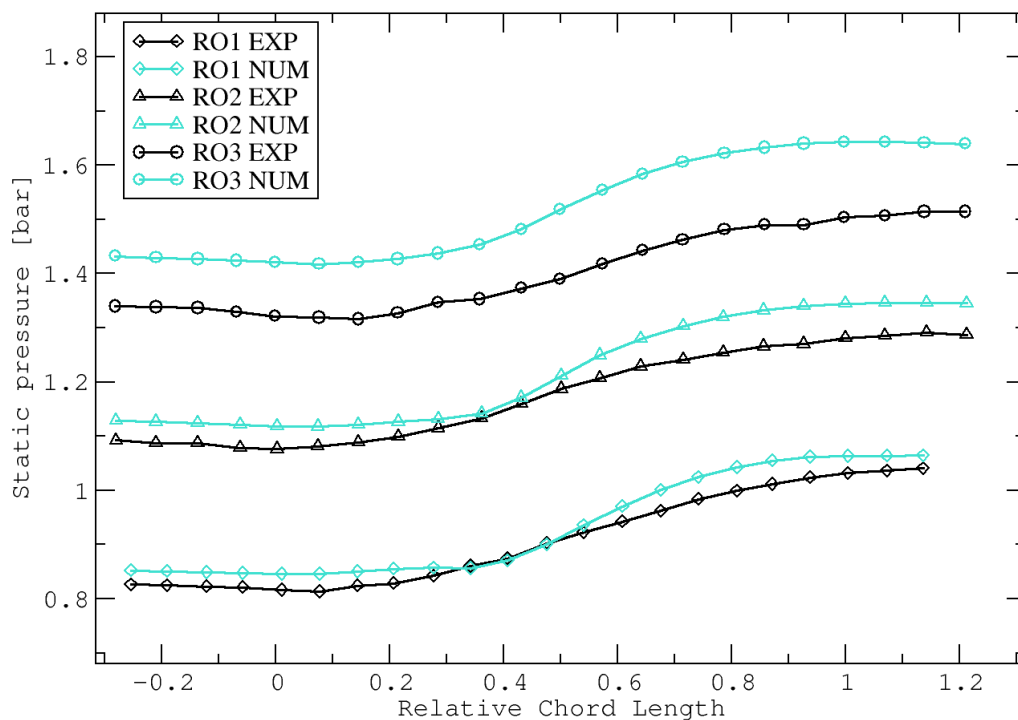

Figure 13: COMPARISON OF STATIC PRESSURE DISTRIBUTION ON THE SHROUD ABOVE ROTOR BLADES AT THE DESIGN OPERATING POINT.

(a) EXPERIMENTAL INSTANTANEOUS TOTAL PRESSURE FIELD [27].

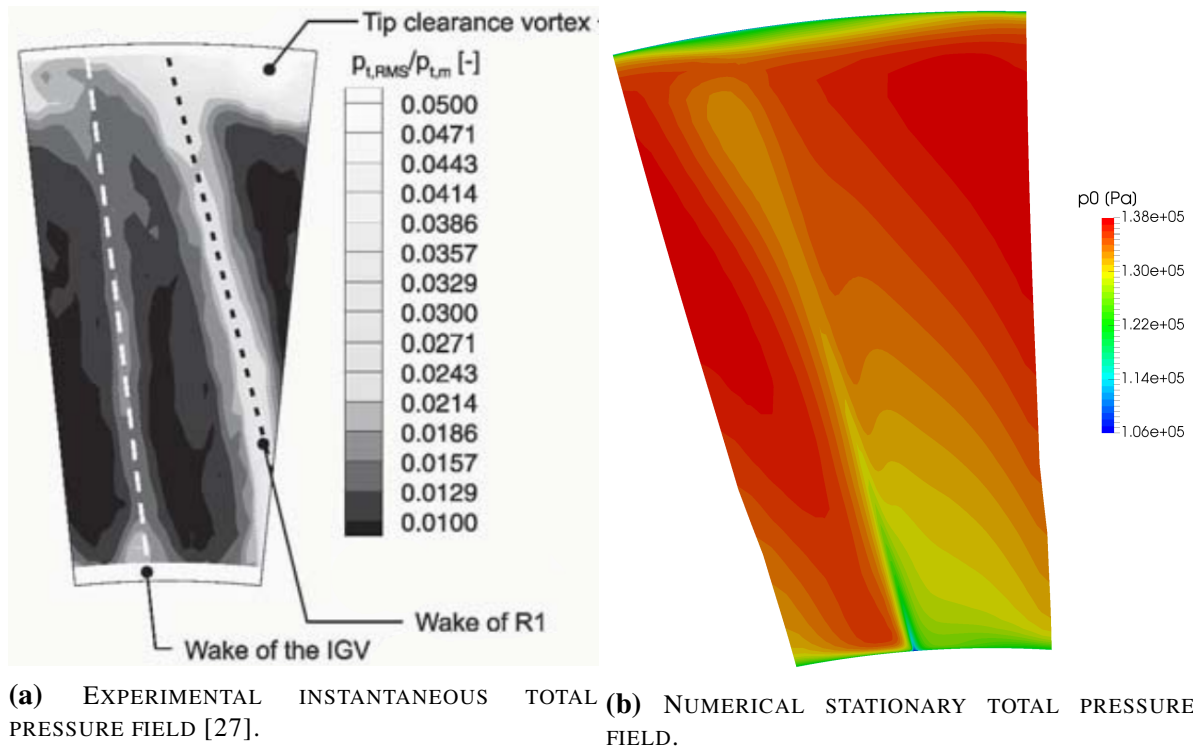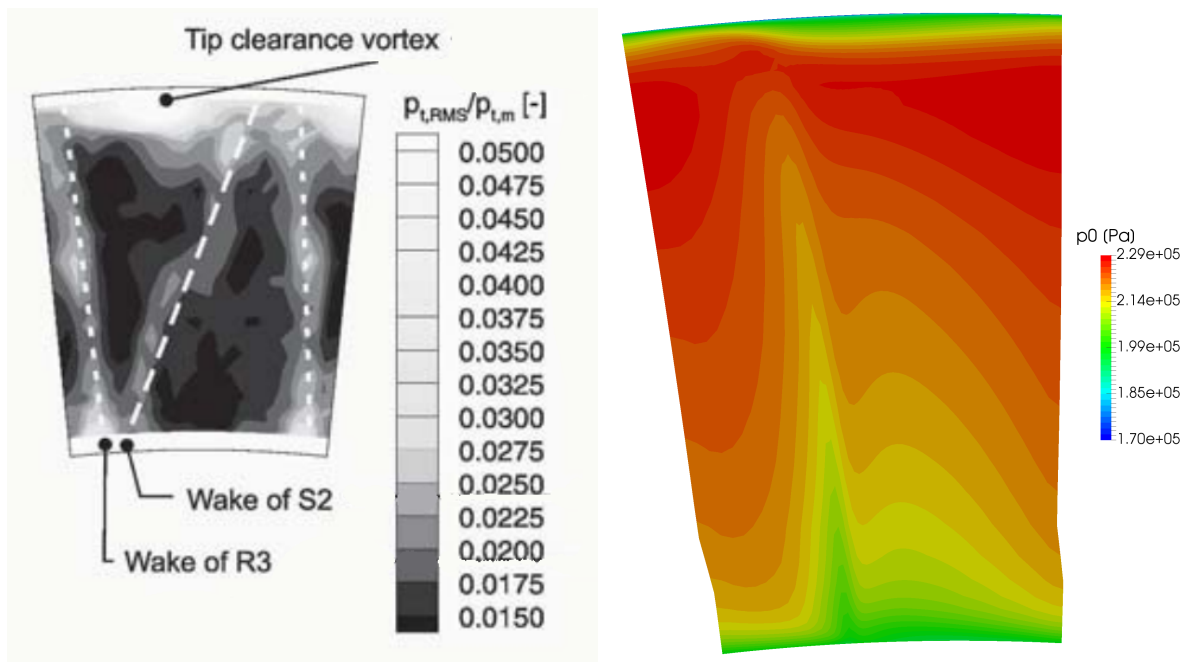**(b)** NUMERICAL STATIONARY TOTAL PRESSURE FIELD.

Figure 14: COMPARISON BETWEEN THE EXPERIMENTAL AND NUMERICAL RESULTS FOR THE TOTAL PRESSURE FIELD BEHIND THE FIRST STAGE ROTOR FOR THE DESIGN OPERATING POINT.

The experimental data presented in Figure 14a shows the instantaneous total pressure field presented in the form of root mean square values. Because of that any quantitative comparison between the numerical and experimental results is not possible as the authors did not note how the values were calculated. However, a qualitative comparison is possible. The wake of the rotor blade is present in both flow fields. The wake of the IGV could not have been captured because of the use of the mixing plane rotor-stator interface. Tip effect of tip leakage is much weaker in the steady-state numerical results than in the instantaneous experimental measurements, but still appears in the shroud region.

A similar flow field comparison is shown in Figure 15 for the total pressure field behind the last stage rotor. Again, the upstream influence seen in Figure 15 does not appear in the numerical results shown in Figure 15b because of the mixing plane rotor-stator interface. A difference between the tip gap flow between the first stage rotor (Figure 14b) and third stage rotor (Figure 15b) is noticeable. The tip gap flow over the third stage rotor blade causes a greater disturbance in the flow which results in smaller efficiency.

Both tip gap flows presented in Figure 16 have a tip gap vortex coming from the leading edge similar to what was reported in [14] for tip vortex behaviour.

(a) EXPERIMENTAL INSTANTANEOUS TOTAL PRESSURE FIELD [27].

(b) NUMERICAL STATIONARY TOTAL PRESSURE FIELD.

Figure 15: COMPARISON BETWEEN THE EXPERIMENTAL AND NUMERICAL RESULTS FOR THE TOTAL PRESSURE FIELD BEHIND THE THIRD STAGE ROTOR FOR THE DESIGN OPERATING POINT.
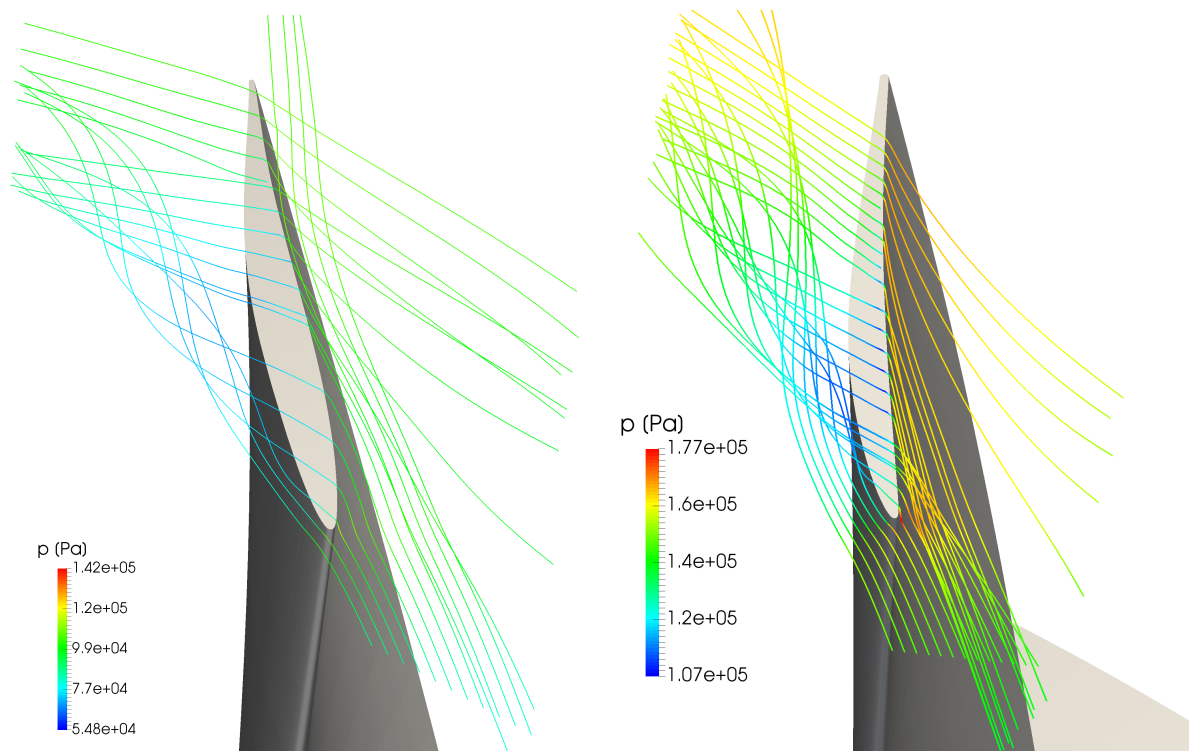
(a) TIP FLOW ABOVE FIRST STAGE ROTOR.

(b) TIP FLOW ABOVE THIRD STAGE ROTOR.

Figure 16: TIP GAP FLOW ABOVE FIRST AND LAST STAGE ROTOR BLADES.

The first stage rotor cross section (Figure 17) shows the difference in the static pressure between the pressure side and suction side. The pressure increases with the blade height due to the nature of rotational movement. Figure 18 shows a detail view of the pressure field in the tip gap as well as show the velocity vectors in the tip gap. The detailed view illustrates how the flow is accelerated through the tip gap due to the pressure difference.
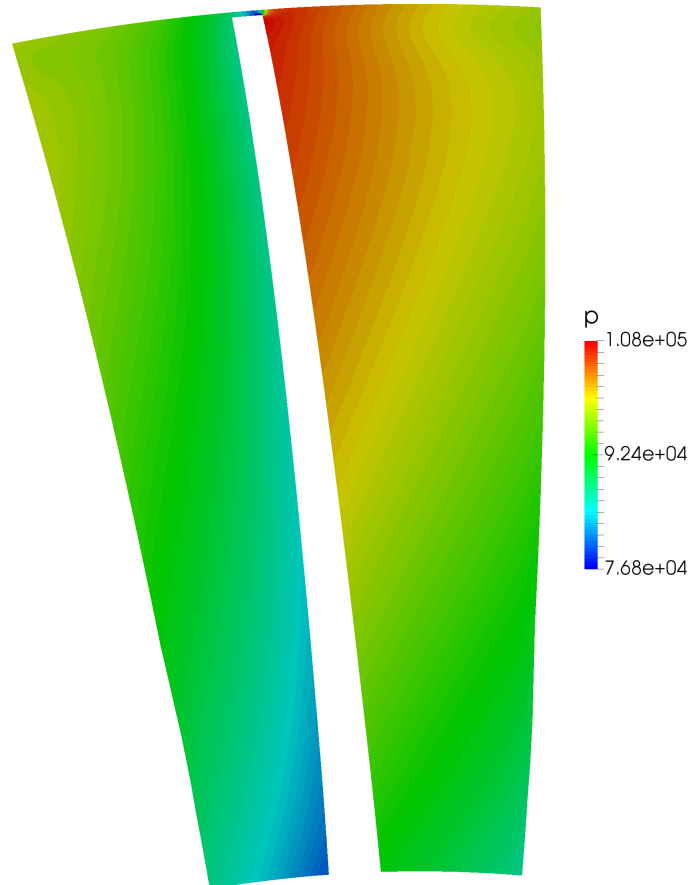

Figure 17: STATIC PRESSURE IN THE FIRST STAGE ROTOR CROSS SECTION.
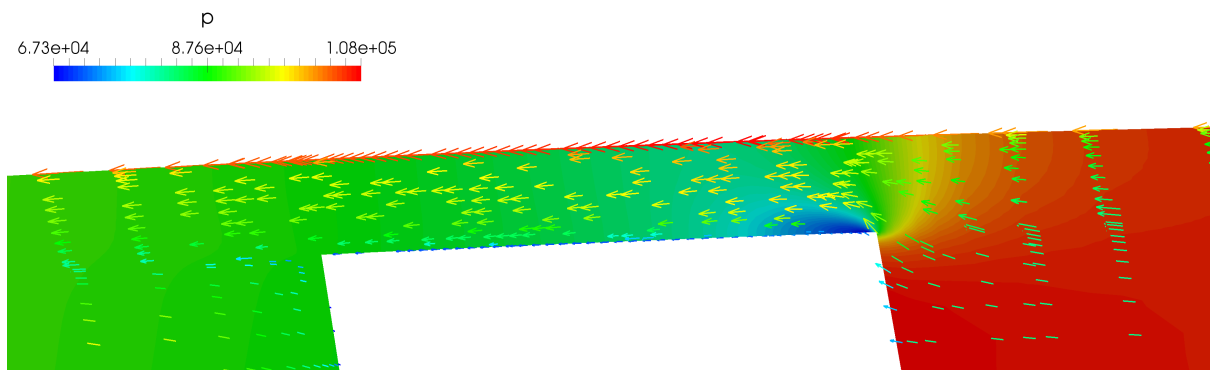
Figure 18: DETAILED VIEW OF THE TIP GAP FLOW ABOVE THE FIRST STAGE ROTOR.

The flow separation on the last stage stator blade is much more severe in the numerical results (Figure 19b) than experimental results (Figure 19a). This difference can be attributed to

turbulence modelling. In figure 20 the flow separation if visualized by streamlines. It extends through the first third of the blade height causing a loss in energy.
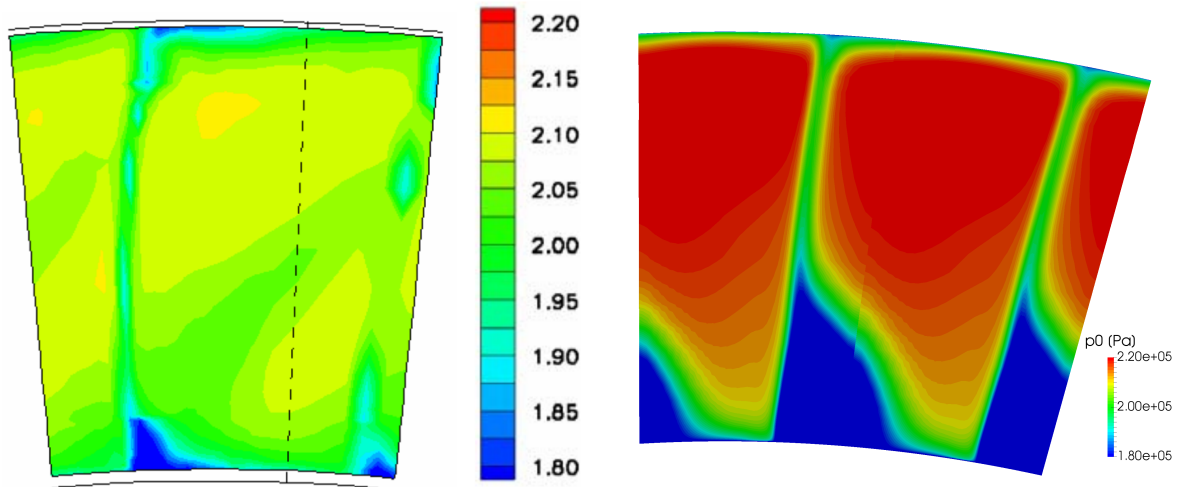
(a) EXPERIMENTAL RESULTS FOR THE TOTAL PRESSURE FIELD BEHIND LAST STAGE STATOR BLADE [8].

(b) NUMERICAL RESULTS FOR THE TOTAL PRESSURE FIELD BEHIND LAST STAGE STATOR BLADE.

Figure 19: COMPARISON OF THE RESULTS FOR THE TOTAL PRESSURE FIELD BEHIND LAST STAGE STATOR BLADE FOR THE DESIGN OPERATING POINT.
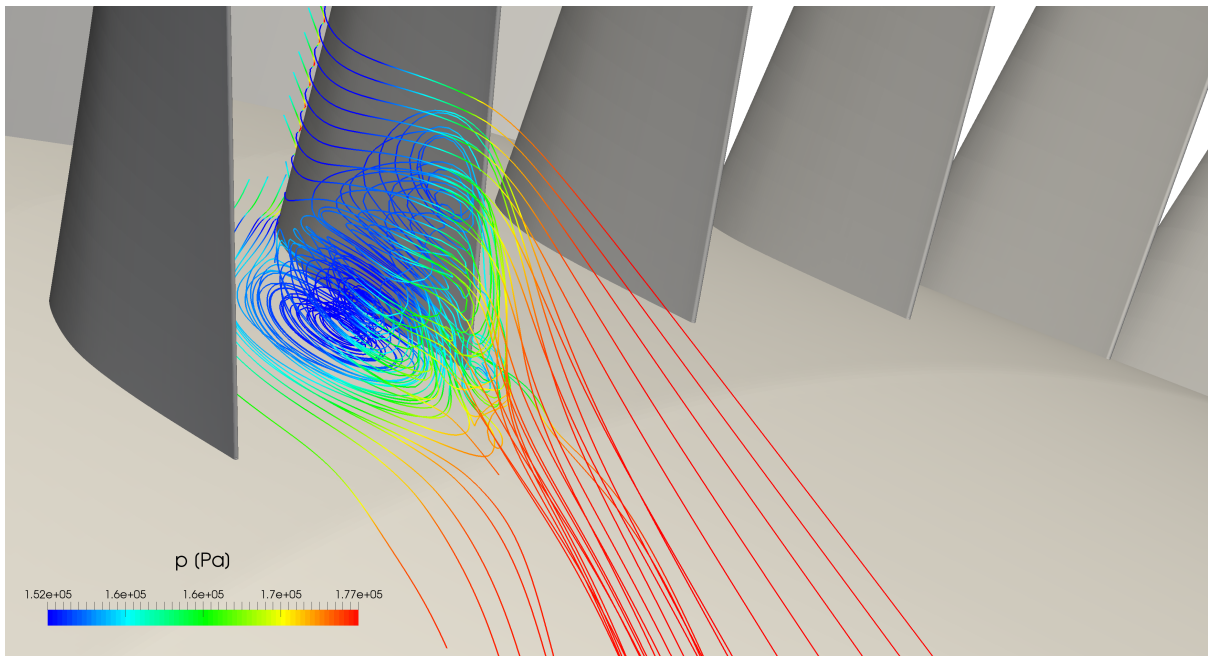

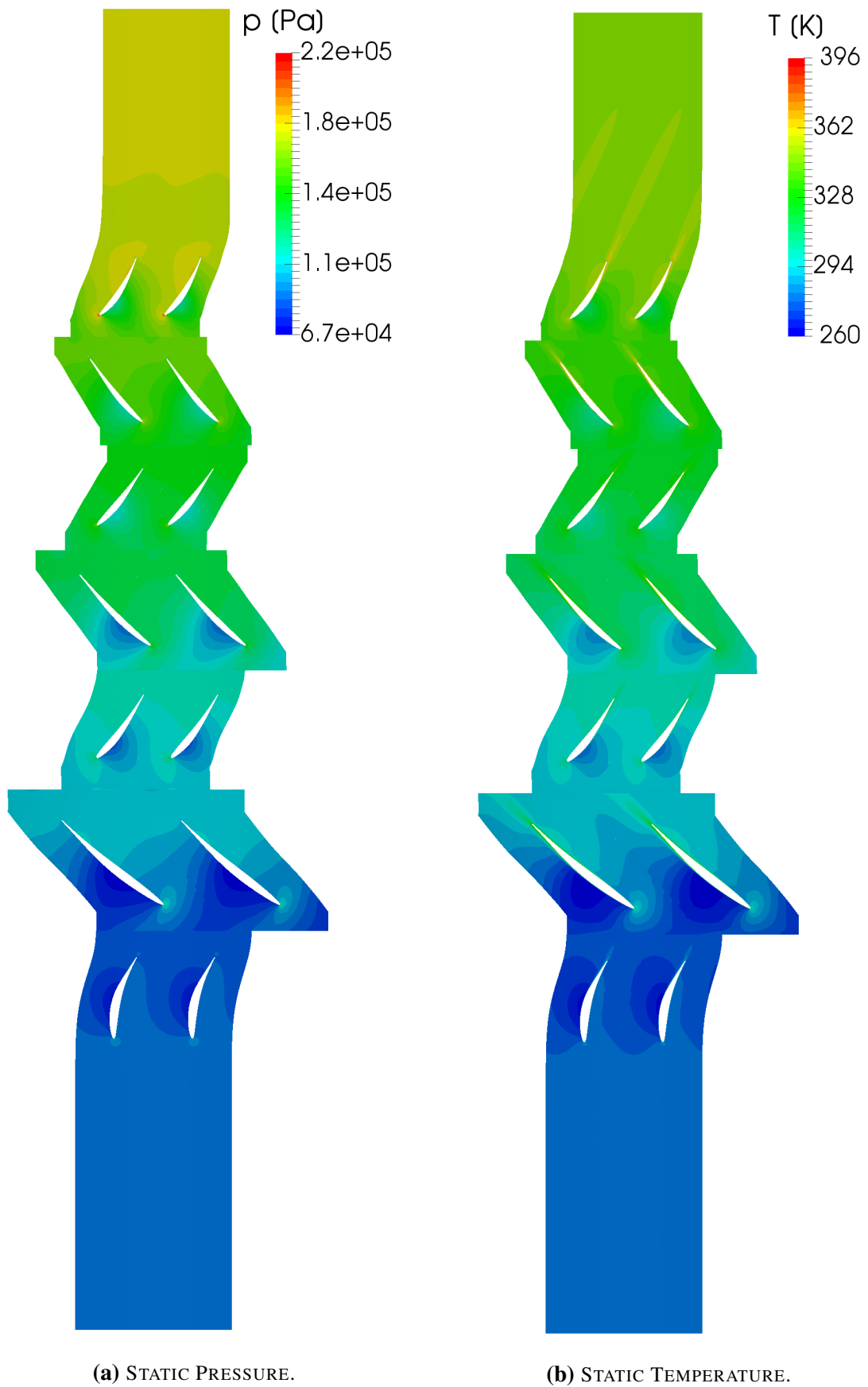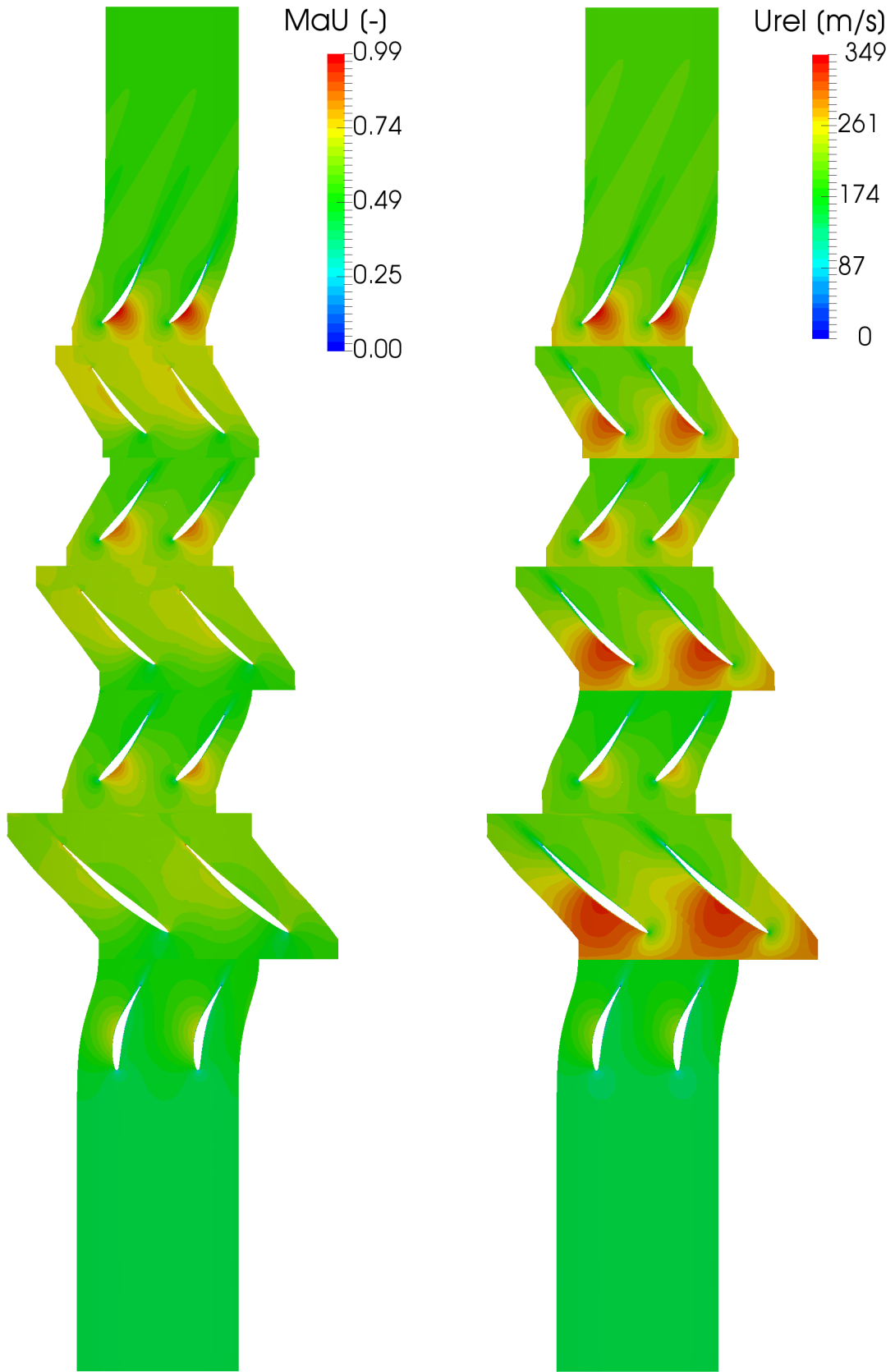**Figure 20:** FLOW SEPARATION ON THE LAST STAGE STATOR BLADE.

(a) STATIC PRESSURE.   **(b)** STATIC TEMPERATURE.

Figure 21: STATIC PRESSURE AND STATIC TEMPERATURE FIELD FOR THE DESIGN OPERATING POINT.

(a) ABOSLUTE MACH NUMBER. **(b)** RELATIVE VELOCITY MAGNITUDE.

Figure 22: ABSOLUTE MACH NUMBER AND RELATIVE VELOCITY MAGNITUDE FIELD FOR THE DESIGN OPERATING POINT.

Figures 21 and 22 show fields for different physical properties at a constant radius 84% of first stage rotor blade height. Even though a single passage was simulated, flow fields are represented for two passages to give a better sense of the flow field. From the pressure field (Figure 21a) it is easy to identify which side of the blade is the pressure side and which is the suction side. Points in which the fluid is accelerated are defined by lower pressure values and higher velocity value, and by looking at Figures 21a and 22b these points correspond to each other. In the static temperature field (Figure 21b) trailing wakes are characterized by the increase in temperature, most notably behind the first rotor and the last stage stator. In the pressure field around the first stage rotor blade shown in Figure 23 the stagnation point can be seen right at the leading edge of the blade. This means that the flow enters the blade at an optimal angle, which is to be expected since the compressor operates in the design operating point.
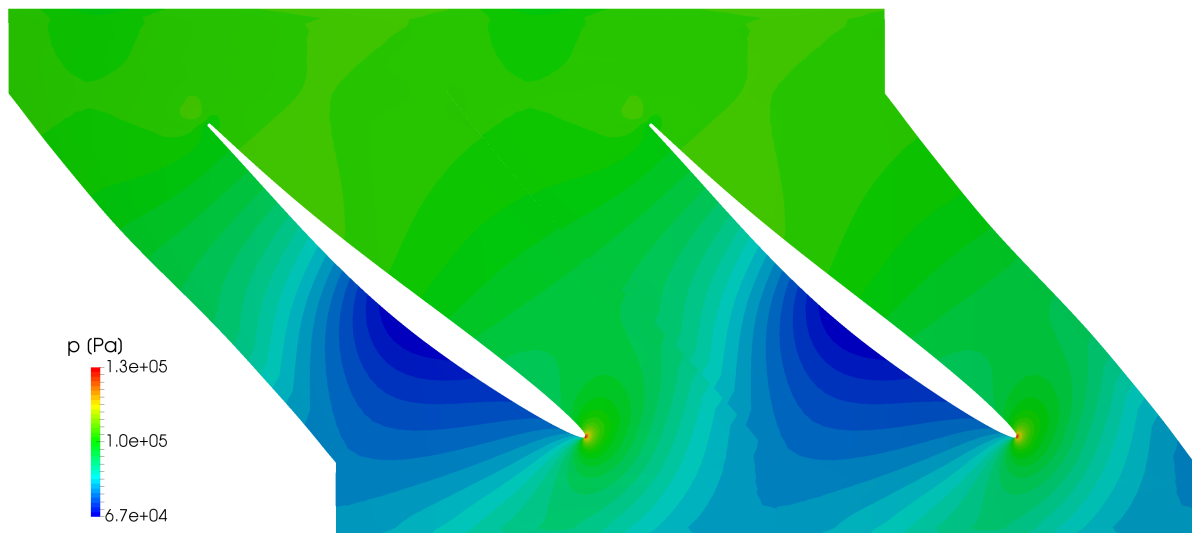

Figure 23: STATIC PRESSURE FIELD FOR FIRST ROTOR AT THE DESIGN OPERATING POINT.

Rothalpy field in Figure 24 displays the characteristics of rothalpy as discussed in Section 2. The physical property is preserved in a blade row and there is a jump in value between stators and rotors. The slight increase in rothalpy behind the second stage rotor blade is caused by dissipation which presents a source of rothalpy within the blade row.
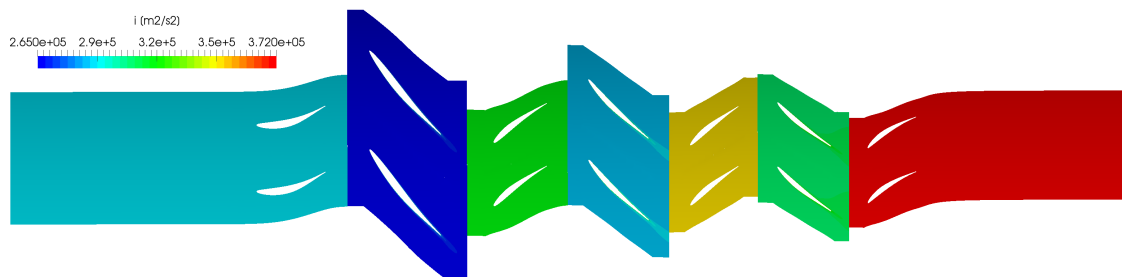

Figure 24: ROTHALPY FIELD FOR THE DESIGN OPERATING POINT.

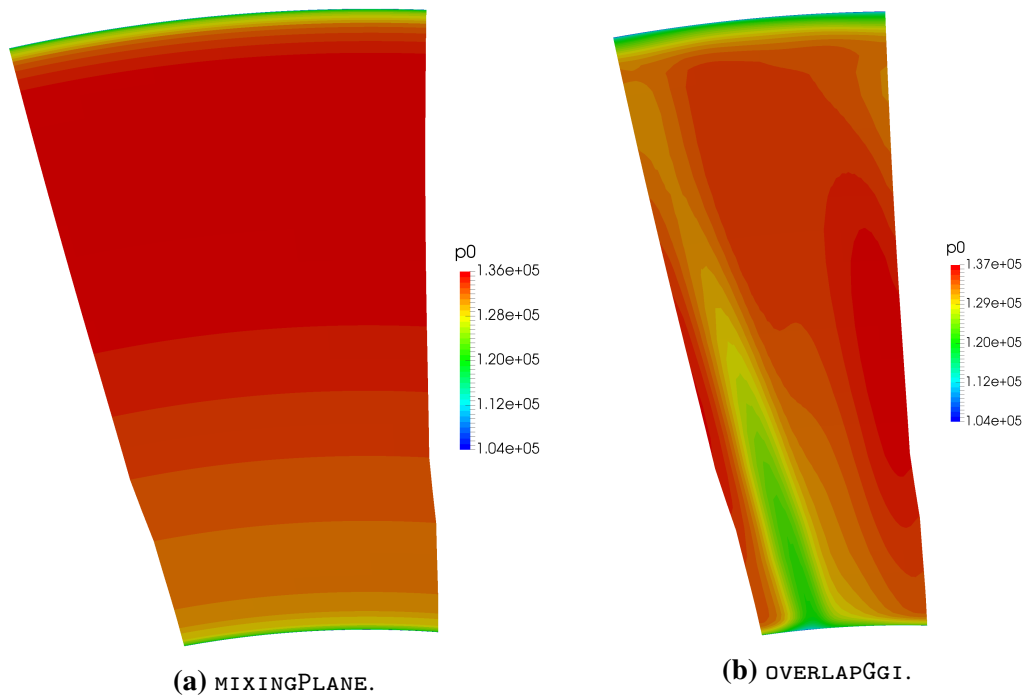**(a)** `MIXINGPLANE`.   **(b)** `OVERLAPGGI`.

Figure 25: COMPARISON OF TOTAL PRESSURE AT THE OUTLET OF THE FIRST STAGE ROTOR REGION FOR DIFFERENT ROTOR-STATOR INTERFACE METHODS.

The difference between the two rotor-stator interfaces is shown via the total pressure at the outlet of the first stage rotor region in Figure 25. The values for the `mixingPlane` method are circumferentially averaged. A small radial difference can be spotted, although there is no wake transported over the interface. With the `overlapGgi` method, the wake can be seen as there is no circumferential averaging of flow values and values are directly transferred over the interface.
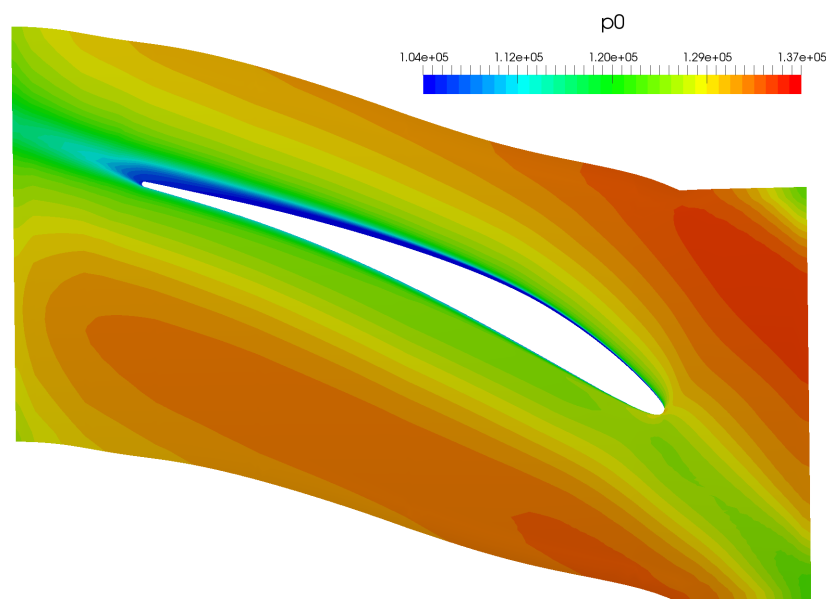

Figure 26: FIRST STAGE STATOR TOTAL PRESSURE.

Figure 26 shows how the upstream rotor wake influences the flow in the hub region of the first stage stator. The wake directly influences the flow around the stator blade.

4.4   Near-Stall Operating Point at Nominal Angular Velocity

A numerical solution for the near-stall operating point could not be obtained as defined by the experimental measurements. The outlet pressure value of 208 632 Pa defined by the experiment was gradually lowered until a numerical solution could be obtained. The outlet pressure for which a solution was obtained is 191 941 Pa. This pressure value is 7.5% higher than the outlet pressure for the design operating point which shows that the flow inside a compressor is sensitive.

The performance of the compressor in the numerically obtained stall point and the design operating point is presented in Table 8. The relationship between the two operating points is as expected. The mass flow rate decreases and the total pressure ratio increases, which corresponds with the compressor behaviour presented in Figure 2. The compressor requires more power to run at this operating point, but works less efficiently.

Table 8: PERFORMANCE DATA COMPARISON BETWEEN THE DESIGN OPERATING POINT AND NUMERICAL STALL POINT.

	Numerical Result for Design Operating Point	Numerical Result for Near-Stall Operating Point
Mass Flow Rate [kg/s]	13.024	12.51
First Stage Total Pressure Ratio	1.32	1.36
Second Stage Total Pressure Ratio	1.29	1.31
Third Stage Total Pressure Ratio	1.23	1.23
Overall Total Pressure Ratio	2.09	2.20
Adiabatic Efficiency [%]	82.13	80.01
Power [kW]	1067	1152

Figures 27 and 28 show the pressure, temperature, absolute Mach number and relative velocity magnitude fields for the near-stall operating point. The flow inside the compressor is slowed down compared to the design operating point. This is clearly seen in Figures 28a and 28b. The pressure minimum in the first rotor is higher, as the flow is not accelerated as much.

Because of a higher pressure gradient, the flow separation on the last stage stator is much more severe. During the process of obtaining the results for the experimental equivalent of near-stall operating point, the flow separation caused the flow inside the compressor to break down. The flow separation at the numerical stall point is shown in Figure 29. The flow disturbance appears at a larger radius (higher blade span) than for the design point (Figure 20).
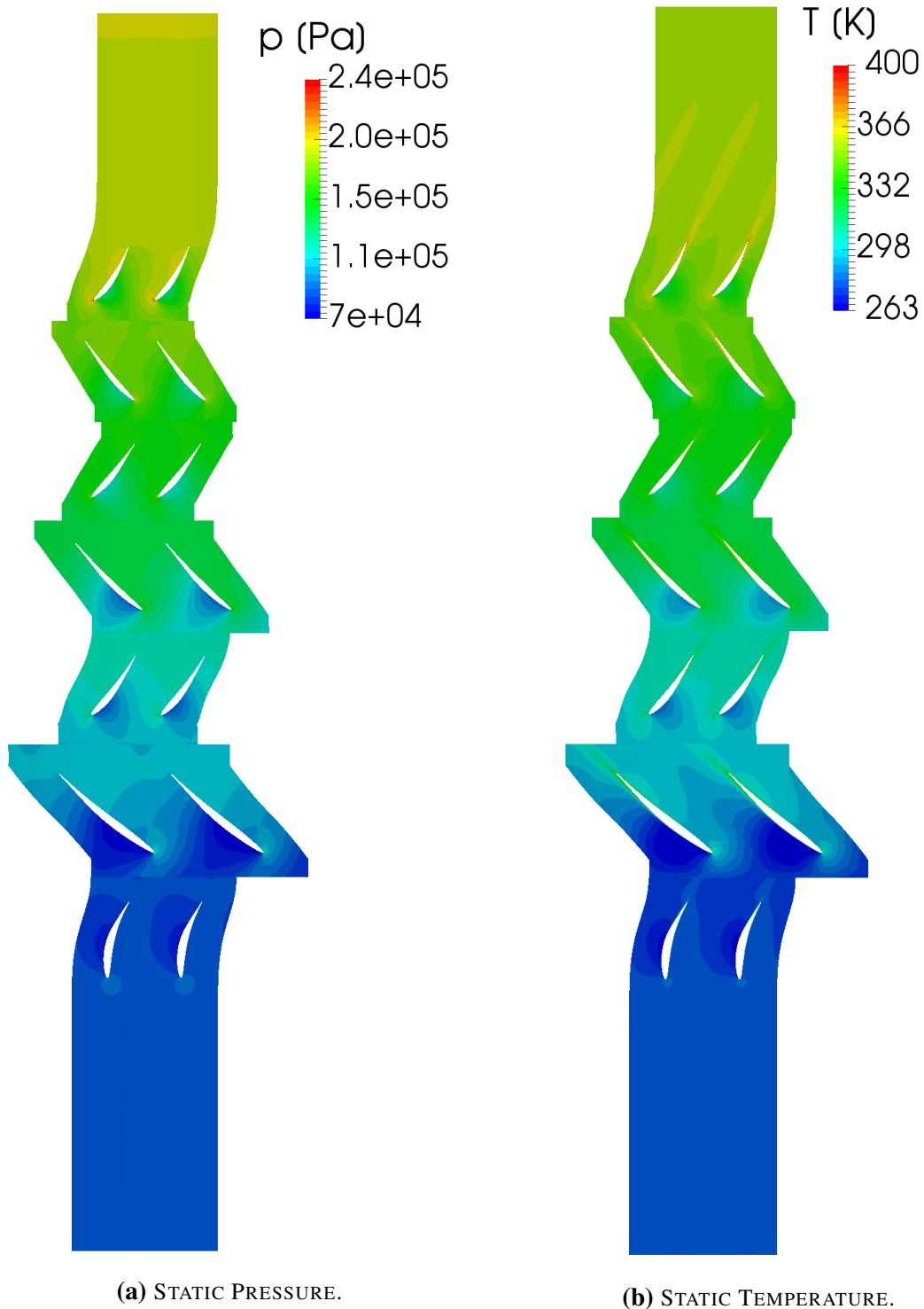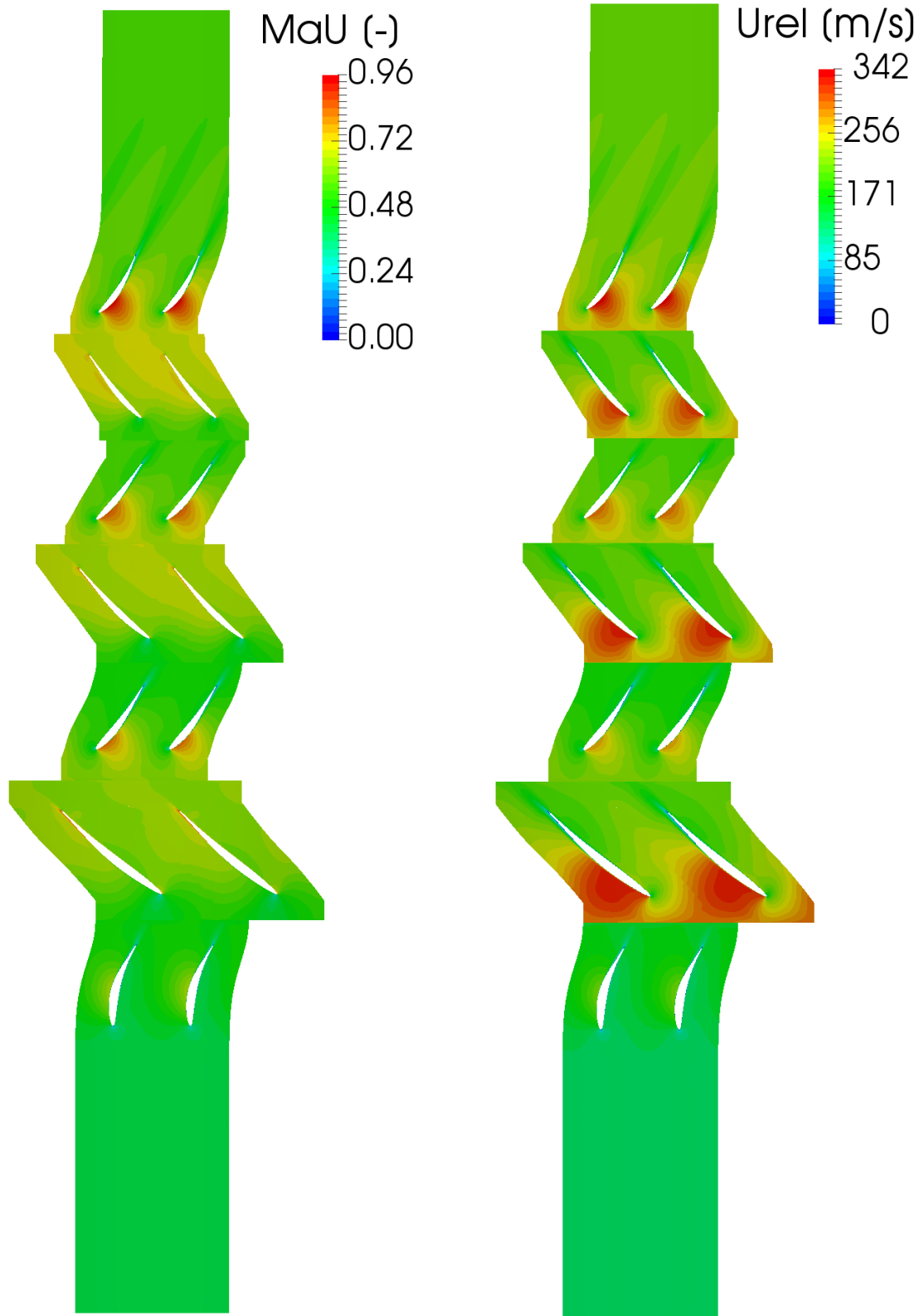
(a) STATIC PRESSURE.

(b) STATIC TEMPERATURE.

Figure 27: STATIC PRESSURE AND STATIC TEMPERATURE FIELD FOR THE NUMERICAL NEAR-STALL OPERATING POINT.

(a) ABOSLUTE MACH NUMBER.

(b) RELATIVE VELOCITY MAGNITUDE.

Figure 28: ABSOLUTE MACH NUMBER AND RELATIVE VELOCITY MAGNITUDE FIELD FOR THE NUMERICAL NEAR-STALL OPERATING POINT.
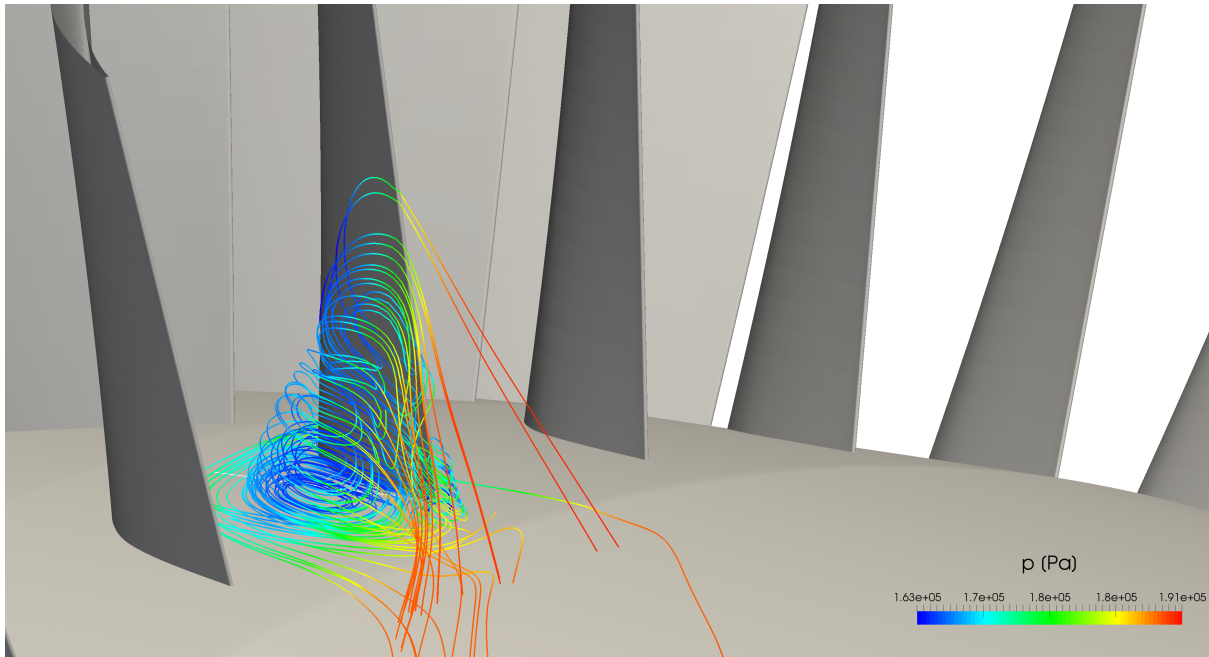
Figure 29: Flow separation on the last stage stator blade for the near-stall operating point.

4.5 Near-Stall Operating Point at 68% Nominal Angular Velocity

A number of operating points were tested experimentally, with the highest adiabatic efficiency obtained at this operating point. The IDAC performance map in Figure 2 shows the design parameters and not experimental measurements, where a much lower efficiency was calculated for this operating point. The difference is caused by the fact that the sidewall blockage was not considered during the two dimensional design process of the compressor [30].

Table 9: Performance data comparison for the near-stall operating point at 68% nominal angular velocity.

	Experiment	Numerical Result	Relative Error [%]
Mass Flow Rate [kg/s]	8.38	7.84	-6.38
1st Stage Total Pressure Ratio	1.17	1.18	-0.61
2nd Stage Total Pressure Ratio	1.15	1.15	0.16
3rd Stage Total Pressure Ratio	1.12	1.13	0.49
Overall Total Pressure Ratio	1.51	1.52	0.45
Adiabatic Efficiency [%]	92.5	86.0	-7.03
Power [kW]	336	336	0.05

The numerical results for the near-stall point at 68% nominal angular velocity (Table 9) are in better alignment compared to the numerical results for the design operating point (Table 7). The biggest difference, as with the design point numerical results, is in the adiabatic efficiency.

For the near-stall point at 68% nominal angular velocity, the de Haller coefficient calculated from experimental tests was available in [30]. The comparison between the numerical and

experimental results is similar to the comparison between the numerical results and design parameters (Figure 12). The numerical results predict a higher loading of the blades, but follow the same trend as experimental results for the first six blade rows. The outlier in the results is the last stage stator. Although no flow separation was detected at the mid span of the last stage stator, blade the numerical results show a high loading on the blade. The de Haller coefficient for the first stage rotor blade is lower than 0.7, but there is no flow separation either.
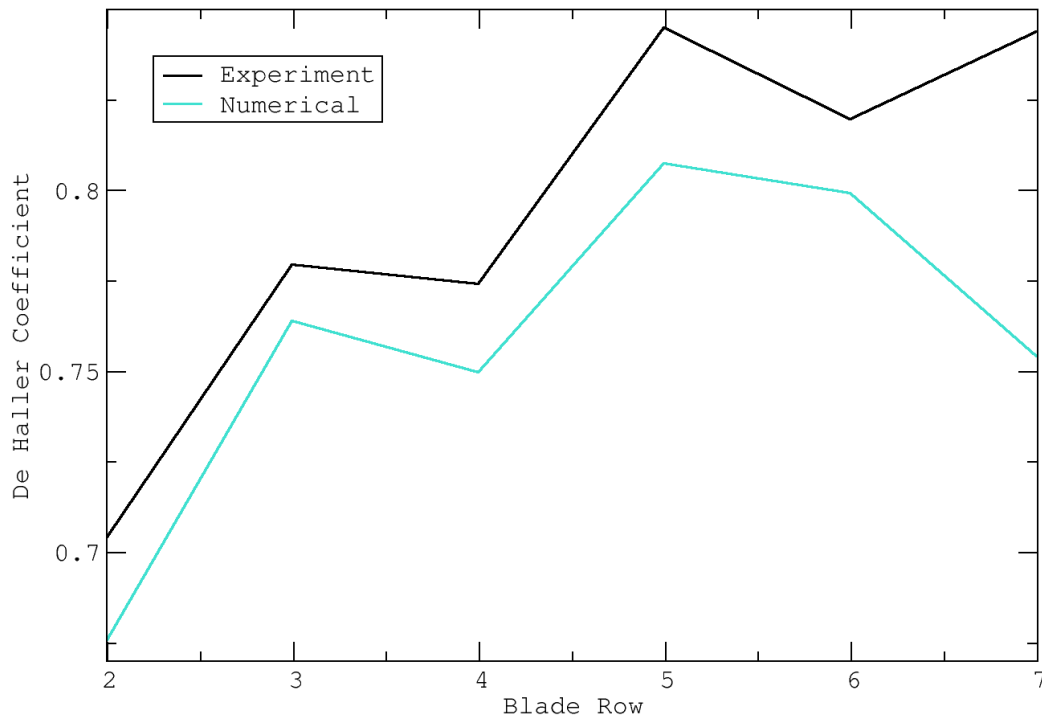

Figure 30: Comparison between the de Haller coefficient calculated from experimental measurements and numerical simulation. Near-stall operating point at 68% nominal angular velocity.

Figure 31 shows the comparison of the pressure distribution on shroud between the experiment and numerical simulation. The numerical results are in good agreement with the experimental results. The numerical solution shows a dip in average pressure values above the leading edge for both first and second stage rotors. This could be due to a tip vortex occurring on the leading edge.

The total pressure field behind the first stage rotor is presented in Figure 32. Experimental measurements (Figure 32a) indicate higher total pressure values in the shroud region. A similar flow characteristic can be observed in the numerical results (Figure 32b). Another higher total pressure region can also be spotted around the blade mid-span in both the experimental measurements and numerical results.

Figure 33 shows the total pressure field behind the last stage stator. The magnitude of numerical flow separation (Figure 33b) at the last stage stator is in good agreement with the experimental measurements (Figure 33a).
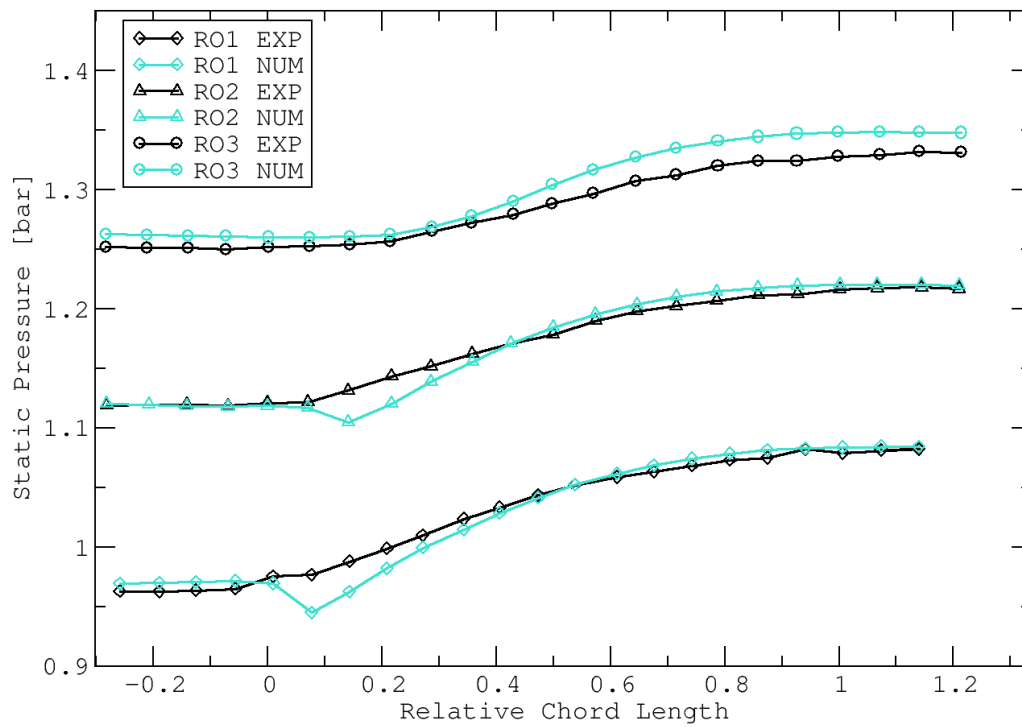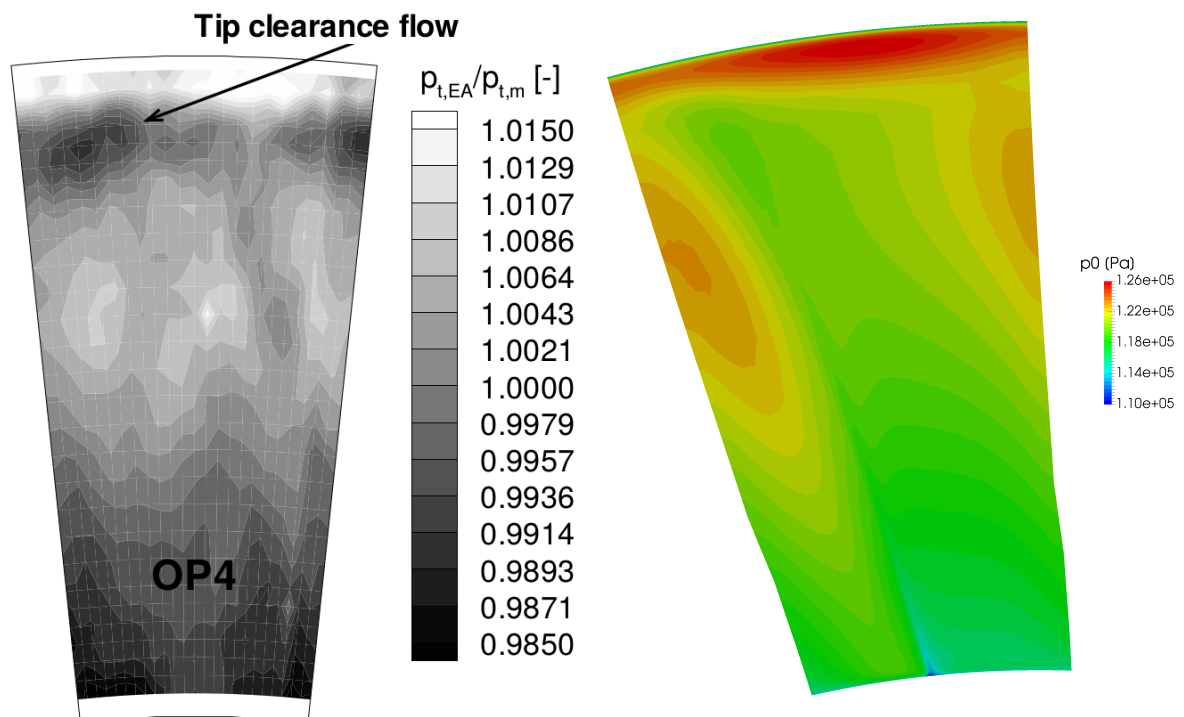
Figure 31: COMPARISON OF STATIC PRESSURE DISTRIBUTION ON THE SHROUD ABOVE ROTOR BLADES FOR THE NEAR-STALL OPERATING POINT AT 68% NOMINAL ANGULAR VELOCITY.

(a) EXPERIMENTAL INSTANTANEOUS TOTAL PRESSURE FIELD [30].

(b) NUMERICAL STATIONARY TOTAL PRESSURE FIELD.

Figure 32: COMPARISON BETWEEN THE EXPERIMENTAL MEASUREMENTS AND NUMERICAL RESULTS FOR THE TOTAL PRESSURE BEHIND THE FIRST STAGE ROTOR. NEAR-STALL OPERATING POINT AT 68% NOMINAL ANGULAR VELOCITY.
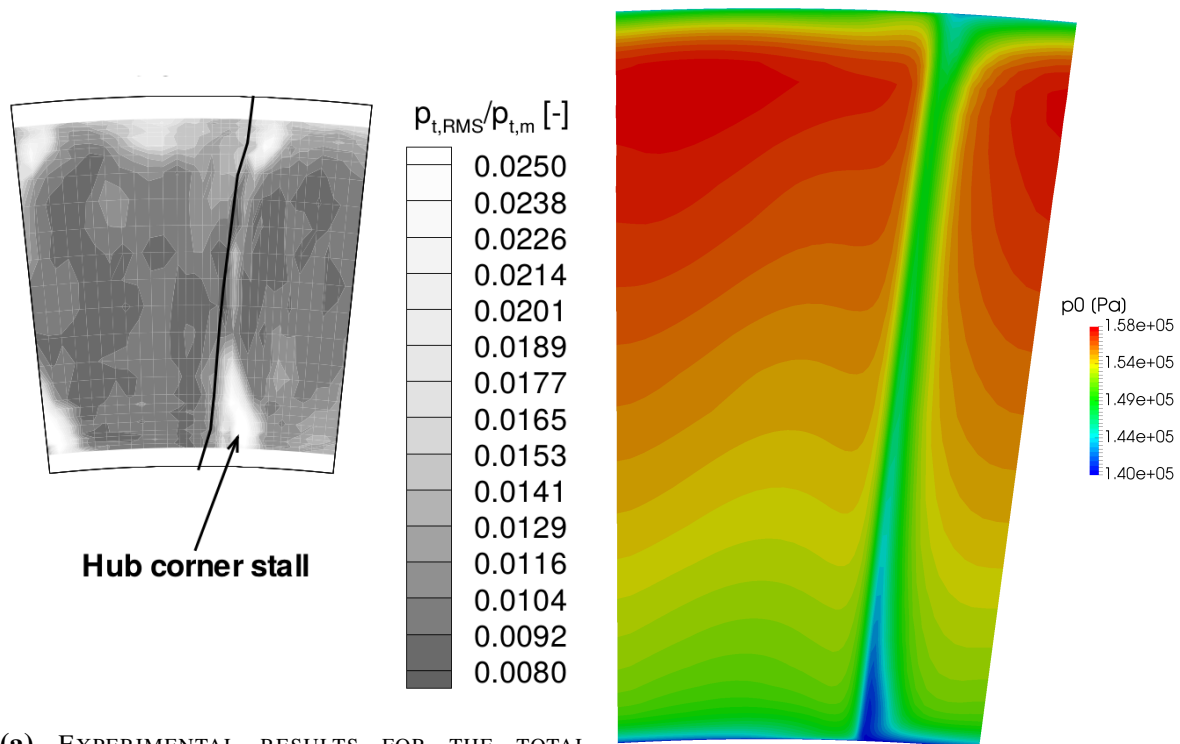
(a) EXPERIMENTAL RESULTS FOR THE TOTAL PRESSURE FIELD BEHIND LAST STAGE STATOR BLADE.

(b) NUMERICAL RESULTS FOR THE TOTAL PRESSURE FIELD BEHIND LAST STAGE STATOR BLADE.

Figure 33: COMPARISON BETWEEN THE EXPERIMENTAL MEASUREMENTS AND NUMERICAL RESULTS FOR THE TOTAL PRESSURE FIELD BEHIND THE LAST STAGE STATOR FOR THE NEAR-STALL OPERATING POINT AT 68% NOMINAL ANGULAR VELOCITY.

In Figures 27 and 28 the pressure, temperature, absolute Mach number and relative velocity magnitude fields are shown for the near-stall operating point at 68% nominal angular velocity. As the static pressure rises across the compressor so does the temperature. Since the angular velocity is lower, the maximum values for the absolute Mach number and relative velocity magnitude are also lower. The shape of the wake behind the last stator visible in Figure 34b shows how the periodic boundary condition is handled by the `cyclicGgi`.

A detailed view of the pressure field is shown in Figure 36 which shows the pressure field around the first stage rotor blade. The stagnation point for this operating point is in a different location than for the design operating point (Figure 23). The ideal position of the stagnation point is at the leading edge but for this operating point the stagnation point moved to the pressure side of the blade. The change stagnation points position shows that the fluid does not enter the blade at an optimal angle. A better view of the flow direction is shown in Figure 37. Figure 37 shows the velocity vector near the leading edge as well as the pressure field. The pressure minimum in Figure 37 shows the location where the fluid is accelerated around the leading edge to the suction side.
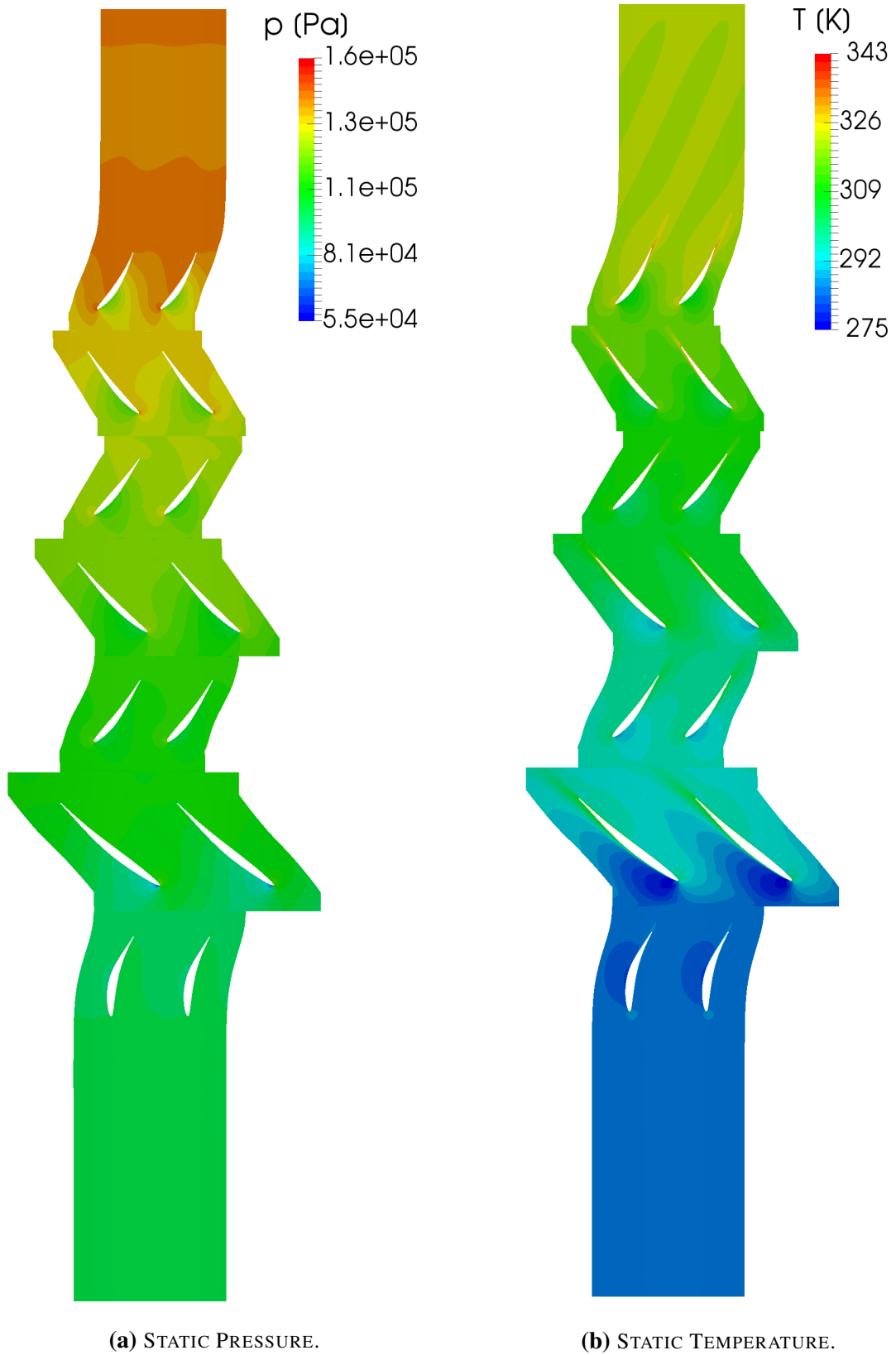
(a) STATIC PRESSURE.

(b) STATIC TEMPERATURE.

Figure 34: STATIC PRESSURE AND STATIC TEMPERATURE FIELD FOR THE NEAR-STALL OPERATING POINT AT 68% ANGULAR VELOCITY.

(a) Aboslute Mach Number.

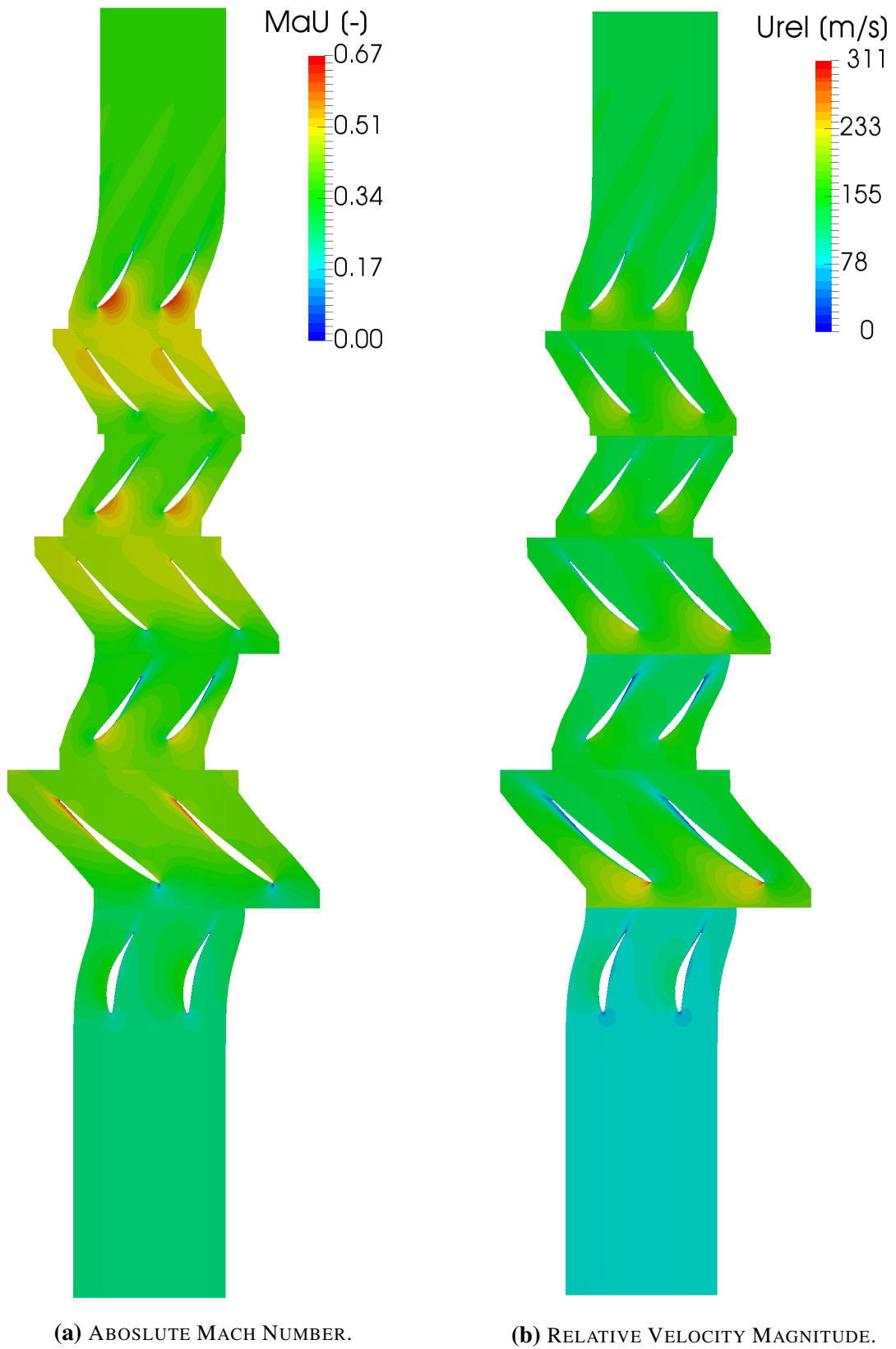**(b)** Relative Velocity Magnitude.

Figure 35: Absolute Mach number and relative velocity magnitude for the near-stall operating point at 68% angular velocity.
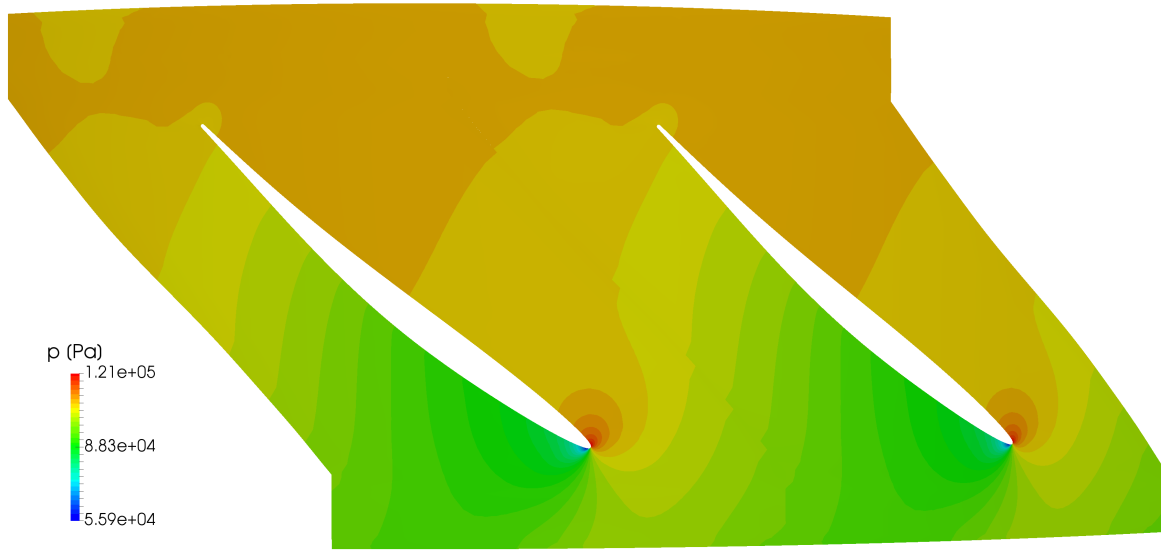
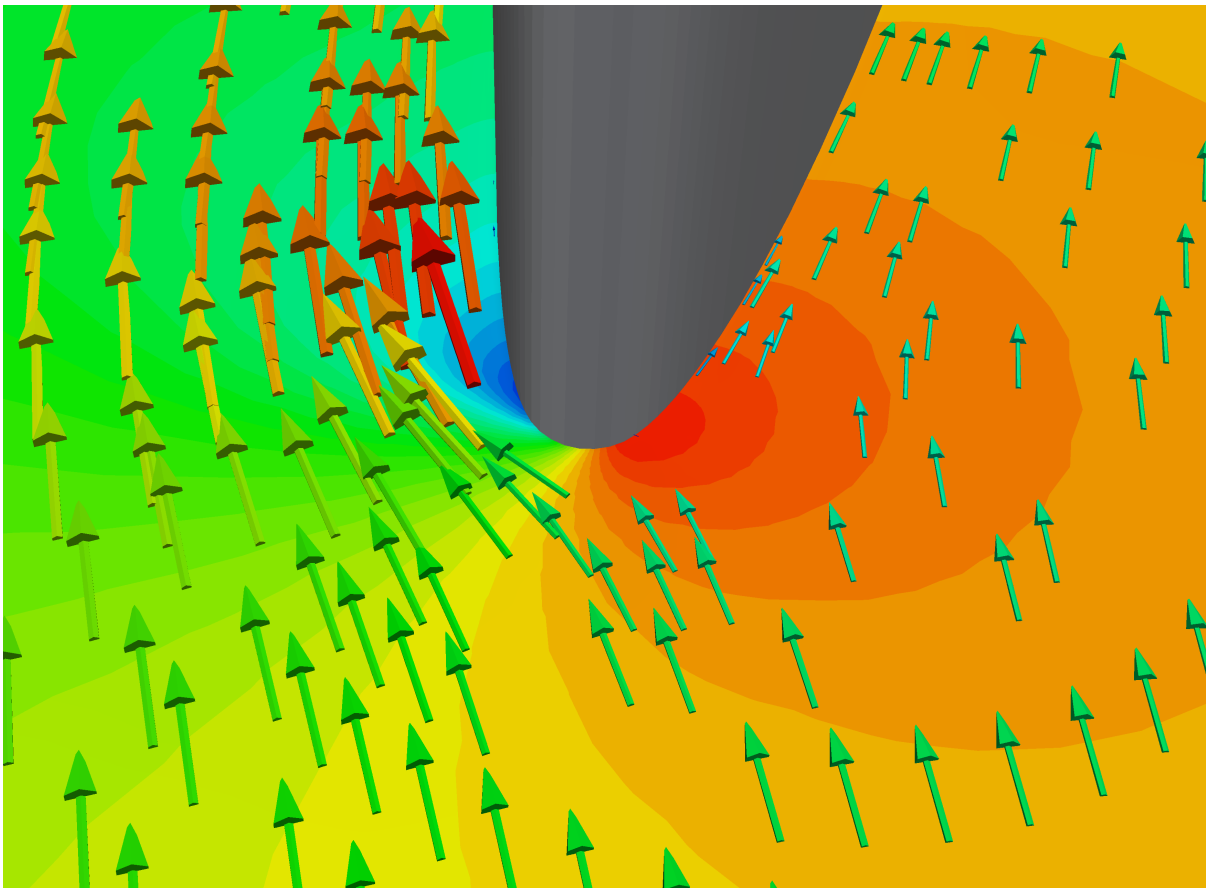**Figure 36:** STATIC PRESSURE FIELD FOR FIRST ROTOR FOR THE NEAR-STALL OPERATING POINT AT 68% ANGULAR VELOCITY.

Figure 37: VELOCIY VECTORS AT THE FIRST ROTOR LEADING EDGE FOR THE NEAR-STALL OPERATING POINT AT 68% ANGULAR VELOCITY.

4.6   Near-Choke Operating Point at 68% Nominal Angular Velocity

The experimental data for this operating point shows that the last stage rotor is almost unloaded. Table 10 shows the comparison in the performance data between the experiment and numerical simulation. As with the previously presented operating points, the biggest difference between the two results is in adiabatic efficiency.

Table 10: PERFORMANCE DATA COMPARISON FOR THE NEAR-CHOKE OPERATING POINT AT 68% NOMINAL ANGULAR VELOCITY.

	Experiment	Numerical Result	Relative Error [%]
Mass Flow Rate [kg/s]	9.49	8.97	-5.51
1st Stage Total Pressure Ratio	1.15	1.15	-0.10
2nd Stage Total Pressure Ratio	1.10	1.11	0.72
3rd Stage Total Pressure Ratio	1.04	1.04	0.01
Overall Total Pressure Ratio	1.31	1.32	0.73
Adiabatic Efficiency [%]	89.2	79.5	-10.84
Power [kW]	258	264	2.21

The experimental and numerical de Haller coefficient are shown in Figure 38. The numerical results follow the trend of experimental measurements across all investigated blade rows. In comparison to other numerical simulations, the simulation for the near-choke operating point at 68% nominal angular velocity shows better correlation with experimental results for the last stage stator blade.
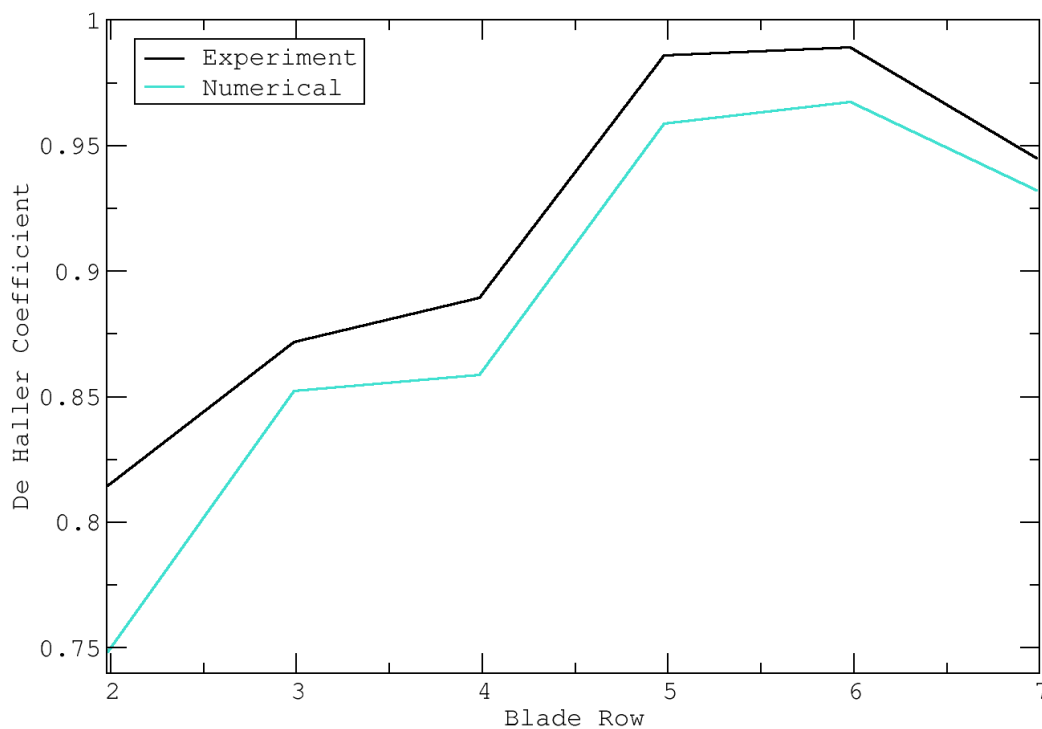

Figure 38: COMPARISON FOR THE DE HALLER COEFFICIENT BETWEEN EXPERIMENTAL AND NUMERICAL VALUES. NEAR-CHOKE OPERATING POINT AT 68% NOMINAL ANGULAR VELOCITY.
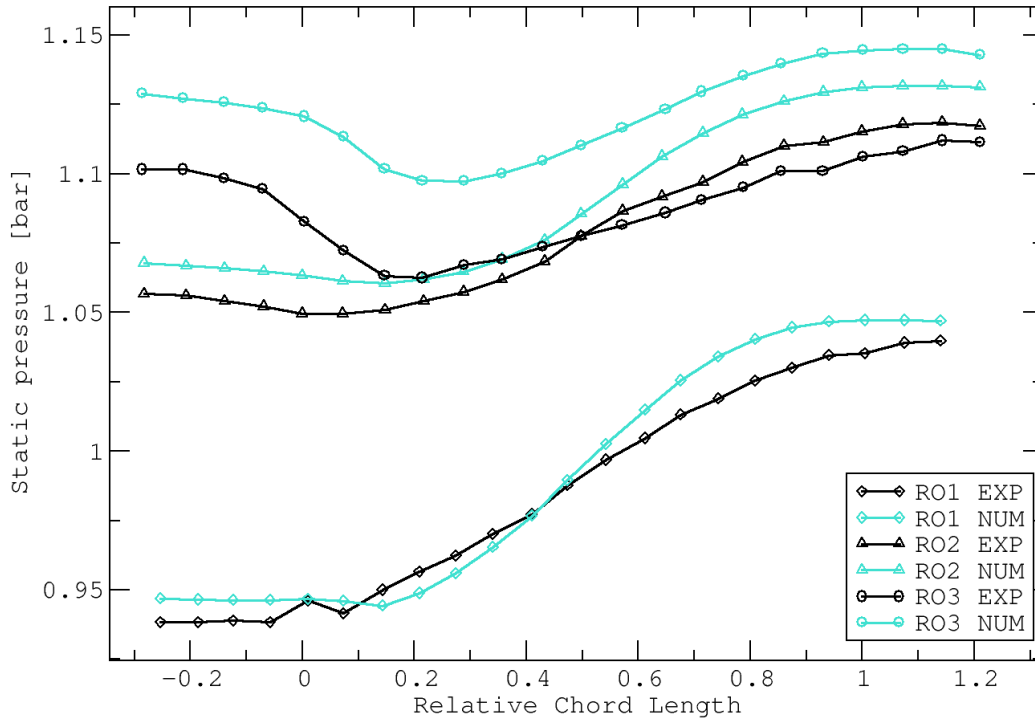
Figure 39: COMPARISON OF STATIC PRESSURE DISTRIBUTION ON THE SHROUD ABOVE ROTOR BLADES FOR THE NEAR-CHOKE OPERATING POINT AT 68% NOMINAL ANGULAR VELOCITY.
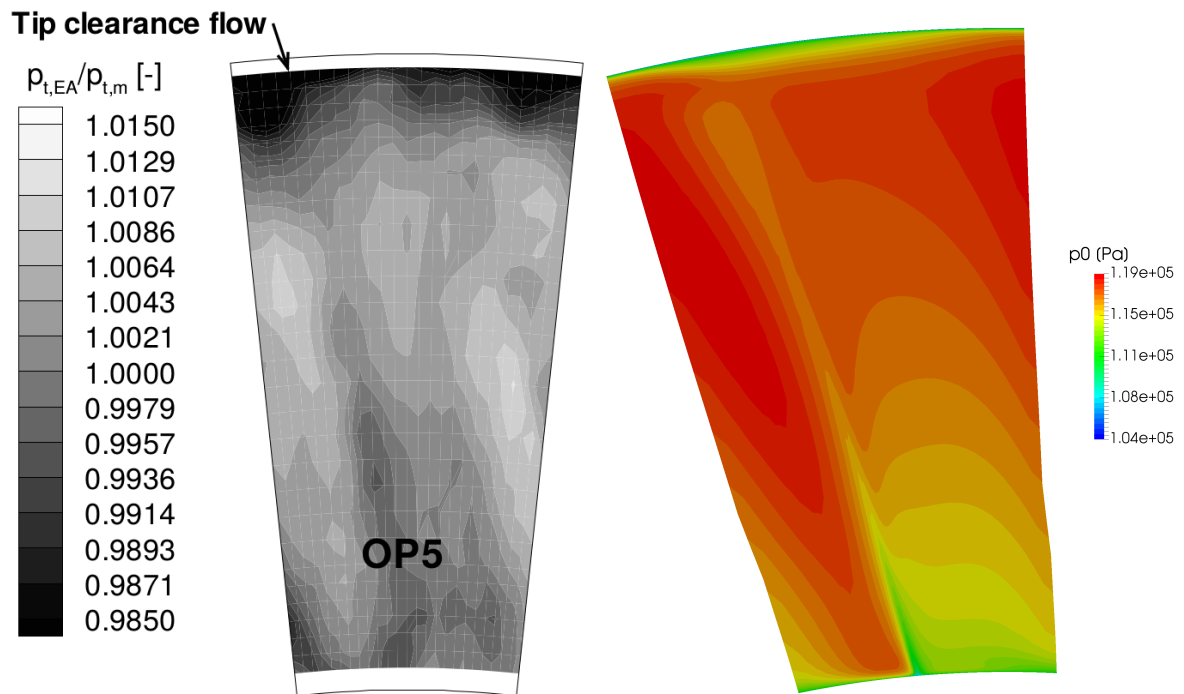
(a) EXPERIMENTAL INSTANTANEOUS TOTAL PRESSURE [30].

(b) NUMERICAL STATIONARY TOTAL PRESSURE.

Figure 40: COMPARISON BETWEEN THE EXPERIMENTAL MEASUREMENTS AND NUMERICAL RESULTS FOR THE TOTAL PRESSURE BEHIND THE FIRST STAGE ROTOR. NEAR-CHOKE OPERATING POINT AT 68% NOMINAL ANGULAR VELOCITY.

Comparison between the pressure distribution at the shroud between the experiment and numerical simulation is shown in Figure 39. The biggest difference is for the compressors third stage. The numerical result follows the trend of the experimental curve but the calculated pressure distribution has higher values. The higher pressure on shroud calculated by the numerical simulation is in correlation with the higher loading on the blades predicted by the de Haller coefficient (Figure 38).

The total pressure field behind the first stage rotor blade is shown in Figure 41. Both experimentally measured and numerically calculated fields show a wake of the first stage rotor blade. The wake is much weaker than the wake behind the first stage rotor for the design operating point (Figure 14). The tip flow is captured by the numerical simulation, as well as a lower total pressure region in the hub region.

Figure 41 displays the total pressure field behind the last stage stator. The experimental investigation of the flow behind the last stator shows a separation of the flow on the blades pressure side. This separation is not present in the numerical solution, but a decrease in total pressure can be seen in the same region where the flow separation occurs.
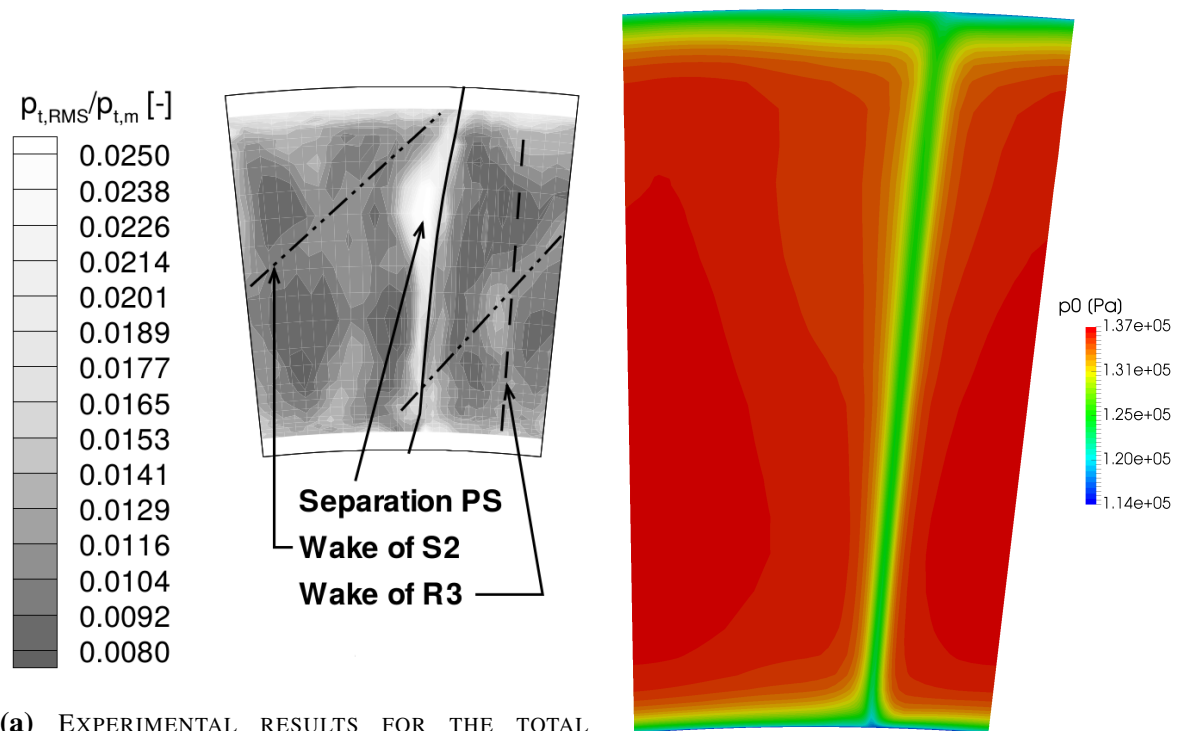
(a) Experimental results for the total pressure behind last stage stator blade.

(b) Numerical results for the total pressure behind last stage stator blade.

Figure 41: Comparison between the experimental measurements and numerical results for the total pressure behind the last stage stator. Near-choke operating point at 68% nominal angular velocity.

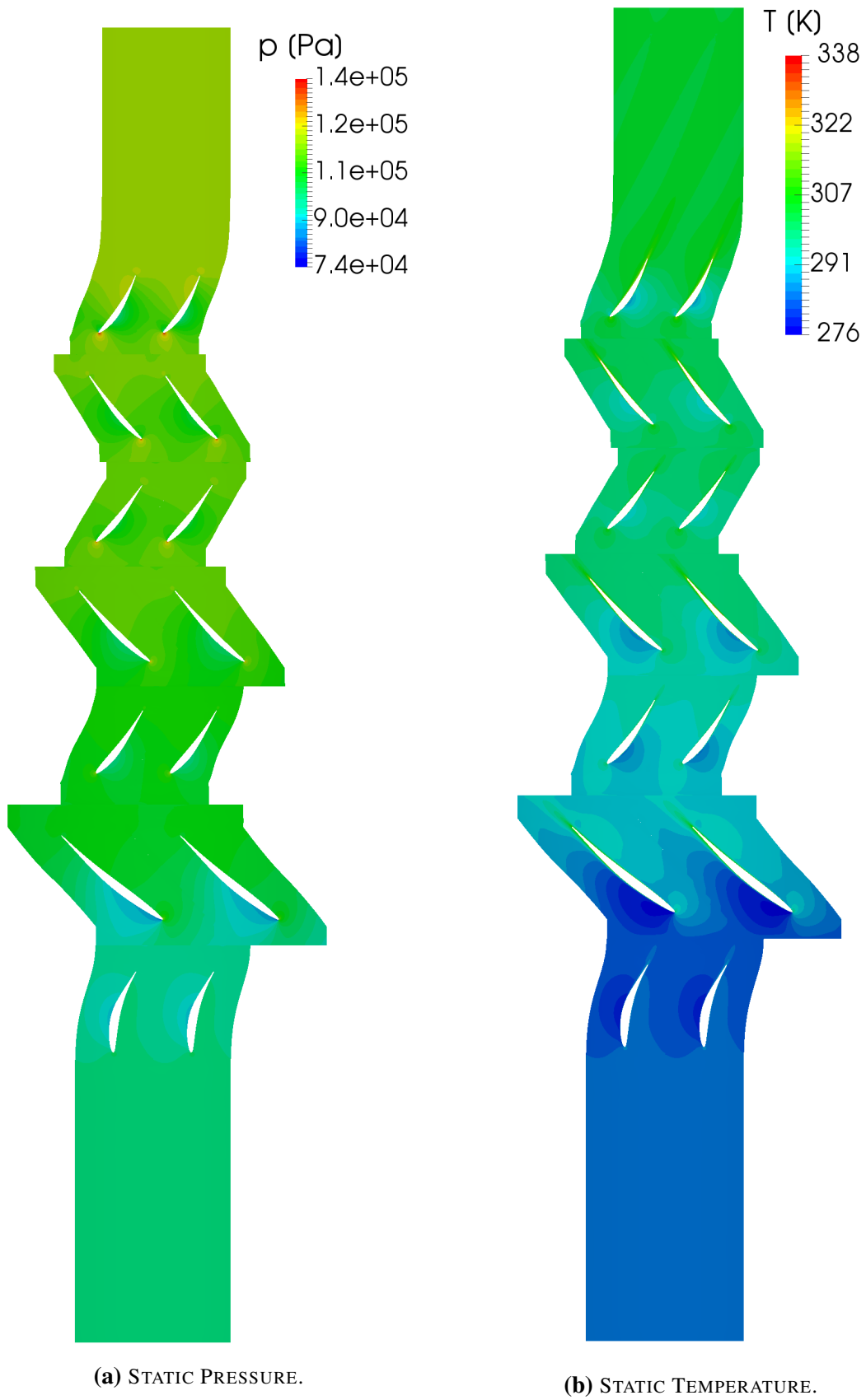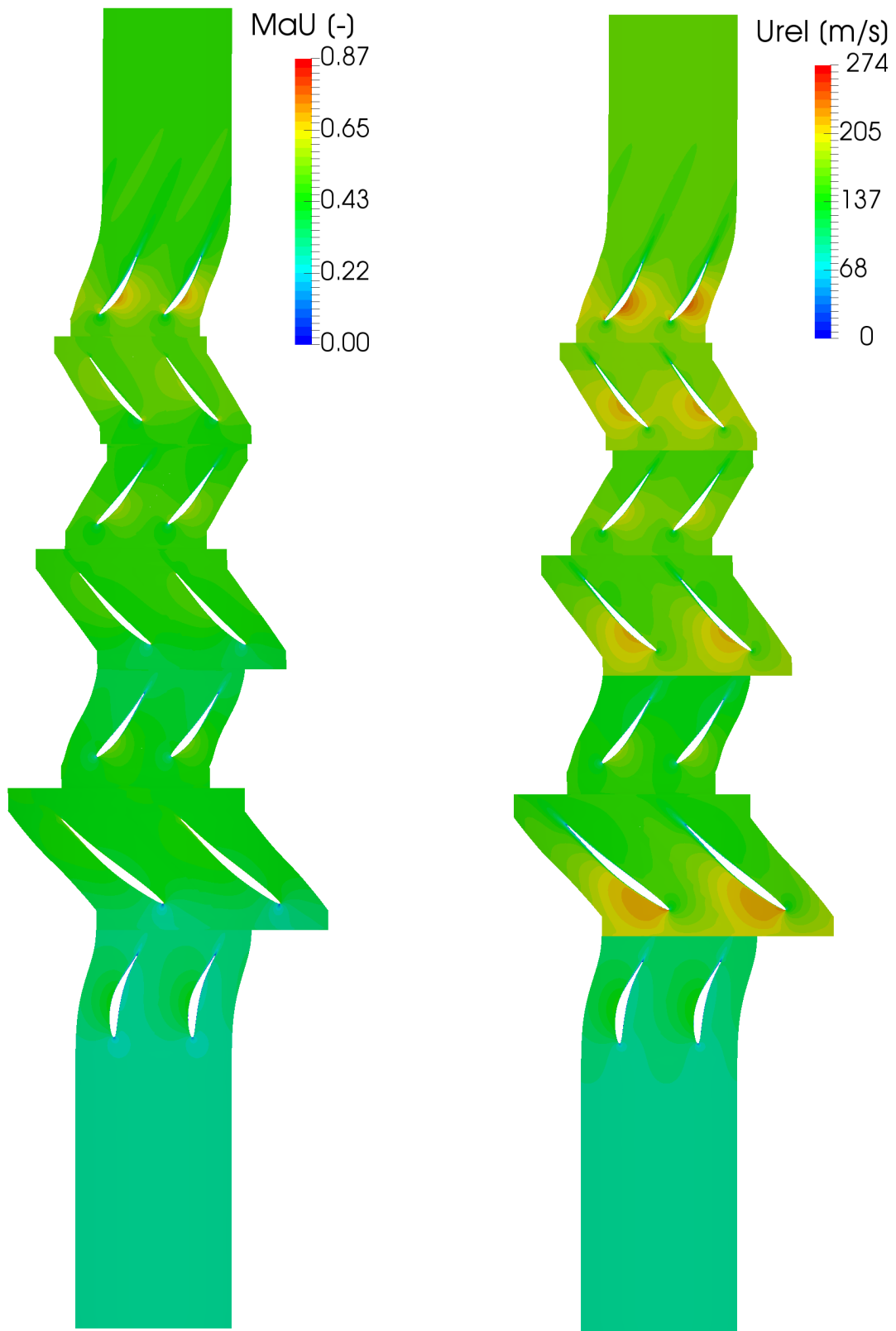(a) STATIC PRESSURE.

(b) STATIC TEMPERATURE.

Figure 42: STATIC PRESSURE AND STATIC TEMPERATURE FIELD FOR THE NEAR-CHOKE OPERATING POINT AT 68% ANGULAR VELOCITY.

(a) Aboslute Mach Number Field.   (b) Relative Velocity Magnitude.

Figure 43: Absolute Mach number and relative velocity magnitude for the near-choke operating point at 68% angular velocity.

Figures 42 and 43 show the flow field calculated by the numerical simulation for the near-choke operating point at 68% angular velocity in terms of static pressure, temperature, Mach number and relative velocity. This operating point operates at the lowest overall total pressure ratio of the examined operating points. The increase of pressure and velocity through the compressor is lower than in other operating points. Figure 38 shows that the last stage of the turbomachine is not heavily loaded and that can be observed in the pressure field (Figure 42a).

4.7 Closure

Results of the numerical simulations of three IDAC operating points are presented in this section. The overall performance of simulated operating points is compared to the overall performance of equivalent experimentally measured operating points in terms of mass flow rate, total pressure ratio, adiabatic efficiency and power input. The numerical results are compared with the available flow field data. Both comparisons show that the numerical simulations are able to provide satisfactory results. The biggest deviation from the experimental result for the overall performance data is 11%. Taking into consideration the applied assumptions and simplifications, the comparison with the experimentally gathered flow field data shows that the numerical simulations were able to capture the nature of the flow inside the compressor.

Along with comparison with experimental data, additional interesting flow features obtained by the numerical simulations are presented. Examining the presented flow features via experiment could prove challenging, but they are easily investigated with numerical simulations.

5   Conclusion and Future Work

This thesis presents numerical simulations of compressible fluid flow in a multi-stage axial compressor performed with `foam-extend`'s `steadyCompresssibleMRFFoam` solver. In order for the numerical simulations to be performed, the compressor geometry had to be spatially discretized. Since the flow inside the axial turbocompressor is considered periodic, only a single passage of the compressor was numerically simulated. When simulating periodic geometries, periodic boundary conditions can be used. In this thesis the `cyclicGgi` boundary condition is used on periodic boundaries. The numerical mesh consists of seven different regions, each defined by a corresponding blade geometry. In order to connect the non conformal mesh regions two different methods were used: `mixingPlane` and `overlapGgi`. Because of the number of blades in each row, the `overlapGgi` method could not be used with the original compressor geometry. The compressor was changed as if every blade row has the same same number of blades.

Numerical results are compared to experimental measurements for three different operating points. The results for the overall compressor performance are satisfactory accurate. The numerical model is able to accurately describe different operating regimes of an axial turbocompressor and capture characteristic flow phenomena at different operating points. The results for the near stall operating point at 68% angular velocity show that the numerical simulation was able to predict the compressor performance better than the design method. This leads to a conclusion that numerical methods can be used in the design process of axial turbocompressors.

Since the numerical simulation showed to accurately capture the flow characteristics additional operating points could be simulated to obtain performance curves for different angular velocities. A transient simulation could be performed and be compared to the available experimental data.

References

[1] Weller, H. G., Tabor, G., Jasak, H., and Fureby, C., "A tensorial approach to computational continuum mechanics using object-oriented techniques," Computers in physics, Vol. 12, No. 6, 1998, pp. 620–631.

[2] Jasak, H. and Beaudoin, M., "Openfoam turbo tools: From general purpose cfd to turbomachinery simulations," ASME-JSME-KSME 2011 Joint Fluids Engineering Conference, American Society of Mechanical Engineers, 2011, pp. 1801–1812.

[3] Beaudoin, M. and Jasak, H., "Development of a Generalized Grid Interface for Turbomachinery simulations with OpenFOAM," Proceedings of International conference "Open Source CFD International Conference", 2008.

[4] Beaudoin, M., Nilsson, H., Page, M., Magnan, R., and Jasak, H., "Evaluation of an improved mixing plane interface for OpenFOAM," IOP Conference Series: Earth and Environmental Science, Vol. 22, No. 2, 2014, pp. 022004.

[5] Niehuis, R., Bohne, A., and Hoynacki, A., "Experimental investigation of unsteady flow phenomena in a three-stage axial compressor," Proceedings of the Institution of Mechanical Engineers, Part A: Journal of Power and Energy, Vol. 217, No. 4, 2003, pp. 341–348.

[6] Hoynacki, A., Gallus, H. E., and Niehuis, R., "Experimentelle Untersuchung der instationären Strömungsvorgänge in einem dreistufigen Axialverdichter mit CDA-Beschaufelung," MTZ - Motortechnische Zeitschrift, Vol. 61, No. 7, 2000, pp. 508–514.

[7] Dixon, S. L. and Hall, C. A., Fluid Dynamics and Thermodynamics of Turmomachinery (Seventh Edition), Butterworth-Heinemann, 2014.

[8] Niehuis, R., "Aufstellung von empirischen Modellen zur Beschreibung der periodischen Interaktion benachbarter Schaufelreihen sowie des Einflusses radialer Mischunsvorgänge auf die Strömung in hochdrehenden mehrstufigen Axialverdictern," Tech. rep., RWTH Aachen, 2003.

[9] Spurk, J. H. and Aksel, N., Fluid Mechanics (Second Edition), Springer, 2008.

[10] Allen, M. P., "Introduction to Molecular Dynamics Simulation," John von Neumann Institute for Computing, 2004.

[11] Landau, L. and Lifshitz, E., Fluid Mechanics, No. v. 6, Elsevier Science, 1987.

[12] Ingram, G., Basic Concepts in Turbomachinery, Grant Ingram and Ventus Publishing ApS, 2009.

[13] "Parsons designs first axial flow compressor," `https://www.turbomachinerymag.com/parsons-designs-first-axial-flow-compressor-2/`, 2015., last access 19.4.2017.

[14] Decaix, J., Balarac, G., Dreyer, M., Farhat, M., and Münch, C., "RANS and LES computations of the tip-leakage vortex for different gap widths," Journal of Turbulence, Vol. 16, No. 4, 2015, pp. 309–341.

[15] Reis, A. J. F., Validation Of NASA Rotor 67 with OpenFOAM's Transonic Density-Based Solver, Master's thesis, Universidade Nova de Lisboa, 2013.

[16] Jasak, H., "Numeričke metode u mehanici kontinuuma (Numerical Methods in Continuum Mechanics), Material for lectures," 2006.

[17] Šojat, B., Development of an Automated Process for Turbine Blade Optimisation, Master's thesis, University of Zagreb, 2017.

[18] Jasak, H., "Numerical Solution Algorithms for Compressible Flows," Lecture Notes, 2007.

[19] De Dominicis, I., Cvijetić, G., Willetts, M., Jasak, H., "Enhanced Turbomachinery Capabilities for foam-extend: Development and Validation," 2016.

[20] Žužul, J., Numerical Evaluation of the Performance Curve for the NASA Rotor 67, Master's thesis, University of Zagreb, 2017.

[21] George, W. K., "Lessons in Turbulence for the 21st Century," `http://www.turbulence-online.com/Publications/Lecture_Notes/Turbulence_Lille/TB_16January2013.pdf`, 2013.

[22] Ristorcelli, J. and Morrison, J., "The Favre–Reynolds average distinction and a consistent gradient transport expression for the dissipation," Physics of Fluids, Vol. 8, No. 10, 1996, pp. 2783–2785.

[23] Amstutz, O., Aakti, B., Casartelli, E., Mangani, L., and Hanimann, L., "Predicting the performance of a high head Francis turbine using a fully implicit mixing plane," Journal of Physics: Conference Series, Vol. 579, No. 1, 2015, pp. 012009.

[24] Du, P. and Ning, F., "Validation of a novel mixing-plane method for multistage turbomachinery steady flow analysis," Chinese Journal of Aeronautics, Vol. 29, No. 6, 2016, pp. 1563 – 1574.

[25] Dawes, W., "Towards improved throughflow capability: The use of 3D viscous flow solvers in a multistage environment," ASME 1990 International Gas Turbine and

Aeroengine Congress and Exposition, American Society of Mechanical Engineers, 1990, pp. V001T01A008–V001T01A008.

[26] Mangani, L., Casartelli, E., Hanimann, L., Wild, M., and Spyrou, N., "Assessment of an implicit mixing plane approach for pump-turbine applications," IOP Conference Series: Earth and Environmental Science, Vol. 22, No. 2, 2014, pp. 022003.

[27] Niehuis, R., "EXPERIMENTAL OFF-DESIGN INVESTIGATION OF UNSTEADY SECONDARY FLOW PHENOMENA IN A THREE-STAGE AXIAL COMPRESSOR AT 100% NOMINAL SPEED," Unsteady Aerodynamics, Aeroacoustics and Aeroelasticity of Turbomachines, 2006, pp. 369.

[28] Hobbs, D. and Weingold, H., "Development of controlled diffusion airfoils for multistage compressor application," ASME 1983 International Gas Turbine Conference and Exhibit, American Society of Mechanical Engineers, 1983, pp. V001T01A058–V001T01A058.

[29] Salunke, N. P. and Channiwala, S., "Design and Analysis of a Controlled Diffusion Aerofoil Section for an Axial Compressor Stator and Effect of Incidence Angle and Mach No. on Performance of CDA," International Journal of Fluid Machinery and Systems, Vol. 3, No. 1, 2010, pp. 20–28.

[30] Bohne, A. and Niehuis, R., "Experimental Off-Design Investigation of Unsteady Secondary Flow Phenomena in a Three-Stage Axial Compressor at 68% Nominal Speed," ASME Turbo Expo 2004: Power for Land, Sea, and Air, American Society of Mechanical Engineers, 2004, pp. 857–866.